



UNIVERSIDADE DE SÃO PAULO
ESCOLA POLITÉCNICA

LUCAS ALVES DA SILVA

**Characterization and evaluation of Fe catalysts supported on zeolite H-ZSM5 for the
Fischer-Tropsch synthesis**

São Paulo

2023

LUCAS ALVES DA SILVA

**Characterization and evaluation of Fe catalysts supported on zeolite H-ZSM5 for the
Fischer-Tropsch synthesis**

Revised version

Dissertation presented to the Chemical Engineering Department of Escola Politécnica da Universidade de São Paulo as a required step to obtain the degree of Master in Science.

Concentration area: Chemical Engineering
Advisor: Prof. Dr. Reinaldo Giudici
Co-advisor: Prof. Dr. Ing. Martin Schmal
Co-advisor: Prof. Dra. Rita M. de Brito Alves

São Paulo


2023

Autorizo a reprodução e divulgação total ou parcial deste trabalho, por qualquer meio convencional ou eletrônico, para fins de estudo e pesquisa, desde que citada a fonte.

Este exemplar foi revisado e corrigido em relação à versão original, sob responsabilidade única do autor e com a anuência de seu orientador.

São Paulo, 19 de Janeiro de 2024

Assinatura do autor: 

Assinatura do orientador: 

Catálogo-na-publicação

Silva, Lucas

Characterization and evaluation of Fe catalysts supported on zeolite H ZSM5 for the Fischer-Tropsch synthesis / L. Silva -- versão corr. -- São Paulo, 2023.

135 p.

Dissertação (Mestrado) - Escola Politécnica da Universidade de São Paulo. Departamento de Engenharia Química.

1.catálise 2.cinética 3.zeólitas 4.combustível sintético 5.Fischer-Tropsch
I.Universidade de São Paulo. Escola Politécnica. Departamento de Engenharia Química II.t.

ASSESSMENT

SILVA, L. A. **Characterization and evaluation of Fe catalysts supported on zeolite H-ZSM5 for the Fischer-Tropsch synthesis.** 2023. Dissertation (Master in Science – Chemical Engineering) – Escola Politécnica, Universidade de São Paulo, São Paulo 2023.

Approved at: 11/12/2023

Judging Committee

Prof. Dr.	Reinaldo Giudici
Institution:	Escola Politécnica da Universidade de São Paulo
Judgment:	Approved
Prof. Dr.	Robson Pablo Sobradieł Peguin
Institution:	Braskem S.A.
Judgment:	Approved
Prof. Dr.	Pedro Henrique Cury Camargo
Institution:	University of Helsinki
Judgment:	Approved

To my parents, Noemia Alves and Antônio Alves for all their love and support.

AKCNOLEDGEMENTS

I want to express my sincere gratitude to my advisors Professor Martin Schmal, Professor Rita Alves, and Professor Reinaldo Giudici for their guidance, trust, teachings, and support throughout this work.

I would like to thank my best lab mate, Heloisa Ruschel, for her companionship, support, conversations and for being a positive force during this journey.

I thank all the friends and collaborators of our research groups, LSCP, and LaPCat, including professors, post-docs, master, and doctoral students for the discussions, teachings, and their assistance. Special thanks to Egydio Terziotti, Heloisa Ruschel, Magno Santos, Valdeir Abreu, Higor Garona, and Victor Albertini, for their friendship and for creating an enjoyable and cheerful academic environment.

I extend my gratitude to my longtime friends, especially Nicolas Santos, Jean Borges, and Lary Matos for being so supportive.

I am sincerely grateful for my family, parents, siblings, and nephews for their love and for being a source of encouragement during my professional journey.

I also thank Professor Pedro Camargo and his research group, especially to Vilma Heczko and Letícia Bezerra, at the University of Helsinki for their collaboration throughout this project and for welcoming me during my exchange period in Finland.

I would also like to thank Professor Elisabeth Assaf and her research group at the Institute of Chemistry, USP-São Carlos, for the technical support.

Finally, I thank the São Paulo Research Foundation (FAPESP) and the Coordination for the Improvement of Higher Education Personnel (CAPES) for the financial support in this project.

This work was funded by FAPESP under processes no. 2021/05329-7 and no. 2022/07813-6.

*“Success is to be measured not so much by the position
that one has reached in life as by the obstacles which he
has overcome while trying to succeed.”*

Booker T. Washington

ABSTRACT

The increasing of energy demand and the concerns about the climate change make the development of synthetic fuels of utmost importance. The Fischer-Tropsch synthesis (FTS), a step in the gas-to-liquid processes, is a catalytic reaction that converts synthesis gas (CO and H₂) into a wide range of hydrocarbons and is as a promising technology to produce synthetic fuels. This process occurs by a polymerization mechanism and its results are dependent on the operating conditions, and mainly on the catalyst used. Iron (Fe)/zeolite catalysts have been extensively studied for FTS due to their cost-effectiveness and bifunctional activity. However, little research has been reported addressing a complete understanding of physical-chemical properties of Fe/H-ZSM5 and the effects of varied reaction condition on FTS, as well as the kinetic assessment of CO conversion over this type of catalyst. This work focused on studying the synthesis, characterization, catalytic and kinetic assessments of Fe/H-ZSM5 for Fischer-Tropsch synthesis. The characterization results showed zeolite and iron oxide structures with crystallinity, high surface area of the support, and presence of mesopores. Fe particles were heterogeneously distributed on the support in different sizes, presenting multiple reduction stages. The catalysts were active for the Fischer-Tropsch synthesis, showing a maximum CO conversion of 86% at 350°C and an average conversion greater than 50% at 300°C. In general, the catalysts exhibited greater formation of short-chain, C₂-C₄, and medium chain, C₅-C₈, hydrocarbons. Temperature, pressure, space velocity and feed composition showed a considerable influence on CO conversion. The catalyst exhibited a stable activity over time without structural changes or coke deposition. Finally, the proposed kinetic model for the best performing catalyst followed the carbide route, considering a double site mechanism with dissociative adsorption of CO and H₂, and participation of CO₂, which was further confirmed by *in situ* characterization.

Keywords: Fischer-Tropsch synthesis, Zeolites, Iron, synthetic fuels, catalysis, kinetics.

RESUMO

O aumento da demanda energética e as preocupações com as mudanças climáticas destacam a importância do desenvolvimento de combustíveis sintéticos. A síntese de Fischer-Tropsch (FTS), uma etapa nos processos gas-to-liquid, é uma reação catalítica que converte gás de síntese (CO e H_2) em uma ampla variedade de hidrocarbonetos, e é uma tecnologia promissora para a produção de combustíveis sintéticos. Esse processo ocorre por meio de um mecanismo de polimerização e seus resultados dependem das condições operacionais e principalmente do catalisador utilizado. Catalisadores de Fe/zeólita têm sido amplamente estudados para FTS devido ao seu custo-benefício e atividade bifuncional. No entanto, há pouca pesquisa abordando uma compreensão completa das propriedades físico-químicas de Fe/H-ZSM5 e os efeitos das variadas condições de reação na FTS, assim como a avaliação cinética da conversão de CO sobre esse tipo de catalisador. Este trabalho concentrou-se no estudo da síntese, caracterização e avaliações catalíticas e cinéticas de Fe/H-ZSM5 para a síntese de Fischer-Tropsch. Os resultados de caracterização mostraram estruturas de zeólita e óxido de ferro com cristalinidade, alta área superficial do suporte e presença de mesoporos. As partículas de Fe foram distribuídas heterogeneamente no suporte em diferentes tamanhos, apresentando múltiplos estágios de redução. Os catalisadores foram ativos para a síntese de Fischer-Tropsch, alcançando uma conversão máxima de CO de 86% a 350°C e uma conversão média acima de 50% a 300°C. Em geral, os catalisadores apresentaram uma maior formação de hidrocarbonetos de cadeia curta ($\text{C}_2\text{-C}_4$) e de cadeia média ($\text{C}_5\text{-C}_8$). Temperatura, pressão, velocidade espacial e composição da alimentação mostraram uma considerável influência na conversão de CO. O catalisador manteve sua atividade estável ao longo do tempo sem mudanças estruturais ou deposição de coque. Por fim, o modelo cinético proposto para o catalisador de melhor desempenho seguiu a rota do carbetto, considerando um mecanismo de sítio duplo com adsorção dissociativa de CO e H_2 , e participação de CO_2 , confirmada pela caracterização *in situ*.

Palavras-chave: Síntese de Fischer-Tropsch, Zeólitas, Ferro, combustíveis sintéticos, catálise, cinética

ILLUSTRATION INDEX

Figure 1 - Bibliometric analysis for "Fischer-Tropsch" from Scopus database:	22
Figure 2 - Gas-to-liquid processes.....	24
Figure 3 - FTS mechanisms. a) carbide b) enol and c) CO insertion.	28
Figure 4 - Possible mechanistic routes for FTS.....	30
Figure 5 - Variation of H ₂ chemisorption with CO chemisorption on group VIII B metals.	31
Figure 6 - Product selectivity in FTS according to ASF model.	32
Figure 7 - Schematics of FTS reactors. a) fixed-bed, b) slurry-bed, c) fluidized bed.	36
Figure 8 - Behavior of transition metals in FTS.....	37
Figure 9 - Fe particles in FTS a) phase transformations. b) iron carbide phases.....	40
Figure 10 - Structures of zeolites Y and ZSM-5	43
Figure 11 - Bifunctional catalysts for Fischer-Tropsch synthesis	44
Figure 12 - Microactivity Effi automated reaction system for gas-to-liquid processes.....	53
Figure 13 - TGA curves of the Fe-Z91PM and Fe-Z91DI as-synthesized catalysts	57
Figure 14 - TGA curves of the Fe-Z91PM and Fe-Z91DI calcined catalysts.	58
Figure 15 - FT-IR Spectra of the Fe-Z91PM, Fe-Z(52, 91, 371)DI catalysts.	59
Figure 16 - FT-IR Spectra of the Fe-Z91PM and Fe-Z(52, 91, 371)DI catalysts	59
Figure 17 - HZSM-5 network structure.....	60
Figure 18 - RAMAN Spectra of the Fe-Z91PM and Fe-Z(52, 91, 371) DI catalysts	61
Figure 19 - Crystal structure of hematite.....	62
Figure 20 - XRD diffractogram of the Fe-Z91PM and Fe-Z(52, 91, 371) DI catalysts.....	63
Figure 21 - N ₂ adsorption/desorption isotherms of Fe-Z91DI and Fe-Z91PM catalysts calcined and HZSM-5.....	64
Figure 22 - H ₂ -TPR curves of the Fe-Z91PM and Fe-Z(52, 91, 371)DI catalysts	66
Figure 23 - H ₂ -TPR detailed profile of the Fe-Z91DI catalyst.....	67
Figure 24 - TEM image of Fe-Z91DI catalyst with a resolution of 500 nm.....	68
Figure 25 - TEM image of Fe-Z91DI catalyst with a resolution of 50 nm	69
Figure 26 - TEM image of Fe-Z91PM catalyst with a resolution of 500 nm.....	69
Figure 27 - TEM image of Fe-Z91PM catalyst with a resolution of 100 nm.....	69
Figure 28 - EDS analysis of the Fe-Z91DI catalyst.	70
Figure 29 - CO ₂ -TPD profiles of pure HZSM-5 and impregnated catalysts.	71
Figure 30 - NH ₃ -TPD profiles of pure HZSM-5 and impregnated catalysts.....	73

Figure 31 - CO - TPD profiles of impregnated catalysts.....	74
Figure 32 - Fischer-Tropsch activity evaluation with temperature screening	75
Figure 33 - CO ₂ selectivity during Fischer-Tropsch reaction with temperature screening.	76
Figure 34 - Effect of SiO ₂ /Al ₂ O ₃ ratio on FTS activity and product distribution.	78
Figure 35 - Effect of SiO ₂ /Al ₂ O ₃ ratio on FTS activity during time on stream (TOS).	78
Figure 36 - Effect of temperature on FTS activity and product distribution.	79
Figure 37 - ASF fitted model for FTS tests under different temperatures.	81
Figure 38 - Effect of WHSV on FTS activity and product distribution.	82
Figure 39 - Effect of pressure on FTS activity and product distribution.....	83
Figure 40 - Effect of H ₂ /CO ratio on FTS activity and product distribution.	84
Figure 41 - ASF fitted model for FTS tests under different H ₂ /CO ratios.....	85
Figure 42 – FTS time on stream test. Fe-Z91DI catalyst.	85
Figure 43 – Post-reaction FTIR spectroscopy analysis with the Fe-Z91DI catalyst.	87
Figure 44 – Post-reaction RAMAN spectroscopy analysis with the Fe-Z91DI catalyst.....	88
Figure 45 – Pre- and Post-reaction XRD analyses with the Fe-Z91DI catalyst.....	89
Figure 46 - Post-reaction TEM images of the Fe-Z91DI catalyst.	90
Figure 47 - W/F _{syg} vs X _{CO} for the Fe-Z91DI.....	91
Figure 48 - Parity plot of predicted Model 1 and experimental CO consumption rate.	100
Figure 49 - Residuals distribution: a) dependent r _{co} ' variable b) normal probability plot.....	100
Figure 50 - Surface response of Model 1 evaluating temperature and H ₂ /CO ratio.....	101
Figure 51 – Model 1 and experimental data curves.	102
Figure 52 – DRIFTS-in situ H ₂ /CO analysis of Fe-Z91DI catalyst.	103

TABLE INDEX

Table 1- Current commercial Fischer-Tropsch plants worldwide.....	26
Table 2 - Comparison of some characteristics of Co and Fe-based catalysts for FTS	39
Table 3 - Summary of literature FTS results with Fe/Zeolite catalysts.....	46
Table 4 - XRD parameters and crystallite size of catalysts.....	64
Table 5 - Textural properties of the catalysts.	65
Table 6 - NH ₃ and CO ₂ adsorption results from TPD analysis.	72
Table 7 - Parameters of Weiz-Prater and Mears criteria calculation.....	92
Table 8 - Experimental conditions and results for kinetic tests with the Fe-Z91DI catalyst. ..	93
Table 9 - Results of fitted kinetic models for CO conversion on Fe-Z91DI catalyst.....	95
Table 10 - Summary of observed bands from DRIFTS analysis.....	104

ABBREVIATION AND ACRONYMS INDEX

ASF	Anderson-Schulz Flory
ATR	Attenuated Total Reflectance
ATR	Autothermal reforming
BET	Brunauer-Emmett-Teller
BRM	Bi-reforming of methane
CCU	Carbon capture and utilization
CNFs	Carbon nanofibers
CNTs	Carbon nanotubes
CSs	Carbon spheres
DI	Dry impregnation
DME	Dimethyl ether
DRIFTS	Diffuse Reflectance Infrared Fourier Transform Spectroscopy
DRM	Dry reforming of methane
EDS	Energy dispersive spectroscopy
Fcc	Face-centered cubic
FID	Flame ionization detector
FT	Fischer-Tropsch
FTIR	Fourier Transform Infrared Spectroscopy
FTS	Fischer-Tropsch Synthesis
FWHM	Full Width at Half Maximum
GC	Gas chromatography
GTL	Gas-to-liquid
HCP	Hexagonal close-packed

HTFT	High-Temperature Fischer-Tropsch
ICSD	Inorganic Crystal Structure Database
IUPAC	International Union of Pure and Applied Chemistry
LHHW	Langmuir-Hinshelwood-Hougen-Watson
LTFT	Low-Temperature Fischer-Tropsch
LUMO	Least unoccupied molecular orbital
MCM	Mobil Catalytic Material
MOF	Metallic organic framework
NPs	Nanoparticles
PM	Physical mixture
POM	Partial oxidation of methane
RDS	Rate-determining step
RMSE	Root mean square error
RWGS	Reverse water-gas-shift
SBA	Santa Barbara Amorphous
SRM	Steam reforming of methane
Syngas	Synthesis gas
TCD	Thermal conductivity detector
TEM	Transmission electron microscopy
TOS	Time on stream
TPD	Temperature programmed desorption
TPR	Temperature programmed reduction
TRM	Tri-reforming of methane
Vol	Volume

WGS	Water-gas-shift
WHSV	Weight hourly space velocity
XPS	X-ray photoelectron spectroscopy
XRD	X-ray diffraction
ZSM-5	Zeolite Socony Mobil-5

SYMBOLS INDEX

Alphanumeric symbols

C_{CO}	carbon monoxide concentration on the catalyst surface.
C_{WP}	Weiz-Prater criteria
D	crystallite mean size
D_{AB}	diffusivity
D_{eff}	effective diffusivity
d_{pore}	pore diameter
E_a	reaction activation energy
F	Fisher Snedecor test value
F_{CO}	carbon monoxide molar inlet flow
F_{syg}	syngas flow
H_{ads}	adsorption heat
k_0	reaction pre-exponential factor
K_{10}, K_{20}	adsorption pre-exponential factor
k_c	mass transfer coefficient
K_i	equilibrium kinetic constant
k_i	reaction kinetic constant
MR	Mears criteria
n	carbon number
P	pressure
p	partial pressure
p_{CO}	carbon monoxide partial pressure

p_{CO_2}	carbon dioxide partial pressure
p_{H_2}	hydrogen partial pressure
p_{H_2O}	water partial pressure
R	gases constant
r	particle radius
R^2	coefficient of determination
r_{CO}	carbon monoxide reaction rate
r_p	molar rate of chain propagation
r_t	molar rate of chain termination
S	vacant sites
S_{BET}	BET surface area
S_{CO_2}	carbon dioxide selectivity
S_{Micro}	microporous area
S_{tot}	total sites amount
T	temperature
V_{Micro}	microporous volume
W	catalyst mass
w_n	mass fraction
X_{CO}	carbon monoxide conversion

Greek symbols

α	chain growth probability factor
β	kinetic coefficient
δ	kinetic coefficient
ε	kinetic coefficient
γ	kinetic coefficient
B	line broadening at half of the maximum intensity
θ	Bragg angle
η	effectiveness factor
κ	dimensionless shape factor
λ	wavelength
μ	kinetic coefficient
π	covalent bond type
ρ_c	catalyst specific mass
σ	covalent bond type
φ	bed porosity
Φ	Thiele's modulus

SUMMARY

1	INTRODUCTION	21
2	LITERATURE REVIEW	23
2.1	GTL PROCESSES.....	23
2.2	HISTORICAL CONTEXT OF FISCHER-TROPSCH SYNTHESIS.....	25
2.3	THE CHEMISTRY OF FISCHER-TROPSCH SYNTHESIS	26
2.3.1	Reaction mechanisms	27
2.3.2	Reaction kinetics	29
2.4	PRODUCT DISTRIBUTION AND SELECTIVITY.....	31
2.5	OPERATING CONDITIONS IN FTS	33
2.5.1	Effect of temperature	33
2.5.2	Effect of pressure	34
2.5.3	Effect of syngas composition and space velocity	34
2.6	REACTORS FOR FTS	35
2.7	CATALYSTS FOR FTS.....	37
2.7.1	Co-based catalysts	38
2.7.2	Fe-based catalysts	39
2.7.3	Effect of promoters	41
2.7.4	Effect of catalyst supports	41
2.8	ZEOLITES AS CATALYST SUPPORT FOR FTS.....	43
3	OBJECTIVES.....	48
4	MATERIALS AND METHODS	49
4.1	CATALYST PREPARATION	49
4.1.1	Materials	49
4.1.2	Catalyst preparation	49
4.2	CATALYST CHARACTERIZATION	50
4.2.1	Thermogravimetric Analysis (TGA)	50
4.2.2	Fourier Transform Infrared Spectroscopy (FTIR)	51

4.2.3	Raman Spectroscopy	51
4.2.4	X-Ray Diffraction (XRD)	51
4.2.5	Hydrogen Temperature Programmed Reduction (TPR)	51
4.2.6	Nitrogen sorption isotherms	52
4.2.7	Transmission Electron Microscopy (TEM)	52
4.2.8	CO, CO₂, and NH₃ Temperature Programmed desorption (TPD)	52
4.2.9	Diffuse Reflectance Infrared Fourier Transform Spectroscopy (DRIFTS-<i>in situ</i>)	52
4.3	FISCHER-TROPSCH PERFORMANCE ASSESSMENT	53
4.3.1	Catalytic Unit	53
4.3.2	Methods for FTS catalyst testing	54
4.4	FISCHER-TROPSCH KINETIC ASSESSMENT	55
4.4.1	Mass transfer effects evaluation	55
4.4.2	Kinetic data acquisition and parameters estimation	56
5	RESULTS AND DISCUSSION	57
5.1	CATALYSTS CHARACTERIZATION	57
5.1.1	Thermogravimetric analysis (TGA)	57
5.1.2	Fourier Transform Infrared Spectroscopy (FTIR)	58
5.1.3	Raman Spectroscopy	60
5.1.4	X-ray diffraction (XRD)	62
5.1.5	N₂ adsorption isotherms	64
5.1.6	Temperature programmed reduction (TPR)	66
5.1.7	Transmission Electron Microscopy (TEM)	68
5.1.8	Temperature programmed desorption (TPD)	70
5.2	FISCHER-TROPSCH PERFORMANCE ASSESSMENT	75
5.2.1	Evaluation of catalytic activity with temperature screening	75
5.2.2	The effect of zeolite SiO₂/Al₂O₃ ratio on catalytic activity and product selectivity	77

5.2.3	The effect of temperature on conversion and product selectivity	79
5.2.4	The effect of space velocity on catalytic activity and product selectivity ...	81
5.2.5	The effect of pressure on catalytic activity and product selectivity	82
5.2.6	The effect of feed composition on catalytic activity and product selectivity 84	
5.2.7	Stability test	85
5.3	POST-REACTION CATALYST CHARACTERIZATION	87
5.3.1	Infrared and RAMAN spectroscopies	87
5.3.2	X-ray diffraction (XRD)	88
5.3.3	Transmission Electron Microscopy (TEM)	90
5.4	FISCHER-TROPSCH KINETIC ASSESSMENT	91
5.4.1	Kinetic regime determination	91
5.4.2	Kinetics data acquisition	92
5.4.3	Diffuse Reflectance Infrared Fourier Transform Spectroscopy (DRIFTS-<i>in situ</i>) 102	
6	CONCLUSIONS	105
6.1	SUGGESTIONS FOR FUTURE WORKS	106
	REFERENCES	107
	APPENDIX A – CONVERSION AND SELECTIVITY CALCULATIONS	126
	APPENDIX B – COMPLEMENTARY FTS TESTS FOR KINETIC MODELING	127
	APPENDIX C – COMPLEMENTARY CATALYST CHARACTERIZATION	129
	APPENDIX D – COMPLEMENTARY FTS TESTS	135

1 INTRODUCTION

The growing energy demand and the depletion of crude oil stimulate the interest in the search for alternative energy sources, especially to supply the needs of the transport sector¹. According to the bp Statistical Review of World Energy (2022)², the global oil production increased by 1.4 million barrels per day (Mbpd) in 2021, while the oil consumption increased by 5.3Mbpd, with most of the consumption growth coming from gasoline (1.8 Mbpd) and diesel (1.3 Mbpd). Moreover, transport is the sector with the highest fossil fuel dependence and was responsible for 37% of the carbon dioxide (CO₂) emissions in 2021³, which draws attention in a world scenario that proposes to reduce greenhouse gas emissions to contain climate change.

Carbon capture and utilization (CCU) technologies, such as CO₂ conversion to hydrocarbons and other value-added chemicals, offer promising solutions to address the issues of fossil fuel consumption and greenhouse gas emissions⁴. In the context of the transport sector, gas-to-liquid (GTL) processes represent a possible technology to produce synthetic fuels, such as alcohol, gasoline, diesel, and kerosene. Among the GTL processes, the Fischer-Tropsch synthesis (FTS) is a well-known route for the production of synthetic hydrocarbon fuel and value-added chemicals.⁵

The Fischer-Tropsch synthesis is a catalytic reaction that converts synthesis gas (syngas), a mixture of CO and H₂, into a wide range of hydrocarbons. Industrially, FTS can be integrated into processes where CO may come from CO₂, such as Methane dry reforming or reverse water-gas-shift (RWGS), leading to promising CO₂-to-chemicals routes.⁶ Moreover, some tandem CO₂ hydrogenation routes via FTS mechanism are also known.⁷ Despite its potential for producing synthetic fuels, FTS faces challenges with CO conversion and product selectivity, limiting its commercial application thereby requiring more development research.

A bibliometric analysis from the Scopus database⁸ for the term “Fischer-Tropsch” between 1939-2022 revealed the publication of 10182 documents, including articles, conference papers, reviews, and book chapters, and 34273 patents. Figure 1 presents a word cloud map with the most common keywords associated with Fischer-Tropsch and a historical analysis of publications with the ranking of countries by published documents.

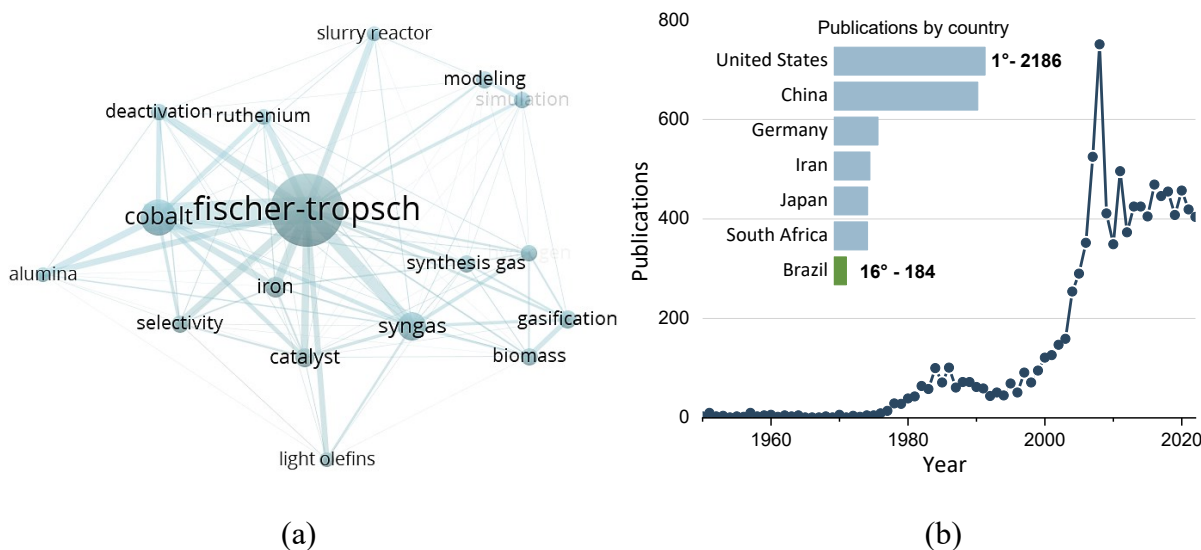


Figure 1 - Bibliometric analysis for "Fischer-Tropsch" from Scopus database: (a) cloud map with the most common keywords associated with Fischer-Tropsch; (b) publications over the years with the ranking of countries by publication.

The most frequently addressed topics in Fischer-Tropsch research are related to catalyst development for this process. Moreover, the analysis showed an increasing number of publications over the years, with a significant increase in the early 2000s. In the world research scenario, the United States, China, and Germany are first placed, while Brazil is on 16th position with 184 publications in this field.

This work aims to study the synthesis, characterization, catalytic testing, and kinetic assessment of Fe catalysts supported on H-ZSM5 zeolite for fuel production via Fischer-Tropsch synthesis. Metal/zeolite are promising Fischer-Tropsch catalysts as both the metal and supports provide activity for this reaction. It should be mentioned that the present master's research is part of the general context of the 4AirCRAFT project⁹, which is a partnership among seven research institutions and universities from several countries: Spain, Germany, Belgium, Italy, Finland, Japan, and Brazil.

The present work is divided into six chapters. Chapter 1 provides a brief introduction with the overall context on the subject. Chapter 2 presents a literature review of the Fischer-Tropsch Synthesis, including the reactions involved, effects of operational conditions, and different catalysts. Chapter 3 outlines the objectives of the work. In Chapter 4, the materials and methods used for the synthesis and characterization of catalysts, catalytic tests, and kinetic studies are detailed. Chapter 5 presents the results of characterization, catalytic tests, and kinetic modeling with a discussion of these findings based on the literature. Finally, Chapter 6 summarizes the main conclusions of the work and provides suggestions for future research.

2

LITERATURE REVIEW

This section presents a review of fundamental concepts related to the Fischer-Tropsch synthesis, including chemical reaction mechanisms, the effect of reaction conditions, and the kinetic behavior of the reaction. Additionally, it offers a literature review concerning the development of catalysts for this process, with relevant findings applicable to the present study.

2.1 GTL PROCESSES

The GTL technology aims to convert gases, such as CH_4 or CO_2 , into liquid products including fuels, aromatics, and alcohols. This conversion can occur through a direct route,¹⁰ involving processes such as aromatization, methanol synthesis, and tandem CO_2 -to-liquids, or through an indirect route, mediated by syngas production via CH_4 reforming or RWGS reaction, followed by processes such as Fischer-Tropsch and Dimethyl ether synthesis.^{11,12} A schematic with the main GTL process is shown in Figure 2.

Among these processes, the study of FTS for fuel production from syngas has been widely investigated in the literature from the perspectives of modeling and simulation¹³, experimental design¹⁴, catalyst development¹⁵, and economic assessment.¹⁶ The syngas is a mixture composed mainly of H_2 and CO , which can be produced using different technologies depending on the carbon feedstock, including natural gas, CO_2 , coal, or biomass.¹⁷ Currently, syngas production is carried out by reforming processes, such as steam reforming of methane (SRM), dry reforming of methane (DRM), and partial oxidation of methane (POM).¹¹

SRM is a highly endothermic process and converts methane and water vapor into syngas with a theoretical H_2/CO molar ratio of 3, making this route mostly used for hydrogen production.^{18,19} DRM is an endothermic process, in which CH_4 reacts with CO_2 to produce syngas with an H_2/CO of 1, suitable for DME synthesis and some FTS processes.²⁰ In POM, the exothermic combustion of CH_4 produces syngas with an ideal H_2/CO of 2 for FTS²¹. However, achieving this ratio is challenging due to the presence of the RWGS side reaction, which consumes H_2 in the process.¹⁰ Thus, steam can be introduced into the POM feed, leading to autothermal reforming (ATR). ATR combines both SMR and POM, where the heat generated

by partial oxidation provides the energy required for the SMR reaction, making ATR an attractive process for syngas generation.²²

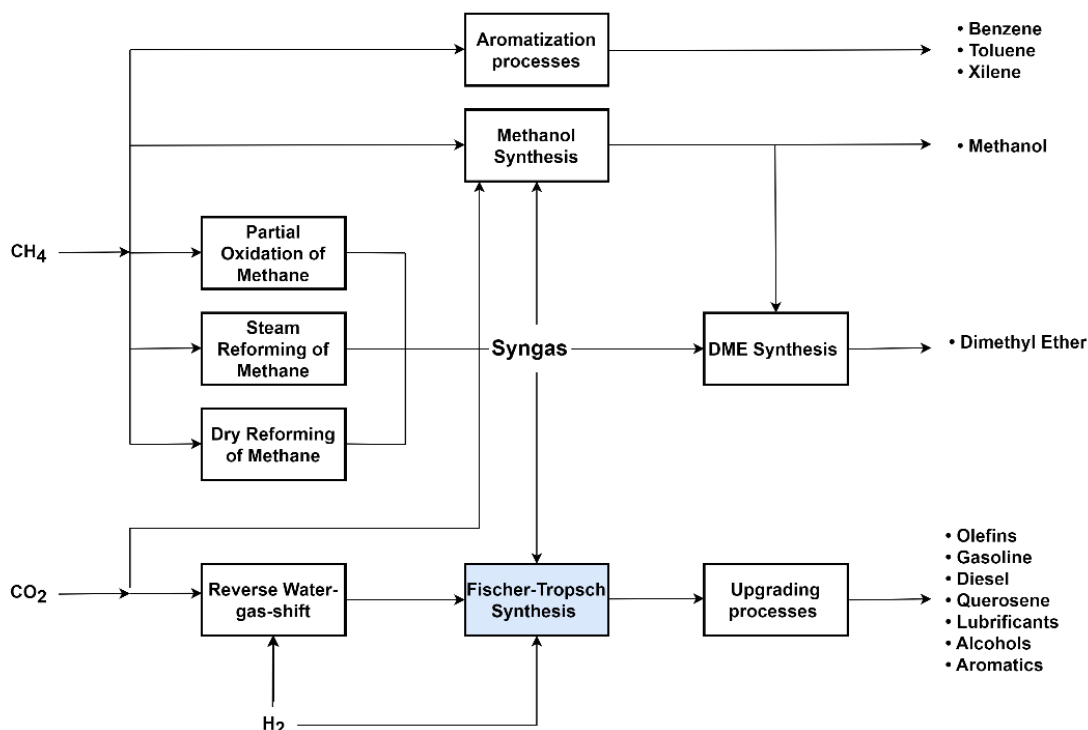


Figure 2 - Gas-to-liquid processes.

Other combined reforming processes for syngas production, such as the bi-reforming of methane (BRM), a combination between SRM and DRM, and tri-reforming of methane (TRM), which combines SRM, DRM, and POM, are also known.²³ These processes are attractive from an environmental perspective, due to the usage of two greenhouse gases.

The Fischer-Tropsch synthesis is a key route for liquid fuel production in the syngas-GTL process. The syngas from reforming steps is catalytically converted in the FTS reactor into a wide range of hydrocarbons via a polymerization reaction.¹⁷ The process is exothermic and usually operated in slurry, fixed, or circulating bed reactors at pressures around 20 bar.²⁴ A detailed description of the entire FTS process will be presented in the subsequent sections of this study.

Considering different FTS outlet products, conventional processes from petroleum refining, such as hydrocracking and isomerization, are incorporated as a third step in gas-to-liquid (GTL) technology for product upgrading.¹⁰ Normally, product upgrading aims at the conversion of hydrocarbons heavier than diesel into the middle distillate range, or at the oligomerization processes of light hydrocarbons. In these processes, acidic materials such as

alumina and zeolites have been extensively studied to promote hydrogenation of alkenes or to protonate unsaturated hydrocarbons to intermediates for cracking and isomerization reactions.²⁵

2.2 HISTORICAL CONTEXT OF FISCHER-TROPSCH SYNTHESIS

In the twentieth century, the use of energy from petroleum was crucial for the development of industrialized nations. The introduction of automobiles, planes and ships combined with the greater energy-efficiency of oil compared to wood or coal replaced the use of solid fuel by liquid fuel.²⁶ Faced with the absence of natural petroleum sources, some European nations such as Germany, Britain, and France became dependent on oil imports. This scenario prompted efforts in the development of synthetic oil from coal, which was an abundant feedstock at the time.²⁶

Followed by the discoveries of CH₄ production by Sabatier²⁷ and coal liquefaction by Friedrich Bergius²⁸, the German scientists Franz Fischer and Hans Tropsch developed a process to convert coal into liquid hydrocarbons in 1926.²⁶ The scientists produced CO and H₂ by hydrocracking coal with steam and then reacted the gases on a cobalt surface catalyst to generate petroleum-like liquids. This achievement generated some patents for Germany^{29,30} and made the country the first industrialized nation to produce synthetic oil from coal.³¹

The call for petroleum independence in the Nazi government accelerated the development of Fischer-Tropsch technology during the 1930s-40 in Germany. Franz Fischer's research resulted in the operation of the first commercial-size FT plant in 1936. From then until 1942, nine FT plants were built contributing to around 12-15 % of Germany's liquid fuel requirement. The production declined in 1944 with the Allied forces bombing during World War II and the high average costs of FTS products compared to the oil-importing ones.²⁶

After the War, the Allied Forces dominated the FT technology, and the first plants were built in the United States in the 1950s. The most expressive development of large-scale FTS occurred in South Africa with Sasol's plant operation.³² Later in the 1970s, the crude oil crisis led to an expansion of Sasol's plants and renewed interest in FTS from companies such as ExxonMobil, Shell, and Statoil. From the 1990s to the 2010s, new GTL plants were built by PetroSA, Shell, and Sasol.³² Table 1 presents the current commercial Fischer-Tropsch plants worldwide.

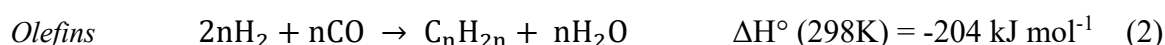
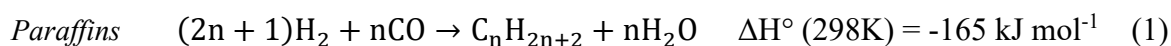
Table 1- Current commercial Fischer-Tropsch plants worldwide

Company	Location	Carbon Feedstock	Capacity (bpd)	Start-up year
Sasol	Sasolburg – South Africa	Coal	5000	1955
Sasol	Secunda – South Africa	Coal	85000	1980
Sasol	Secunda – South Africa	Coal	85000	1982
PetroSA	MosselBay – South Africa	Natural gas	30000	1992
Shell	Bintulu – Malaysia	Natural gas	14700	1993
Shell & Qatar Petrol.	Ras Laffan – Qatar	Natural gas	140000	2011
Sasol & Qatar Petrol.	Ras Laffan – Qatar	Natural gas	34000	2006
Sasol & Chevron	Escravos – Nigeria	Natural gas	34000	2013

Source: ³²⁻³⁴

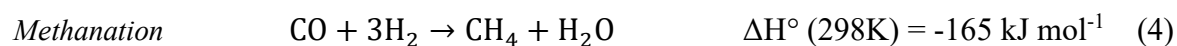
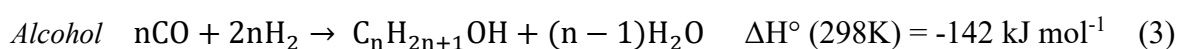
2.3 THE CHEMISTRY OF FISCHER-TROPSCH SYNTHESIS

The Fischer-Tropsch reaction is characterized by the conversion of CO and H₂ into hydrocarbons. However, executing this transformation involves a complex series of parallel reactions, resulting in a broad product spectrum that includes paraffins, olefins, oxygenates, and other by-products. The reactions represented by Eqs. (1) and (2) are the target transformations in the FTS process, as they yield paraffins and olefins, that can be further separated into valuable chemicals. The resulting products, known as syncrude, comprise a mixture of synthetic naphtha, fuel, lubricating oils, and waxes, where straight-chain molecules are predominant.^{32,35}

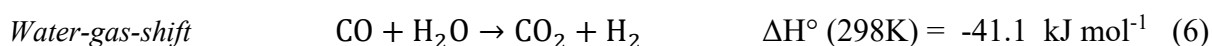


The FT reactions are exothermic, which makes efficient heat removal from the catalytic system necessary. The heat released per reacted carbon atom to build the chains averages about 35 kcal³⁶. Moreover, the reactions are kinetically controlled and far from equilibrium, which, according to Dry (2004)³⁷, makes the product spectra different from what would be expected from thermodynamic considerations.

The process also contains a considerable number of side reactions. Depending on the reaction conditions, the presence of oxygen during chain growth can lead to the formation of alcohols and other oxygenated products, Eq. (3). Among these side reactions, methane formation is noteworthy and is often considered separately in kinetic descriptions, Eq. (4). Methanation is more likely to occur at high temperatures, in environments with abundant hydrogen, and particularly with the use of nickel catalysts. Additionally, the Boudouard reaction, Eq. (5), occurs over most FTS catalysts. This reaction results in the deposition of amorphous carbon, which leads to the deactivation of metallic sites within the catalyst.³⁸



The water-gas-shift (WGS) reaction, Eq. (6), is another side reaction present in FTS, especially when iron catalysts are used. In this case, WGS needs special attention, as the reaction influences the partial pressures of CO, H₂, CO₂, and H₂O, thereby affecting FTS product selectivity, reaction rate, and catalyst deactivation. Besides, the occurrence of WGS is beneficial in some industrial processes, especially when syngas with a low H₂/CO is used, as the reaction provides a supplementary source of H₂ to the system.³⁹



2.3.1 Reaction mechanisms

From a chemical point of view, Fischer-Tropsch synthesis is considered both a CO hydrogenation and a polymerization reaction.³² Despite the discovery of the reaction has been made in the 1930s, many details regarding its mechanism remain in debate.²⁴ Two main paths have been proposed to describe FTS mechanisms. In the first hypothesis, the C-O or C-OH bond is cleaved to form 'CH_x' species, which are incorporated into the growing chain. In the second hypothesis, CO is directly inserted into the growing chain and an intermediate RCH_xOH is formed⁴⁰. The representative mechanistic routes of these hypotheses are called carbide, enol, and CO insertion, differing in the adsorption type and monomer structure.^{35,41}

The carbide mechanism was initially proposed by Franz Fischer and Hans Tropsch in 1926. This route, presented in Figure 3a, considers that CO adsorbs dissociatively on the

catalyst surface and then, the C species are hydrogenated to form methylene monomer, which is the key intermediate. The chain growth occurs with the insertion of adsorbed CH_x species onto the metal-carbon bond of adsorbed C_nH_m molecules. The termination step can occur by two different mechanisms: the addition of H or CH_3 species to the chain leading to paraffins, or direct desorption of unsaturated chains leading to olefins.^{35,42}

Although the carbide mechanism is widely accepted to describe liquid hydrocarbon formation, it fails to explain the formation of branched hydrocarbons and oxygenated products, such as alcohols and acids. Thus, several modified carbide mechanisms were proposed to cover this limitation. According to Teimouri, Abatzoglou, and Dalai (2021)³⁵, the variations point to different chain initiators, such as methyl⁴³ and vinyl groups⁴⁴, different chain-growth monomers⁴⁵, or alternative CO dissociation paths.^{46–48}

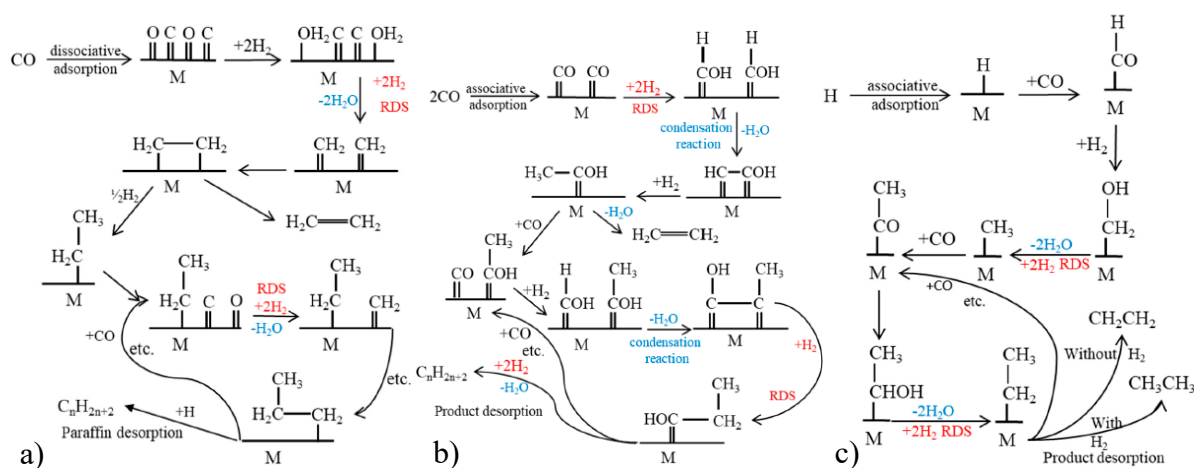


Figure 3 - FTS mechanisms. a) carbide b) enol and c) CO insertion.

Source: Adapted from Shafer et al. (2019)⁴¹ without requiring permission.

The enol mechanism is a route used to explain the formation of oxygenated products. In this pathway, presented in Figure 3b, CO is adsorbed non-dissociatively on metal sites and undergoes partial hydrogenation by absorbing H atoms, resulting in an enol structure of hydroxymethylene, which is the key intermediate. This structure grows through a series of condensation and water elimination steps involving the hydroxyl groups of neighboring hydroxymethylene species.^{41,49}

Finally, CO insertion is another route proposed to explain the wide range of products formed in FTS. In this mechanism, presented in Figure 3c, CO is molecularly adsorbed onto the metal sites leading to a carbonyl molecule, which is the key intermediate monomer. Initially, CO hydrogenation forms an alkyl compound, and subsequent chain growth occurs through the insertion of carbonyl monomers into the metal-alkyl bond. The desorption step can occur with

or without the involvement of H-adsorbed atoms, yielding paraffins and olefins products, as in the carbide mechanism.⁴¹

2.3.2 Reaction kinetics

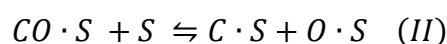
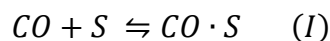
The complexity of FTS mechanisms makes the kinetic assessment of this reaction a challenging study. Kinetically, FTS reaction can be divided into two main steps: the formation of $-CH_x-$ or $-COH_x-$ monomer, known as the hydrogenation step of CO, and the chain growth, which can be classified as the polymerization step. The majority of kinetic studies in literature show that the monomer formation is significantly slower than the polymerization step.⁵⁰

Therefore, the approaches used to derive FTS rate models are focused on the mechanism of reactants adsorption and monomer formation, leading to what is frequently known as lumped kinetics. According to Nikbakht, Mirzaei and Atashi (2018)⁵¹, lumped kinetic models for CO consumption can be expressed using Power-law, Eley-Rideal, or Langmuir-Hinshelwood-Hougen-Watson (LHHW) approaches. Among them, LHHW models have been extensively investigated for CO consumption.⁵¹ Generally, $-r_{CO}'$ expression is represented as function of the partial pressure of reactants and certain products, as shown in Eq. (7).

$$-r_{CO}' = \frac{k (p_{CO})^\alpha (p_{H_2})^\beta}{(1 + \sum_i (K_i p_i^\delta))^\varepsilon} \quad i = CO, CO_2, H_2 \text{ or } H_2O \quad (7)$$

In which, r_{CO}' is the carbon monoxide consumption rate, p is the partial pressure of the component i , k is the reaction kinetic constant, K_i the adsorption equilibrium constant of the component i , and α , β , γ , δ and ε are the coefficients that differentiate the models for each mechanism: type of adsorption of the reactants, number of sites on the reaction step and presence of vacant sites on the catalyst surface.

The adsorption study of H_2 and CO over the metals is crucial for understanding the kinetic models of CO consumption in FTS. It is known that both associative and dissociative adsorption of CO can occur over a metal surface. However, according to Van der Laan (1999)⁵² CO dissociates on most of the transition metals used for FTS at high temperatures and pressures. It has been also reported that the associated adsorption of CO can be a precursor state to dissociation of this molecule into carbidic species as in Eqs. (I) and (II):



After CO adsorption, its dissociation can occur either directly or via H-assisted path, as summarized in Figure 4. Subsequently, the mechanisms diverge based on the type of monomer considered to initiate the propagation/polymerization step, which is typically faster than the initial step.

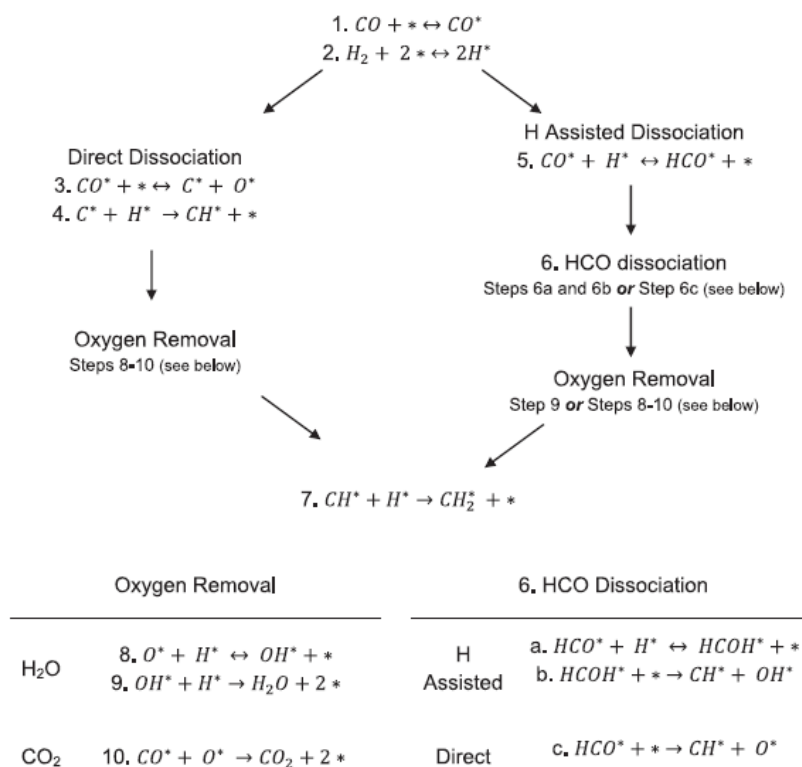


Figure 4 - Possible mechanistic routes for FTS.

Source: Reproduced from Okeson et al. (2016)⁵⁰ with permission from Elsevier.

For hydrogen molecules, the reaction step occurs after their dissociative adsorption on most transition metals. However, the metals can exhibit varying adsorption strengths for both CO and H₂. A study by Vannice (1975)⁵³ on unsupported metals showed that there is a trend in adsorption strength between CO and H₂ molecules within Group VIII B metals: those that strongly adsorb CO tend to exhibit weaker adsorption of H₂, as shown in Figure 5. When the heats of adsorption for H₂ and CO are comparable, hydrogen competes more effectively with CO for adsorption sites, resulting in nearly equal surface coverages of these two gases. Conversely, competition for sites is less favorable when there are significant disparities in the heat adsorptions between the molecules.

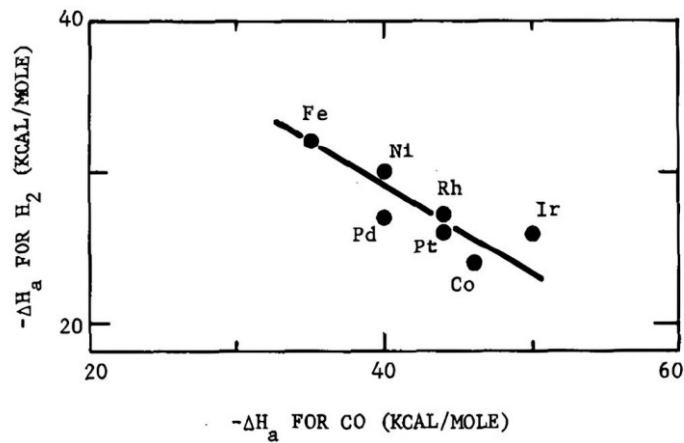


Figure 5 - Variation of H₂ chemisorption with CO chemisorption on group VIII B metals. Source: Reproduced from Vannice (1975)⁵³ with permission from Elsevier.

2.4 PRODUCT DISTRIBUTION AND SELECTIVITY

In addition to the proposed mechanisms for FTS, it is widely accepted that its products follow the polymerization distribution model of Anderson-Schulz-Flory (ASF), presented in Eq. 8. This model assumes that the mass fraction, w_n , of each hydrocarbon with carbon number, n , is dependent on a chain growth probability factor, α . The α -value is a function of the molar rate of chain propagation, r_p , and the molar rate of chain termination, r_t , as shown in Eq 9. Figure 6 presents the expected distribution of products based on the α -value.⁵⁴

$$w_n = n(1 - \alpha)^2(\alpha)^{n-1} \quad (8)$$

$$\alpha = \frac{r_p}{(r_p + r_t)} \quad (9)$$

Given the product distribution model, one of the current challenges in the FTS process is to ensure the selectivity of long-chain hydrocarbons. The maximum selectivity for liquid fuels such as gasoline (C₅-C₁₁), jet fuel (C₈-C₁₆), and diesel (C₁₀-C₂₀) is evaluated to be 48%, 41%, and 40%, respectively⁵⁵, according to the ASF model. These values are indirectly related to the reaction conditions, reactor design, and catalyst formulation (most explored in the literature). Thus, the ASF model serves as a guide for evaluating the characteristics of different catalysts, so that deviations from the model show the effects that the catalyst has on product distribution.⁴¹

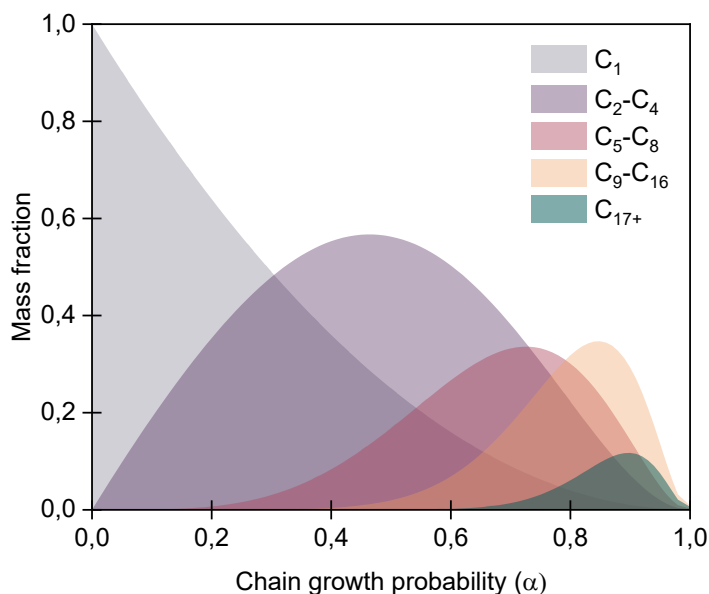


Figure 6 - Product selectivity in FTS according to ASF model.

Eq. 8 is frequently presented in the logarithmic form in order to calculate the α -value from the hydrocarbon mass fraction, as shown in Eq. 10. Kinetically, the ASF model is valid for FTS assuming a constant kinetic environment at each catalytic site during the reaction. However, it is acknowledged that this condition is not achieved, which sometimes makes hydrocarbons fraction different to the expected from the model, especially for CH_4 .⁵⁴

$$\ln\left(\frac{w_n}{n}\right) = n \ln(\alpha) + \ln\left(\frac{(1-\alpha)^2}{\alpha}\right) \quad (10)$$

Methane selectivity is usually higher than predicted. This can be explained by the existence of methanation active sites on the catalyst, or by the nature of FT mechanism, since the combination of two $-\text{CH}_2-$ species is more difficult than the hydrogenation of the CH_2 -Metal intermediates.⁵⁶ On the other hand, C_2 - C_4 selectivity is often lower than predicted by ASF. In this case, the variation is attributed to the incorporation of C_2 - C_4 olefins into other chains.^{35,57} As a result, the ASF plots from Eq 10 usually exhibit curved profiles instead of straight lines.⁵⁴

Overall, the selectivity on FTS depends on the ability of the catalyst to maintain a balance between the adsorbed reactants and products. This equilibrium is a function of the electron density on the metallic surface, which is adjusted by the transfer of electrons between the catalyst and the antibonding orbital of the CO molecule.²⁴

Finally, the ASF model has limitations in predicting the product distribution of bifunctional catalysts as it only considers the polymerization reactions occurring on the metallic surface.³⁵ A bifunctional catalyst for FTS comprises an active metal phase for hydrocarbon chain growth, and a designed support suitable for secondary reactions, such as C-C cleavage of

heavy hydrocarbons. Thus, the model with a single chain growth probability factor fails to predict the occurrence of side reactions. Li et al. (2018)⁵⁸ proposed a modification to the ASF model by introducing a second chain growth parameter, accounting for the support cracking ability³⁵. The modified distribution exhibited a better fit with the experimental selectivities observed for bifunctional catalysts.

2.5 OPERATING CONDITIONS IN FTS

The results of CO conversion and product selectivity in FTS are highly influenced by reaction conditions, such as temperature, pressure, space velocity, and feed composition.⁵⁹ Therefore, an appropriate investigation of the operating conditions is essential for optimizing the FTS results.

2.5.1 Effect of temperature

Temperature significantly influences CO conversion and product selectivity in FTS due to the inherent polymerization-like mechanism of these reactions⁶⁰. Typically, an increase in temperature favors the activation of CO molecules on the catalytic sites, leading to more available C atoms on the surface to react with hydrogen⁶¹. Thus, augmenting temperature has a positive effect on catalytic activity and CO conversion.

Liu et al. (2007)⁶² observed a 14% increase in CO conversion when the temperature rose from 260°C to 290°C for a Fe-Mn catalyst. Similarly, Akbarzadeh et. al (2020)⁶³ reported a 20% increase in CO conversion with a Co-Mn catalyst at temperatures ranging from 220°C to 280°C. However, higher temperatures can lead to catalyst deactivation. Li et al. (2022)⁶⁴ found that a precipitated iron catalyst operating at 290°C exhibited a 15 times higher deactivation rate constant than catalysts operating at 270°C, due to sintering and surface oxidation of carbides on the catalyst.

In the product selectivity, elevated temperatures shift the product distribution towards shorter chains³⁸. During the polymerization mechanism, temperature has a stronger influence on the termination rate of the reaction compared to the propagation rate, as the desorption step is an endothermic process. Additionally, higher temperatures accelerate hydrogenation, which contributes to chain termination. Consequently, increased temperature leads to a reduction in the α value of the ASF distribution model.⁵⁶

In industrial applications, the FT process is typically classified into two operational modes: Low-Temperature Fischer-Tropsch (LTFT) synthesis and High-Temperature Fischer-Tropsch (HTFT) synthesis.⁶⁰ The operating temperature of each process depends on the metal active site, but generally, LTFT occurs at a maximum temperature of 240°C, whereas HTFT at 350°C.⁶⁵ The product spectra are different from both processes. LTFT primarily yields diesel and waxes, with approximately 50% of syncrude mass in C₂₂ and heavier wax fraction, consisting mainly of linear paraffins and α -olefins.⁶⁰ In contrast, HTFT produces lighter hydrocarbons, predominantly linear and olefin-rich compared to LTFT.⁶⁶

2.5.2 Effect of pressure

Operating pressure influences FT activity by increasing adsorbed carbon species on the surface, increasing reactant collision probability and CO conversion.⁶⁷ According to Todici et al. (2016)⁵⁹, this effect is more significant in Co-based catalysts compared to Fe-based ones. Studies by Akbarzadeh et al. (2020)⁶³ and Liu et al. (2007)⁶² demonstrated a rise in CO conversion of 37% and 32%, respectively, when the pressure rose from 1 atm to 20 atm and from 9 atm to 25 atm, respectively. However, similar to the effect of temperature, excessively high pressures can lead to aggregation and the sintering of active metals.

The effect of pressure on the product selectivity in FTS is still a topic of discussion in the literature. In general, there is a consensus that increasing pressure results in lower selectivity to CH₄, while increases C₅₊ selectivity⁶⁸. This effect is explained by the increase in the α -value at high total pressures. Kinetically, an increase in operating pressure reduces the ratio of H₂/CO adsorbed species, which causes a diminution in chain termination by hydrogenation of C_n species.⁶⁹

2.5.3 Effect of syngas composition and space velocity

The feed H₂/CO molar ratio in FTS significantly influences the product selectivity. As the reaction progresses and long-chain hydrocarbons are formed, the utilized H₂/CO approaches 2, due to the inherent chemical composition of the products (C_nH_{2n+2}, C_nH_{2n}).⁵⁶ Additionally, an increase in H₂/CO enhances the hydrogenation activity, thereby increasing the selectivity towards CH₄ and lighter hydrocarbon chains, while the selectivity to C₅⁺, oxygenates, and alkenes decreases.³⁸

Osa et al. (2011)⁶¹ investigated the effect of syngas composition on FTS over a Co/Al₂O₃ catalyst. CO conversion increased from 6.6% to 25.6% while CO₂ and C₅⁺ selectivities decreased when the H₂/CO ratio was augmented from 0.5 to 2.0. A similar trend was noted by Liu et al. (2007)⁶² with Fe-Mn catalyst. Additionally, higher hydrogen partial pressures weaken the WGS reaction, decreasing CO₂ selectivity. Consequently, as Fe catalysts exhibit greater WGS activity compared to Co catalysts, the feed H₂/CO is usually below 2, depending on the operating temperature.³⁷

The space velocity also influences CO conversion and the occurrence of secondary reactions. Typically, CO conversion decreases with the increase in space velocity due to the shortened contact time between syngas and the active sites. Additionally, at higher flow rates, the re-adsorption of formed olefins decreases, leading to increased selectivity towards alkenes. Osa et al. (2011)⁶¹ investigated the effect of space velocity on FTS using a Co/Al₂O₃ catalyst. They observed a 30% decrease in CO conversion and an almost 8% decrease in C₅⁺ selectivity when the space velocity increased from 4000 h⁻¹ to 12000 h⁻¹.

2.6 REACTORS FOR FTS

The reactor design for FTS is crucial for achieving optimal CO conversion and product selectivity. FTS reactions are highly exothermic, making heat removal essential to prevent overheating, methanation, coke deposition, and catalyst deactivation. Additionally, the presence of multiple phases (solid, liquid, and gas) adds complexity to the reactor setup. Currently, common commercial-scale FTS reactors including fixed-bed, slurry-bed, and fluidized-bed configurations, as depicted in Figure 7, have been developed, with significant contributions from Shell and Sasol companies since 1936.^{24,38,70}

The fixed-bed reactor is a widely used configuration for FTS processes. Currently, it is employed in the multi-tubular form at industrial scale for LTFT. The system consists of a vessel with long narrow tubes containing catalysts, in which syngas and products flow vertically. Heat exchange is achieved through contact between the tube walls and the water in the vessel, resulting in steam generation.²⁵

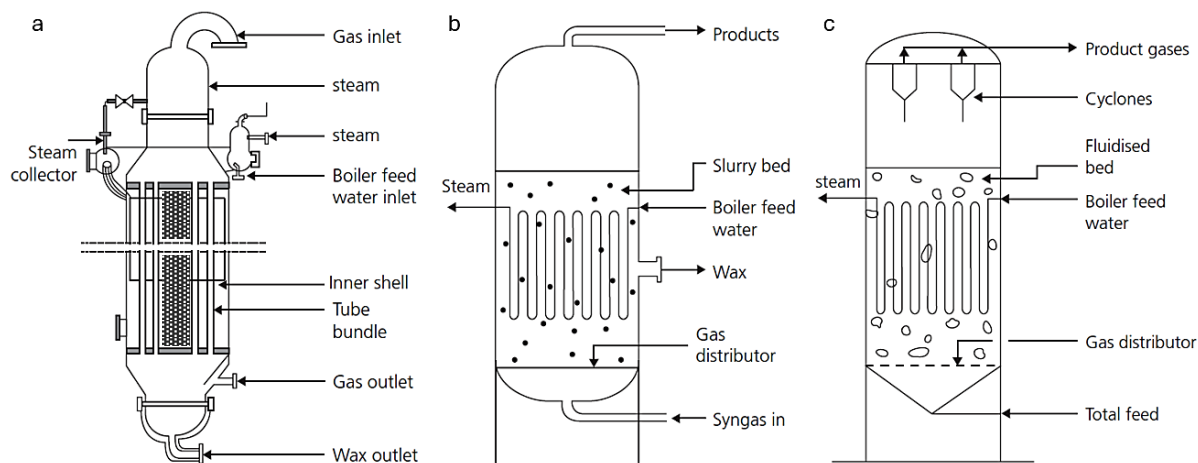


Figure 7 - Schematics of FTS reactors. a) fixed-bed, b) slurry-bed, c) fluidized bed.
Source: Reproduced from Gnanamani et al. (2016)⁷¹ with permission from Elsevier

This type of reactor is also the most used for bench-scale studies due to its operational simplicity. The main advantage is the easy separation of the products from the catalyst. However, challenges include heat removal, leading to temperature gradients and difficulties in controlling selectivity, as well as the formation of hot spots along the bed.¹⁰ Moreover, other drawbacks such as high-pressure drop and intra-particle diffusion limitations limit its application.³⁸

Slurry-bed reactors are an alternative to fixed-bed for LTFT processes, consisting of a vessel containing a slurry dispersed with catalysts within the produced FT wax. Hydrocarbons form as syngas bubbles rise through the slurry, collecting light components in the upper section, while heavy liquid hydrocarbons concentrate at the bottom of the vessel²⁵. Efficient heat exchange occurs between the well-mixed slurry and internal cooling tubes, ensuring precise temperature control, higher CO conversion, and α -values. This reactor type offers advantages such as low-pressure drop and uniform temperature profiles. Challenges include continuous catalyst-liquid separation demand and the high viscosity of slurries.^{10,38}

Fluidized-bed reactors provide a solution to heat transfer limitations observed in fixed-bed systems for FTS. Similar to slurry-bed systems, internal cooling tubes dissipate heat, generating steam and enabling isothermal operation with improved selectivity control. The main drawback of this reactor type is liquid products adherence to catalyst particles, leading to agglomeration. To counter this, elevated temperatures are applied, making fluidized-bed reactors suitable for HTFT processes.³⁸

Finally, in addition to industrial reactors, the literature presents several research efforts focused on designing novel FTS reactors, including small-scale multi-tube⁷², microstructured⁷³, and membrane reactors.⁷⁴

2.7 CATALYSTS FOR FTS

Good Fischer-Tropsch catalysts must have metals with adsorption ability for both CO and H₂ molecules. Typically, H₂ activation involves its dissociation into reactive atomic species, while CO activation can occur by non-dissociative or dissociative adsorption. Moreover, H₂ dissociation on transition metal surfaces is usually easier than CO dissociation. As a result, the catalyst activity in the FT synthesis is predominantly determined by its capability to activate CO.⁷⁵

The activation of CO on metal surfaces involves the bonding of its 5σ (HOMO) and 2π* (LUMO) orbitals with the metal d-band. Certain transition metals in the periodic table exist in reducible oxide forms, while others do not, affecting their ability to adsorb CO, as shown in Figure 8. Moreover, the activation energy for carbon-oxygen separation is primarily influenced by the electronic nature of the metal, rather than the metal surface geometry. Despite, the surface geometry may determinate whether the CO adsorption is dissociative or non-dissociative at specific temperatures.⁷⁵

IIIB	IVB	VB	VIB	VII B	VIII B	VIII B	VIII B	IB	IIB
Sc	Ti	V	Cr	Mn	Fe	Co	Ni	Cu	Zn
Y	Zr	Nb	Mo	Tc	Ru	Rh	Pd	Ag	Cd
La	Hf	Ta	W	Re	Os	Ir	Pt	Au	Hg

Figure 8 - Behavior of transition metals in FTS

Source: Adapted from Perego et al. (2009)⁷⁶ with permission from Elsevier.

Certain metals in groups VIII B and IB, such as Cu and Pd, exhibit low adsorption heat, enabling non-dissociative CO adsorption, suitable for methanol synthesis from syngas. Conversely, transition metals on the left side of the periodic table, such as W and Mo, tend to adsorb CO dissociatively but have poor H₂ adsorption, making them inactive for FTS. Meanwhile, metals such as Fe, Co, Ni, and Ru exhibit moderate CO adsorption strength, making

them appropriate for CO hydrogenation according to the Sabatier's principle. Among these metals, Fe and Co are the most studied and used industrially, Ru has a high cost, despite being more active, and Ni favors the hydrogenation instead of C-C coupling, leading to the major formation of methane.⁷⁵

Nowadays, commercial Fischer-Tropsch plants is limited and concentrated in Africa, Asia, and in the Middle East, as shown in Table 1. These plants utilize technologies developed by either Shell or Sasol companies with commercial catalysts of pure Fe or Co supported on Al₂O₃ or SiO₂.⁷⁷ Research studies in the literature also focus on the catalyst design using Co and Fe as active metals, as well as exploring the effects of using different supports and promoters on the FTS results.

2.7.1 Co-based catalysts

In general, Co-based catalysts exhibit higher stability and selectivity toward long-chain hydrocarbons when compared to Fe-based catalysts. These catalysts produce more linear n-paraffins compared to Fe, resulting in a lower olefin/paraffin ratio.⁵ FTS processes utilizing cobalt catalysts can operate at lower temperatures than those with iron catalysts, making cobalt more suitable for LTFT. Conversely, Co-based catalysts are more sensitive to variations in operating conditions, leading to changes in the product selectivity.³⁸ Table 2 presents a comparison of key characteristics between Co and Fe-based catalysts for FTS.

FTS reactions are significantly affected by catalyst nanoeffects, and recent studies have explored the influence of active phases and particle size on FT activity. In Co-based catalysts, the metallic crystalline forms α -Co (hcp) and β -Co (fcc) are the active sites for CO conversion.⁵ Co carbides such as Co₂C and Co₃C have also been observed in spent catalysts, but these phases are related to alcohol formation as they facilitate CO insertion during chain growth.³⁸

Table 2 - Comparison of some characteristics of Co and Fe-based catalysts for FTS

Parameter	Co-based catalyst	Fe-based catalyst
	• 190-240°C.	• 200-350°C.
Operating temperature	• Used in LTFT. • High temperature increases CH ₄ selectivity and catalyst deactivation.	• Used in LTFT and HTFT.
Feed gas	• H ₂ /CO ratio of 2.0-2.3 (poor WGS activity).	• Flexible H ₂ /CO ratio, 0.5-2.5 (high WGS activity).
Activity	• More active at lower space velocities.	• More active than Co at higher space velocities.
Product spectrum	• Primary products are n-paraffins, marginal production of α -olefins. • Higher paraffin/olefin ratio.	• Primary products are n-paraffins, considerable production of α -olefins. • Lower paraffin/olefin ratio.
Resistance	• Longer lifetime.	• Shorter lifetime.

Source: Adapted from Ail and Dasappa (2016)⁷⁸ with permission from Elsevier.

2.7.2 Fe-based catalysts

Fe-based catalysts are known to operate under flexible conditions in FTS, being used in processes at both low and high temperatures. Fe catalysts exhibit WGS activity under FTS conditions, making them suitable for H₂-poor syngas processes.⁷⁹ According to Shafer et al. (2019)⁴¹, Fe-based catalysts exhibit a more diverse product distribution, showing significant selectivity towards acids, aldehydes, ketones, and isomerized products compared to Co and Ru catalysts.

Typically, Fe catalysts undergo a reduction step before set to FTS conditions, since it exhibits different oxidation states. Hematite (Fe₂O₃) is the most stable oxide of Fe, being reduced into magnetite (Fe₃O₄), iron oxide (FeO) and/or metallic iron (Fe) under H₂ flow. Then, the reduced iron species can be carburized to produce iron carbide species, which are the active sites for hydrocarbons chain growth in FTS, as shown in Figure 9a.⁷⁹

The carbide species are formed as small nodules (nucleation) on the surface of Fe₃O₄, FeO, or Fe when CO is in contact with the catalyst. Moreover, the carburization and carbide

oxidation processes are significantly influenced by the FTS environment, where H₂O or CO₂ formed may influence on the amount of iron carbides and iron oxide species over the catalyst surface.⁷⁵

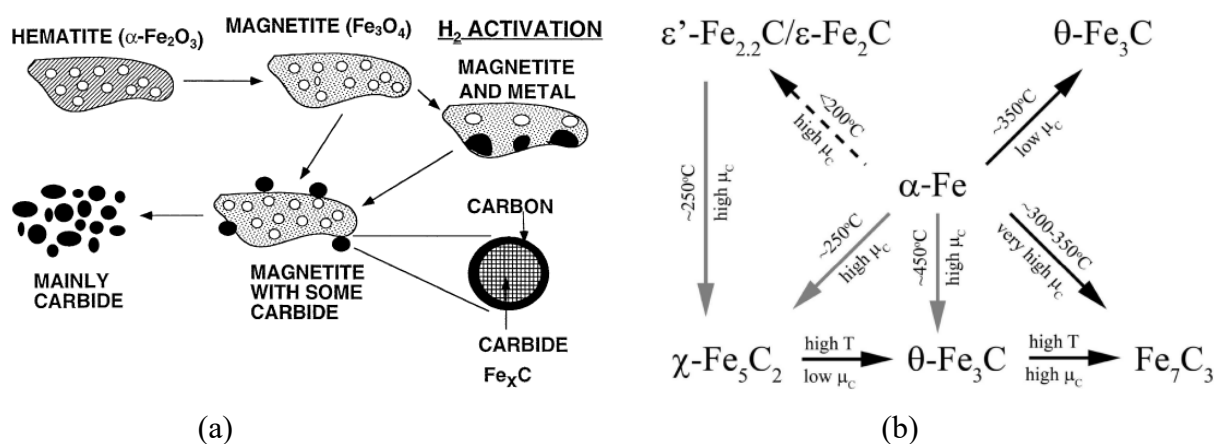


Figure 9 – Fe particles in FTS a) phase transformations. b) iron carbide phases.
Source: reproduced from a) Shorff et al. (1995)⁸⁰ b) Smit et al. (2010)⁸¹ with permissions from Elsevier and American Chemical Society.

Iron carbides play a crucial role in the chain growth and can exist in various phases, such as χ -Fe₅C₂ (Hägg carbide), θ -Fe₃C, Fe₇C₃, ε -Fe₂C, and ε' -Fe_{2.2}C₇. Currently, there is a debate in the literature to determine which species are active, but in most cases, the catalytic performance is associated to the χ -Fe₅C₂ content of the catalysts. Some studies suggest that θ -Fe₃C is inactive, while others report its activity for FTS at high temperatures.⁸²

Shorff et al. (1995)⁸⁰ evaluated the effect of different pretreatment gases (CO, H₂, and CO/H₂) on unsupported iron oxide catalysts. The study showed that when the catalysts are exposed to the FTS environment, iron oxides transform into multiple carbide phases, irrespective of the activation step. Similarly, Smit et al. (2010)⁸¹ investigated the effect of treating α -Fe₂O₃ with pure CO and CO/H₂ on catalyst phases. XRD patterns showed that the CO-treated sample exhibited 90% χ -Fe₅C₂ phase formation, whereas the syngas-treated sample showed 56%.

Smit et al. (2010)⁸¹ also investigated the transformations between ε - χ - θ carbide phases, as shown in Figure 9b. The study revealed that the formation of θ -Fe₃C, χ -Fe₅C₂, and ε -carbides can be explained based on their relative thermodynamic stability, with the carbon chemical potential playing a significant role in determining their formation⁸¹. Additionally, it is known that the carbide species χ -Fe₅C₂ and θ -Fe₃C are oxidized to Fe₃O₄ during the FTS reaction, and both FTS and WGS activities depend on the percentage of each phase present in the catalyst.⁷¹

2.7.3 Effect of promoters

Promoters for FTS catalysts are categorized as reduction, alkali, or structural promoters, enhancing metal reducibility, stability, and mechanical strength^{83,84}. Promoters can favor CO hydrogenation and enhance liquid products selectivity, as observed by Uykun Mangaloglu et al. (2018).⁸⁵ Their study showed that K/Cu/Mn addition in an Fe/zeolite catalyst increased the selectivity to diesel/gasoline hydrocarbons from 48% to 64-79%.

Several metals, including Pt, Ru, Au, and Cu, are known to facilitate the reduction of iron catalysts. Among these, Cu is a cost-effective metal extensively investigated as a promoter for FTS catalysts⁸³. Cu-promoted Fe₂O₃ catalysts are reduced to Fe₃O₄ at much lower temperatures than Cu-free Fe₂O₃ catalysts. Initially, copper oxide is reduced to metallic copper, and subsequently, hydrogen spillover occurs from metallic copper to adjacent iron oxides, facilitating their reduction and the carburization step, leading to improved FTS performance.⁸³

Alkali promoters, particularly K, significantly influence FTS results, being a cost-effective and optimal promoter.⁸³ Heavier alkali metals favor light hydrocarbon formation.⁸³ Several studies^{86,87, 88} showed that potassium promotion enhanced Fe catalyst carburization, increasing C₅₊ selectivity. The reduction facilitation follows a mechanism similar to that observed with Cu, where hematite is easily reduced to magnetite in an electron-enriched environment, leading to an efficient carburization of particles in iron carbide phases for CO activation and chain growth.⁸³

2.7.4 Effect of catalyst supports

The selection of the support in catalyst design is crucial for achieving high FTS activity and selectivity. The support can disperse the active phase, modify its electronic properties, avoid overheating and enhance the catalyst mechanical strength.⁸⁹ The interaction between the support and the metal phase also influences the metallic reduction process. A too weak interaction leads to poor metal dispersion and formation of metallic agglomerates, while too strong interaction hinders the reduction process. Therefore, reaching an optimal balance in this interaction is essential to ensure superior catalyst performance.⁹⁰

Generally, the most studied supports for FTS can be divided into groups: silica/alumina-based supports, metal oxides, carbon-based supports, zeolites, and MOFs. Among these, SiO₂ and Al₂O₃ have been extensively investigated in literature due to their high surface area and porous sizes, which improve the active phase dispersion and catalytic activity.

Jun et al. (2004)⁹¹ studied Fe-K-Cu catalysts supported on SiO₂ and Al₂O₃ for FTS using CO₂-rich syngas. The authors reported that alumina improved the distribution of Fe, Cu, and K, compared to the SiO₂ support. The Al₂O₃-supported catalyst exhibited higher carbide content and achieved a greater selectivity for middle distillates (21%) compared to the SiO₂-supported catalyst (9%). Similarly, Kang et al. (2013)⁹² reported that Al₂O₃-supported Fe catalyst exhibited better reducibility and carbidization, which led to a two times higher CO conversion compared to the SiO₂-supported catalyst. On the other hand, the selectivity for heavy hydrocarbons was favored on the SiO₂ support (64%) compared to Al₂O₃ (38%).

Lu et al. (2021)⁹³ also compared SiO₂ and Al₂O₃ supports with Fe₂O₃ as catalysts for FTS. The CO conversion of Fe/Al₂O₃ catalyst was 3.3 times higher than that of the unsupported Fe catalyst. The results demonstrated a higher selectivity towards heavy hydrocarbons for the Al₂O₃-supported catalyst (49%) compared to the SiO₂-supported catalyst (37%), consistent with the findings reported by Jun et al. (2004).⁹¹ Moreover, SiO₂ and Al₂O₃ supports affected the electronic state of iron atoms, in which Fe-Si or Fe-Al interactions facilitated the formation of C-rich iron carbide (ϵ -Fe₂C), as observed via XPS analysis.

Mesoporous materials, such as SBA-15 and MCM-41, have also been studied as potential supports for FTS due to their well-defined pore sizes and high surface areas. These materials are often preferred over microporous, as excessively small pores limit reactant diffusion. Additionally, larger pore sizes enhance the metal reducibility and prevent 1-olefin readsorption, promoting the formation of heavier hydrocarbons.⁹⁴

Cheng et al. (2015)⁹⁵ studied the effect of pore size using MCM-41 as Fe catalyst support on FTS. The efficiency of Fe nanoparticles depended on the degree of iron carbidization. Higher dispersion of iron oxide on smaller pore mesoporous silicas led to poorer CO hydrogenation due to lower iron reducibility and reduced concentration of iron carbide species. On the other hand, catalysts with larger pore sizes exhibited superior catalytic performance, attributed to the presence of larger iron nanoparticles.

A similar behavior was observed by Xiong et al. (2008)⁹⁶ who studied Co/SBA-15 catalysts with different pore sizes for FTS. They observed that Co particles were distributed on both exterior and interior surfaces after reduction in the larger pore supports. The support with a larger pore diameter (~15 nm) led to larger cobalt clusters when compared to supports with a smaller pore diameter (~4 nm), which favored CO adsorption and its hydrogenation.

Carbon-based materials, including reduced graphene oxide (rGO), carbon nanofibers (CNFs), carbon nanotubes (CNTs) and carbon spheres (CSs), have also been studied as catalyst supports for FTS. It is believed that their nanoporous structure increase the selectivity toward

heavier hydrocarbons and their chemical composition facilitates the formation of carbides on iron-based catalysts.⁹⁷

Valero-Romero et al. (2021)⁹⁷ and Chen et al. (2008)⁹⁸ observed enhanced Fe reduction and carbidization in carbon-based supports under FTS conditions, due to the support chemical composition and low metal-support interaction. Similarly, Chen et al. (2008)⁹⁹ and Yu et al. (2010)¹⁰⁰ observed enhanced iron carbide formation with Fe in confined structures (CNTs and CSs), promoting C₅₊ selectivity. These findings corroborate with DFT calculations¹⁰¹ indicating weaker iron binding located inside carbon nanotube walls.

2.8 ZEOLITES AS CATALYST SUPPORT FOR FTS

Zeolites are crystalline porous solids structured with AlO₄ and SiO₄. The tetrahedra are interconnected to form rings and blocks, which are differently arranged resulting in distinct three-dimensional frameworks with well-defined channels and cavities, as shown in Figure 10. These materials exhibit acid properties, characterized by the presence of both Lewis acid sites, originated from the electronic state of Al in the framework, and Bronsted acid sites, where protons compensate the negative charge associated with Al atoms.^{102,103}

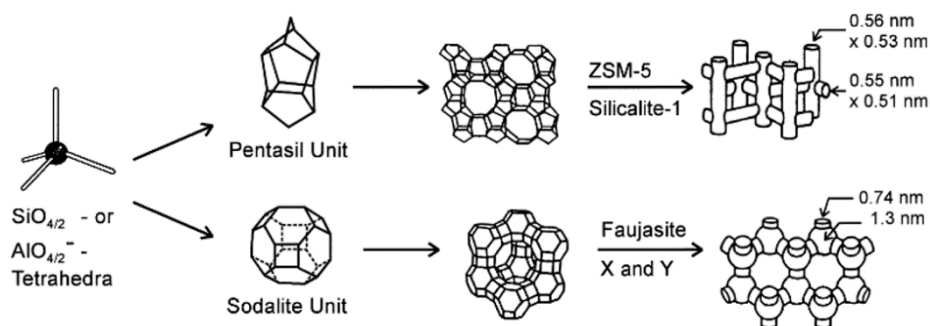


Figure 10 - Structures of zeolites Y and ZSM-5

Source: Adapted from Weitkamp (2000)¹⁰⁴ with permission from Elsevier

In the FTS studies, zeolite-supported catalysts are bifunctional catalysts, with active metals promoting hydrocarbon chain growth and acid sites facilitating secondary reactions, as shown in Figure 11. The carbonic chains may undergo hydrocracking or oligomerization when interact with acid sites, influencing selectivity toward specific hydrocarbon ranges.^{105,106} However, optimal acidity is crucial, since excessive acidity can lead to an over-cracking effect, favoring methane and short-chain hydrocarbon production.

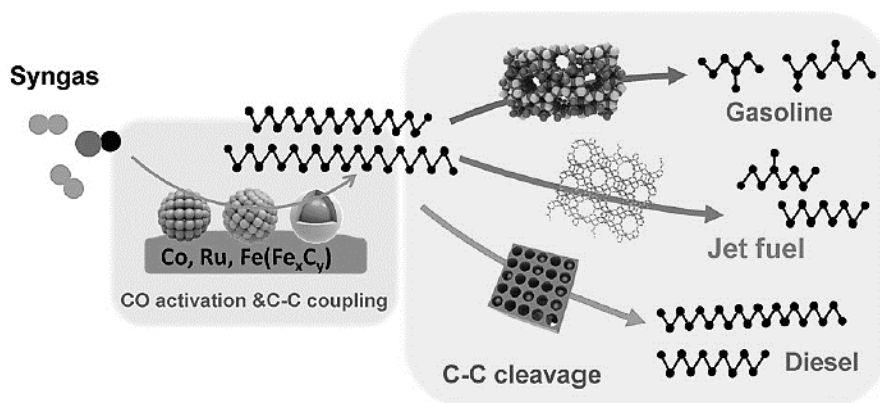


Figure 11 - Bifunctional catalysts for Fischer-Tropsch synthesis

Source: Reproduced from Zhou et al. (2019)¹⁰⁷ with permission from Elsevier.

Zeolite porosity influences the product selectivity in FTS. Long and small micropores can create diffusional resistance for products inside the channels, affecting secondary reactions. The structure can also confine metal particles, limiting molecular access and product diffusion, leading to over-cracking of chains and a higher selectivity for light hydrocarbons (C_2 - C_4).¹⁰⁸

In the literature, several zeolites have been tested as supports for Fe and Co catalysts in FTS. Most studies focus on investigating the effects of zeolite acidity and porosity in FTS. In general, zeolite-supported catalysts yield different product spectrum from classical straight-chain FTS products due to shape selectivity and acidic site-driven secondary reactions.¹⁰⁹

Bessel (1993)¹¹⁰ compared Co catalysts supported on zeolites (ZSM-5, Y, mordenite, and bentonite) with SiO_2 and Al_2O_3 supports for FTS. The study showed that SiO_2 and Al_2O_3 favored unbranched hydrocarbons, while acidic supports, such as ZSM-5, exhibited higher selectivity to gasoline-range products and more branched hydrocarbons. A subsequent study by Bessel (1995)¹¹¹ concluded that internal acid site accessibility in zeolite had a greater impact on cracking and isomerization reactions than the strength or concentration of acid sites.

Botes and Bohringer (2004)¹¹² investigated Fe/HZSM-5 catalyst acidity in FTS. The study showed that low acidity of HZSM-5 (Si/Al: 140) enhanced C_5 - C_{11} selectivity from 25% to 35%, compared to unsupported Fe catalyst. In contrast, highly acidic zeolite (Si/Al:15) caused rapid catalyst deactivation and higher selectivity for light paraffins. This corroborates with the study of Plana et al. (2016)¹¹³, which showed that highly acid Fe/HZSM-5 catalyst reduced selectivity towards C_{5+} compared to less acidic catalysts. Remarkably, the authors also found that zeolites presented little effect on side WGS reaction, indicated by similar CO_2 selectivity across different supports evaluated.

Concerning zeolite porosity, Cheng et al. (2015)¹⁰⁸ studied Co catalysts on mesoporous HZSM-5 zeolite. The study showed that the use of H-meso-ZSM-5 instead of traditional microporous H-ZSM-5 significantly suppressed the formation of C₁-C₄ hydrocarbons. This corroborates with the study of Plana et al. (2016)¹¹³, who reported that desilicated Fe/HZSM-5 catalysts, presenting mesopores, exhibited higher selectivity to hydrocarbons due to the enhanced metal particle accessibility. Similarly, Peng et al. (2015)¹¹⁴ observed increased selectivity to long carbon-chain hydrocarbons in FTS with mesoporous Y zeolite as support for Co nanoparticles, reaching 60% for diesel fuel compared to 47% with microporous zeolite.

The synthesis method is also important for catalyst performance in FTS, since it can influence metal-support interaction and metal confinement in the zeolite framework. Weng et al. (2007)¹¹⁵ found that Fe/LiY-zeolite catalysts prepared via incipient wetness impregnation exhibited superior Fe dispersion, and C₅₊ selectivity compared to wet impregnation and physical mixing methods. Similarly, Baranak et al. (2013)¹¹⁶ observed higher catalytic activity (52%) and C₅₊ selectivity (50%) for impregnated Fe/ZSM-5 catalysts compared to the catalyst prepared by physical mixing (43% and 45%, respectively).

Metal/zeolite catalysts with core-shell structure have been discussed in the literature concerning their effects in FTS. Zhou et al. (2019)¹⁰⁷ reported that metal/zeolite core-shell structure favors the tandem reactions of chain growth and isomerization, leading to a higher selectivity of C₅₊. This corroborates with Liu et al. (2021)¹¹⁷ who observed facilitated Fe₅C₂ carbide formation in confined Fe@zeoliteY compared to impregnated catalysts. Conversely, Amoo et al. (2020)¹¹⁸ reported increased selectivity towards light hydrocarbons when iron nanoparticles were confined within zeolite Y.

Overall, zeolites have been studied as promising bifunctional supports for FTS, with three aspects being commonly evaluated: acidity, porosity, and synthesis method. The addition of promoters on these catalysts has also been studied, as shown in Table 3. In general, a trend is observed for hydrocarbons distribution, with a predominant formation of C₂-C₄ hydrocarbons, followed by C₅₊ and C₁. The catalysts show CO₂ selectivity, from 6.9% to 45%, as Fe catalysts exhibit activity for WGS.

Table 3 - Summary of literature FTS results with Fe/Zeolite catalysts

Catalyst	H ₂ /CO	T	P	WHSV	CO	CO ₂	Hydrocarbon selectivity			ref
							CH ₄	C ₂ -C ₄	C ₅₊	
FeCuK/ZSM-5	2	300	10	2000	81.1	35.6	19.6	42.6	37.8	119
FeCuK/Mor	2	300	10	2000	72.9	37.7	32.2	44.2	23.6	119
FeCuK/ β -Zeolite	2	300	10	2000	63.9	25.2	31.5	50.8	17.7	119
Fe/ZSM-5	2	280	19	750	50.4	16.7	18.8	32.4	48.8	85
Fe@ZSM-5	2	320	10	6000	47.4	24.1	24.8	42.5	32.7	120
FeK@ZSM-5	2	320	10	6000	53.7	20.2	19.8	52.1	28.1	119
Fe@ZSM-5	2	300	20	22500	13.1	8.7	27.1	43.9	28.9	121
Fe/ZSM-5	2	250	1	2200	38.7	11.4	20.2	41.1	38.7	122
FeK/ZSM-5	2	250	1	2200	69.8	10.2	11.8	55.1	33.1	122
Fe@ZSM-5	2	300	10	-	60.4	25.7	33.7	31.1	35.0	123
Fe@Y	2	300	30	-	70.3	41.4	31.7	64.6	3.7	124
Fe/Y	2	300	30	-	48.7	27.8	28.5	25.5	46.0	122
FeMn/ZSM-5	1	320	10	2220	69.9	45.5	24.1	41.6	34.3	125
FeMnCu/ZSM-5	1	320	10	2220	48.3	43.2	23.9	41.9	34.4	125
Fe/HZSM-5	1	280	19	-	72.4	9.0	7.9	14.0	78.1	116
FeMn/ZSM-5	2	280	10	2000	82.2	35.5	20.2	57.5	22.3	126
FeMn@ZSM-5	2	280	10	2000	78.5	28.3	18.7	57.5	23.8	126

T = °C, WHSV = ml h⁻¹ g⁻¹, P = bar, CO conv. and CO₂ sel. (mol %). Hydrocarbon selectivity without CO₂

Comparing the performance of zeolite-based catalysts liquid fuel production is also challenging. Typically, most studies do not individually quantify the hydrocarbons and the chains are grouped into the C₂-C₄ range, with C₅₊ hydrocarbons assumed to represent liquid fuels. However, FTS can produce hydrocarbons with different sizes beyond C₅₊, including fuels, such as gasoline, kerosene, and diesel, but also wax (C₂₀₊). Therefore, accurately quantifying all hydrocarbons in fuel range is crucial for a comprehensive evaluation.

In summary, zeolites have been studied as promising catalyst supports for FTS, especially H-ZSM5. Despite this, there are few research concerning comprehensive studies of Fe/ZSM-5 catalysts addressing a complete catalyst characterization, investigation of varied reaction conditions on catalyst performance, and most notably, the understanding of CO conversion kinetics. Thus, a complete investigation of the mentioned aspects is essential for further optimization studies of Fe/Zeolite-based catalysts for FTS.

3

OBJECTIVES

This study aims to investigate Fe/HZSM-5 catalysts for CO hydrogenation via Fischer-Tropsch Synthesis, exploring their chemical and structural characteristics, as well as their reactional and kinetic effects.

The specific objectives are:

- Perform the synthesis of Fe nanoparticles and their deposition on the HZSM-5 supports.
- Study the characteristics of the prepared catalysts, including structure, crystallinity, metal size, dispersion, and presence of acid/basic sites using different characterization techniques.
- Evaluate the performance of the catalysts in CO conversion for FTS with temperature screening and identify possible deactivation effects.
- Investigate the effects of varied reaction parameters, including support acidity, temperature, space velocity, pressure, and feed composition on CO conversion and liquid hydrocarbons selectivity, as well as the catalyst stability over time on stream.
- Characterize the spent catalysts to assess possible structural modifications and coke deposition.
- Study different kinetic models of CO consumption and estimate the kinetic parameters for the studied catalysts.
- Propose a mechanism of CO consumption over the catalyst surface based on the best fitted model and *in situ* characterization.

4

MATERIALS AND METHODS

This section presents the details of experimental procedures undertaken in this study. Initially, the description of materials and methods used for the synthesis of the catalysts is presented. Then, it is given the detailed information on the techniques and parameters used for catalyst characterization. Subsequently, the experimental setup and conditions employed for catalyst testing in Fischer-Tropsch synthesis are described. Finally, the methods utilized for kinetic assessment experiments and subsequent parameter estimation are outlined.

4.1 CATALYST PREPARATION

The present study was conducted as part of a collaborative project involving seven research institutions. The catalysts studied in this work were prepared at the CamargoLab laboratory, at the Inorganic Chemistry Department of the University of Helsinki, Finland.

4.1.1 Materials

Zeolites HZSM-5 with $\text{SiO}_2/\text{Al}_2\text{O}_3$ ratios of 52, 91, and 371 were acquired from ACS materials[®]. The technical datasheet from ACS reports that all zeolites were prepared by conventional hydrothermal methods and present a sphere-shape with a BET surface area $>362 \text{ m}^2/\text{g}$. For preparation of Fe_3O_4 nanoparticles (NPs) it was used: $\text{FeCl}_2 \cdot 4\text{H}_2\text{O}$ ($>99\%$) and $\text{FeCl}_3 \cdot 6\text{H}_2\text{O}$ ($>98\%$) from Sigma-Aldrich, HCl (37%) from VWR chemicals, and NaOH (99%) from VWR chemicals.

4.1.2 Catalyst preparation

The catalyst preparation method used in this work is an adaptation from Wei et al. (2017)¹²⁷. Initially, the Fe_3O_4 NPs were synthesized separately. Then, the metal loading methods of dry impregnation (DI) and physical mixing (PM) were used with the HZSM-5 with a $\text{SiO}_2/\text{Al}_2\text{O}_3$ ratio of 91. These samples were denoted by the codes Fe-Z91DI and Fe-Z91PM along this work. After preliminary results from catalytic tests, the dry impregnation

method was used to prepare the catalysts with HZSM-5 of SiO₂/Al₂O₃ ratios of 52 and 371. These samples were denoted by the codes Fe-Z52DI and Fe-Z371DI.

For the preparation of Fe₃O₄ NPs, 501.6 mg of FeCl₂·4H₂O and 1262.8 mg of FeCl₃·6H₂O salts were added in a two-neck round-bottom flask and dissolved in 6.0 ml of deionized H₂O with 0.2 ml of HCl (37%). The mixture was attached to a condenser and set under stirring in an oil bath at 60°C. Then 16.0 ml of NaOH (1.5 M) was added to the solution dropwise with a syringe. The resultant black mixture was kept under stirring and heating for 1 h. Then, after cooling down, the particles were separated from the solution with a magnet and washed three times with 16 ml of deionized H₂O. The particles were dried in an oven at 60°C under an air atmosphere and ground in an agate mortar before use.

In all prepared catalysts, a Fe₃O₄/HZSM-5 weight ratio of 1 was used, as reported by Wei et al. (2017)¹²⁷, leading to a theoretical iron loading of 36% wt. For the dry impregnation catalyst, the as-prepared Fe₃O₄ NPs were dispersed in deionized H₂O (50 mg/ml). Then, a small amount of this suspension was added to the zeolite in a Petri plate until a slurry was obtained without excess liquid. The formed slurry was mixed with a metal spatula and dried in an oven at 60°C for 25 min. The procedure was repeated until all the suspension was used. After the final addition, the material was dried in oven overnight at the same temperature. The sample was collected and ground in an agate mortar. For the physical mixing catalyst, the as-prepared Fe₃O₄ NPs and the HZSM-5 support were mixed in an agate mortar until a homogenous powder was obtained. All catalysts were calcined at 550 °C for 4 h under air flow.

4.2 CATALYST CHARACTERIZATION

The catalyst characterizations and catalytic tests were carried out in Brazil, at the University of São Paulo.

4.2.1 Thermogravimetric Analysis (TGA)

A thermogravimetric analysis was carried out for the studied catalysts before and after the calcination step to evaluate their mass loss profile and weight loss. The curves were obtained from a Shimadzu DTG-60H thermobalance under a synthetic air flow of 100 ml/min, with a heating ramp of 30°C/min up to 1000°C.

4.2.2 Fourier Transform Infrared Spectroscopy (FTIR)

Infrared spectroscopy was performed to identify the support lattice bond vibrations. The analyzes were conducted on a Shimadzu spectrophotometer model IRPrestige-21 scanning the spectra in the range of 400-4000 cm^{-1} with 32 scans per analysis. The samples were analyzed using the Attenuated Total Reflectance (ATR) technique.

4.2.3 Raman Spectroscopy

To complement the structural characterization from FTIR, a Raman spectroscopy of the samples was carried out. The analyzes were conducted in a Renishaw InVia Raman Microscope equipped with argon laser with a power of 50 mW and wavelength $\lambda = 532$ nm. The spectra were taken in the range of 100-1200 cm^{-1} .

4.2.4 X-Ray Diffraction (XRD)

The crystalline phases of the samples were identified using X-ray diffraction in a Rigaku MiniFlex spectrometer with $\text{CuK}\alpha$ radiation. The measurements were made at 30kV and 10 mA in the range of 8–80° (2θ) Bragg angle using a 0.02 step width with a 0.5s counting time. The phases were identified based on the Inorganic Crystal Structure Database (ICSD) using Xpert Highscore software. The crystallite size of metal nanoparticles was determined by Scherrer's equation, shown in Eq.11.

$$D = \frac{\kappa \cdot \lambda}{\beta \cdot \cos\theta} \quad (11)$$

Where D is the mean size of the crystalline domain, κ is a dimensionless shape factor (value of 0.9), λ is the x-ray wavelength, β is the line broadening at half of the maximum intensity peak and θ is the Bragg angle.

4.2.5 Hydrogen Temperature Programmed Reduction (TPR)

Temperature programmed reduction of the samples was performed on a Autochem II 2920-Micromeritics equipment connected with a thermal conductivity detector (TCD). Before the analysis, the sample was pre-treated under Ar flow at 150°C for 30 min to eliminate the physisorbed water and other contaminants. After the pretreatment, the analysis was conducted

with an H₂/Ar (10 vol%) flow of 30 ml/min in the temperature range of 30–900 °C with a heating ramp of 10 °C/min.

4.2.6 Nitrogen sorption isotherms

To evaluate the surface area, porous size, and textural characteristics, nitrogen sorption isotherms were taken on Micromeritics ASAP-2020 equipment. Before the analysis, the samples were pre-treated under a vacuum at 120 °C for 12 h for degassing. After the pre-treatment, the measurements were taken at the N₂ boiling point (77 K).

4.2.7 Transmission Electron Microscopy (TEM)

To evaluate the morphology, shape, and metal dispersion of the catalysts, transmission electron microscopy was carried out. The analyzes were performed on a JEOL JEM 2100 microscope. The samples were prepared by dispersing the catalysts in ethanol, followed by their loading on a carbon-coated copper grid. The counting and editing image software ImageJ was used to estimate the particle size distribution.

4.2.8 CO, CO₂, and NH₃ Temperature Programmed desorption (TPD)

To assess the quantity and strength of acid and basic sites, as well as the CO adsorption capacity of the catalysts, temperature programmed desorption curves were taken using CO, CO₂, and NH₃ as probing molecules. The measurements were carried out in a Autochem II 2920-Micromeritics equipment connected with a thermal conductivity detector (TCD). The samples were outgassed and dried at 150°C under Ar flow of 30 mL min⁻¹ and cooled down to 30 °C. Then, the metallic samples were reduced at 450°C (10°C/min) under H₂/Ar (10% vol.) with a flow of 30 mL min⁻¹. The system was cooled down to 30 °C and then, the samples were treated with NH₃, CO₂ or CO (10-15 vol. %) at 30 mL min⁻¹ for 1 h. After adsorption of the probe molecule, the sample was purged with He. Finally, the desorption stage was conducted with increasing the temperature from 30 to 900 °C using a heating rate of 10 °C·min⁻¹.

4.2.9 Diffuse Reflectance Infrared Fourier Transform Spectroscopy (DRIFTS-*in situ*)

The Diffuse reflectance infrared Fourier transform spectroscopy (DRIFTS) was performed by using a spectrometer Shimadzu IRPrestige-21 equipped with a Mass spectrometer

analyzer. The catalyst was mixed with Al_2O_3 powder and set on the equipment window cell. Initially, the sample was reduced *in situ* under H_2 flow with a WHSV $4800\text{ml.g}^{-1}.\text{h}^{-1}$ at 450°C for 1 h. Then the system was cooled to 260°C and the pressure was raised to 8 bar with N_2 flow. The spectra were recorded with a resolution of 4 cm^{-1} between 4000 and 700 cm^{-1} wavenumbers for background correction. Then, the reduced catalyst was set to a continuous flow of $\text{CO}/\text{H}_2/\text{N}_2$ with a proportion of 3:6:1 with a WHSV of $4000\text{ ml.g}^{-1}.\text{h}^{-1}$. The spectra were recorded at several temperatures: 260, 280, 300 and 320°C .

4.3 FISCHER-TROPSCH PERFORMANCE ASSESSMENT

4.3.1 Catalytic Unit

The tests were carried out in an Microactivity Effi automated reaction system model MAE16110 PID Eng&Tech from Micromeritics[®], with controlling feed gas flow, temperature, and pressure, as shown in Figure 12. The system is equipped with a Hastelloy C fixed-bed tubular reactor model with an internal diameter of 9.1 mm and two condensers: a wax collector hot trap ($T \sim 170^\circ\text{C}$) and a liquid collector cold trap ($T \sim 20^\circ\text{C}$). The system features an electric furnace for heating the reactor, an internal heating box with a hot air convector, and an external heating line.



Figure 12 – Microactivity Effi automated reaction system for gas-to-liquid processes.

A chromatograph model GC-2010 Plus from Shimadzu[®] equipped with a thermal conductivity detector (TCD) and a flame ionization detector (FID) was used for quantification of reactants and products. A column model Carboxen-1010 PLOT from Supelco[®] was used for

separating light gases, further detected by TCD, while a column model Rtx-1 from Shimadzu® was used for separating the hydrocarbons, further detected by FID.

4.3.2 Methods for FTS catalyst testing

Initially, the reactor was prepared with a quartz wool bed and then loaded with catalyst powder. The mass used varied from 100 to 200 mg, depending on the WHSV used. For all catalytic tests, the catalyst was pre-reduced with pure H₂ gas flow at a WHSV of 4800 mL.g⁻¹.h⁻¹ at 450°C, following a heating ramp of 2 °C/min, and held at this temperature for 4 hours. Subsequently, the system was cooled down to the reaction temperature and switched to the reaction gases flow containing H₂:CO:N₂ with increasing pressure to 20bar. The system was kept for stabilization for 30 minutes. Then, FTS tests were conducted, evaluating different parameters, according to the following strategy:

1) Temperature screening activity: the tests were carried out by changing the temperature *in situ* following: 260°C → 300°C → 350°C → 300°C with the Fe-Z91PM and Fe-Z91DI catalysts. Conditions used: P = 20bar, H₂/CO=2, WHSV=6880 mL.g⁻¹.h⁻¹.

2) Support acidity evaluation: the tests were carried out with the Fe-Z52DI, Fe-Z91DI, and Fe-Z371DI catalysts. Conditions used: T=300 °C P=20bar, H₂/CO=2, WHSV=6880 mL.g⁻¹.h⁻¹.

3) Temperature evaluation: the tests were carried out with the Fe-Z91DI catalyst by changing the temperature from 260-320°C. Conditions used: P=20bar, H₂/CO=2, WHSV=6880 mL.g⁻¹.h⁻¹.

4) Space velocity evaluation: the tests were carried out with the Fe-Z91DI catalyst by changing the space velocity from 4000 to 9000 mL.g⁻¹.h⁻¹. Conditions used: T=300 °C P=20bar, H₂/CO=2.

5) Pressure evaluation: the tests were carried out with the Fe-Z91DI catalyst by changing the pressure from 1-30 bar. Conditions used: T=300°C, H₂/CO=2, WHSV=4000 and 6880 mL.g⁻¹.h⁻¹.

6) Feed composition evaluation: the tests were carried out with the Fe-Z91DI catalyst by changing the feed H₂/CO ratio from: 1-2. Conditions used: T=300°C, P=20 bar, WHSV=4000 mL.g⁻¹.h⁻¹.

7) Stability test: a time on stream test of 72 hours was carried out with the Fe-Z91DI catalyst for evaluating its stability. Conditions used: T=300 °C P=20bar, H₂/CO=2, WHSV=4000 mL.g⁻¹.h⁻¹.

The monitoring of reactants and lightweight products from the reactor was performed online every 30 minutes during the tests using gas chromatography. At the end of each test, the cold trap was bypassed, and all hydrocarbons were analyzed using gas chromatography. Triplicate data were collected for each studied condition, and the average value of the results was calculated. CO conversion and CO₂ selectivity calculations were performed based on the chromatographic areas/concentrations and are outlined in Appendix A. Hydrocarbon selectivity was calculated based on the weight percentage of each component obtained from chromatographic concentrations, with additional details provided in Appendix A.

4.4 FISCHER-TROPSCH KINETIC ASSESSMENT

4.4.1 Mass transfer effects evaluation

Prior to collecting data for the estimation of kinetic parameters, the effect of mass transfer on the studied system was evaluated. Catalytic tests were conducted with varying W/F_{syg} (catalyst mass/syngas flow) ratio values by changing either the catalyst mass or the syngas flow. These tests followed the methods described in the previous section, with WHSV values evaluated at 4000, 9000, 20000, 40000, 80000, 120000, and 160000 mL.g⁻¹.h⁻¹. Subsequently, based on the W/F_{syg} vs X_{CO} curve, the Weisz-Prater and Mears criteria were calculated to measure the influence of mass transfer on the reactor. The Weisz-Prater criterion determines if internal diffusion is limiting the reaction using the expression given in Eq. 12:

$$C_{WP} = \frac{\text{Actual reaction rate}}{\text{A diffusion rate}} = \eta \Phi^2 = \frac{-r_a' \rho_c r^2}{D_{eff} C_{as}} \quad (12)$$

In which, $-r_a'$ is the observed reaction rate, ρ_c is catalyst specific mass, r is particle radius, D_{eff} is the effective diffusion coefficient, and C_{as} is the reactant concentration on the catalyst surface. If $C_{WP} \ll 1$, there are no internal diffusion limitations and consequently no concentration gradient exists within the particle. However, if $C_{WP} \gg 1$ internal diffusion limits the reaction.¹²⁸

The Mears criterion (Eq. 13) is used to determine whether the external mass transfer from the bulk gas phase to the surface of the catalyst can be neglected.

$$MR = \frac{-r_{co'} \rho_c (1-\phi) R n}{k_c C_{ab}} \quad (13)$$

In which, ϕ is the bed porosity, k_c is mass transfer coefficient, R is the catalyst particle radius, C_{ab} is the bulk reactant concentration, and n is the reaction order. If Mears criterion value $MR < 0.15$, then external mass transfer effects can be ignored, and there is no difference in concentration between the bulk gas and the catalyst surface.¹²⁸

4.4.2 Kinetic data acquisition and parameters estimation

The models investigated in this study followed the Langmuir-Hinshelwood-Hougen-Watson (LHHW) kinetics approach, and the kinetic and equilibrium constants followed the Arrhenius's Law. Based on the literature review, 10 LHHW models were selected for studying the Fe-Z91DI catalyst. For most of the models considered, the reaction rate can be expressed as: $-r_{co}' = f(T, pH_2, pCO, pCO_2, pH_2O)$.

The tests for kinetic data acquisition were conducted at WHSV of 160000 mL.g⁻¹.h⁻¹ and pressure of 20 bar. The catalysts were also reduced under pure H₂ gas flow with a WHSV of 4800 mL.g⁻¹.h⁻¹ at 450°C, for 4 hours. During the reaction, the variables studied included temperature and the H₂/CO feed ratio in order to obtain a collection of data for model adjustment. The tests were performed at temperatures of 260, 280, 300, 310 °C and H₂/CO feed ratios of 1.0, 1.5, 2.0 and 3.0. Triplicates for each studied condition were used.

After evaluating the mass transfer conditions, the assumption of a differential reactor was considered, which posits that the reaction rate is constant at all points within the reactor. Consequently, the CO consumption rate was calculated as given by Eq. 14.

$$-r_{CO}' = \frac{F_{CO}^{inlet} X_{CO}}{W_{cat}} \quad (14)$$

In which, F_{CO}^{inlet} is the CO molar inlet flow, X_{CO} is the CO conversion and W_{cat} is the catalyst mass. The details of all data calculations are shown in Appendix B.

The observed experimental reaction rates were adjusted to the theoretical rates predicted by the selected models. To achieve this, a nonlinear regression analysis was performed using the Levenberg-Marquardt algorithm implemented in Python 3 programming language. This analysis was complemented by the calculation of statistical parameters, including the coefficient of determination, Root Mean Square Error (RMSE), and Fisher Snedecor test (F Value), in order to assure the fit quality, prediction accuracy and overall significance.

5 RESULTS AND DISCUSSION

This section is organized into four main topics. The first and third topics present the catalyst characterization before and after reaction, respectively. The second topic presents the results and discussion of the Fischer-Tropsch synthesis reaction tests. Finally, the fourth topic presents the kinetic assessment and a critical discussion based on the existing literature.

5.1 CATALYSTS CHARACTERIZATION

5.1.1 Thermogravimetric analysis (TGA)

A thermogravimetric analysis of the Fe-Z91PM and Fe-Z91DI samples were performed before and after the calcination step, as shown in Figure 13 and Figure 14.

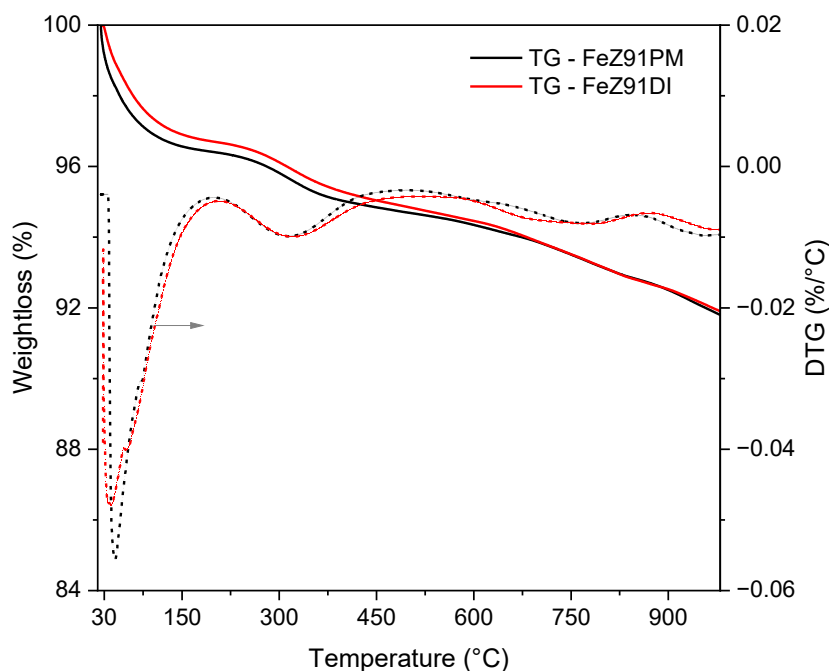


Figure 13 - TGA curves of the Fe-Z91PM and Fe-Z91DI as-synthesized catalysts

The results in Figure 13 show the thermogravimetric profiles of samples prepared by physical mixing and dry impregnation. The total mass loss for the synthesized material is approximately 8.4%. It is observed that there are two distinct regions of mass loss rates on the

synthesized samples. The first region, up to 100°C, indicates the mass loss of water before and after the calcination step.

The second region, between 220-420°C, is attributed to the mass loss of residuals from either the metal particles synthesis or the reminiscent zeolite template under the oxidative atmosphere. Based on the TGA profiles, a calcination temperature of 550°C was selected.

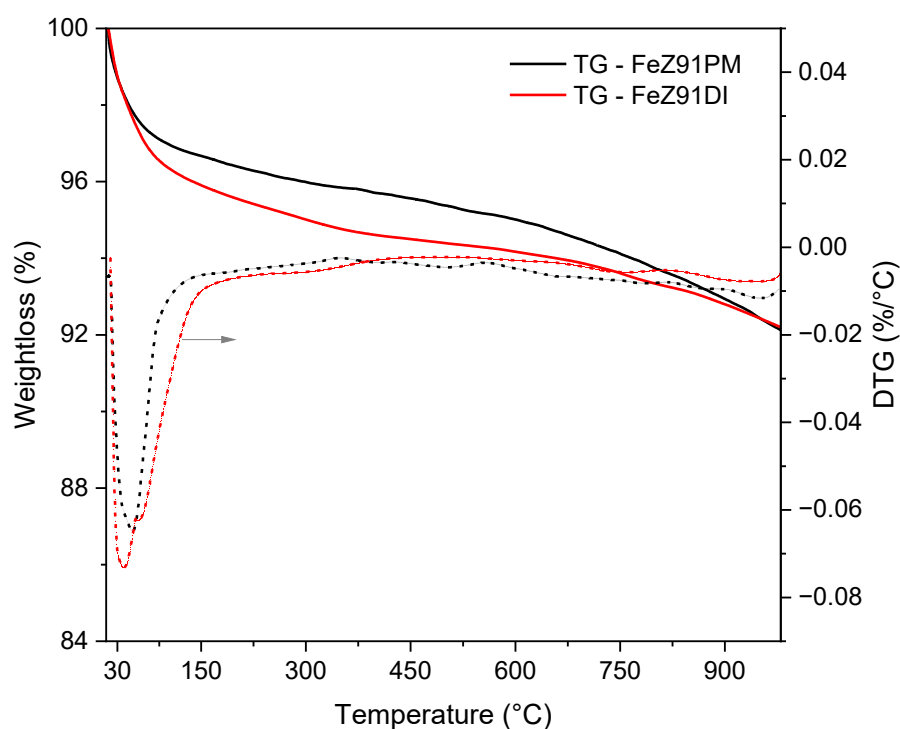


Figure 14 - TGA curves of the Fe-Z91PM and Fe-Z91DI calcined catalysts.

After the calcination, the DTG curves exhibited only the peak around 40-60°C, which is related to the mass loss of water, as presented in Figure 14. This mass loss profile was similar to those reported previously for this type of material.^{129,130} The TGA curves for the Fe-Z52DI and Fe-Z371DI samples after calcination were obtained and are presented in Appendix C. The catalysts prepared with different zeolites showed similar mass loss profiles.

5.1.2 Fourier Transform Infrared Spectroscopy (FTIR)

All catalysts were analyzed by FTIR after calcination for identifying zeolite lattice binding vibrations and the results are shown in Figure 15 and Figure 16.

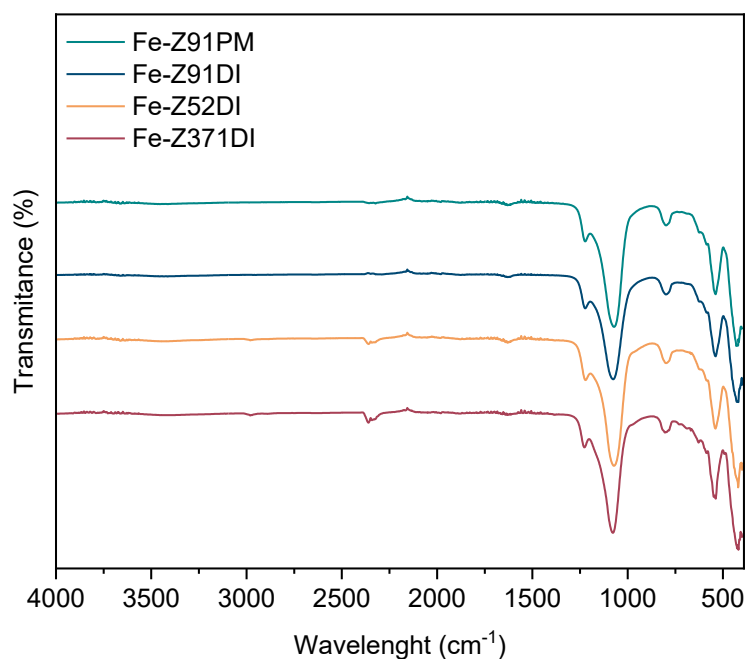


Figure 15 - FT-IR Spectra of the Fe-Z91PM, Fe-Z(52, 91, 371)DI catalysts.

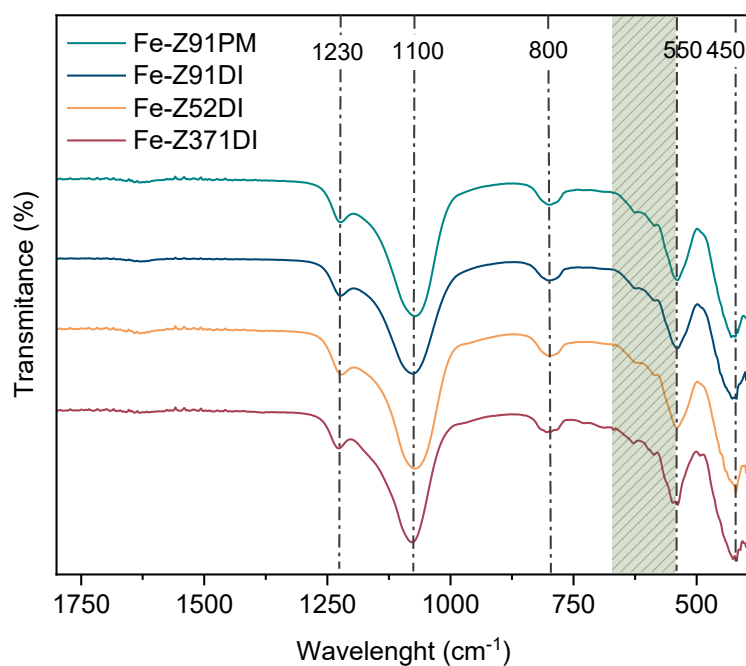


Figure 16 - FT-IR Spectra of the Fe-Z91PM and Fe-Z(52, 91, 371)DI catalysts

Generally, the characteristic bands of aluminosilicate materials appear between 400 cm^{-1} and 1300 cm^{-1} and correspond to vibrations of the tetrahedral framework.^{131,132} The results displayed in Figure 16 showed similar spectra in this region, indicating that the Fe deposition on the support with different $\text{SiO}_2/\text{Al}_2\text{O}_3$ ratios did not change the main zeolite structures.

The band observed around 550 cm^{-1} indicates the vibration of external double 5-membered ring blocks, which is characteristic of the HZSM-5 structure formed by channels of 4, 5 and 6 members, as shown in Figure 17. The band around 1230 cm^{-1} is assigned to the external asymmetric stretching of structures containing four chains of 5-membered ring blocks, which is also characteristic of HZSM-5. The band near 800 cm^{-1} is assigned to external symmetric stretching of Si-O-Si or Si-O-Al linkages of zeolites, while the bands around 450 cm^{-1} and 1100 cm^{-1} indicate internal vibrations of Si(Al)O₄ tetrahedrons from the lattice.^{131,132}

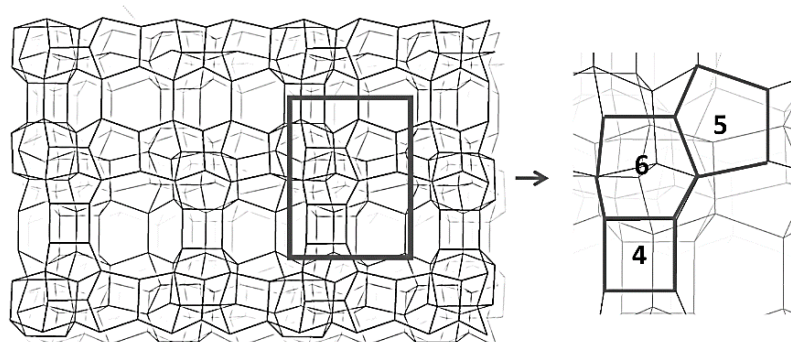


Figure 17 - HZSM-5 network structure.

Source: Adapted from Database of Zeolite Structures (2022)¹³³

Finally, the characteristic bands corresponding to stretching vibration modes of the Fe-O bond appear in the ranges $550\text{-}700\text{ cm}^{-1}$, as highlighted in the spectra, and $1000\text{-}1400\text{ cm}^{-1}$ according to the literature.^{134,135} The spectrum observed in Figure 16 indicates the absorption band in a small region near the 550 cm^{-1} . However, as the iron oxide particles are dispersed in zeolite, Fe-O bands are difficult to identify compared to the support, which present higher intensity bands.

5.1.3 Raman Spectroscopy

RAMAN Spectroscopy was performed for identifying precisely the Fe-O bonds and the results are shown in Figure 18.

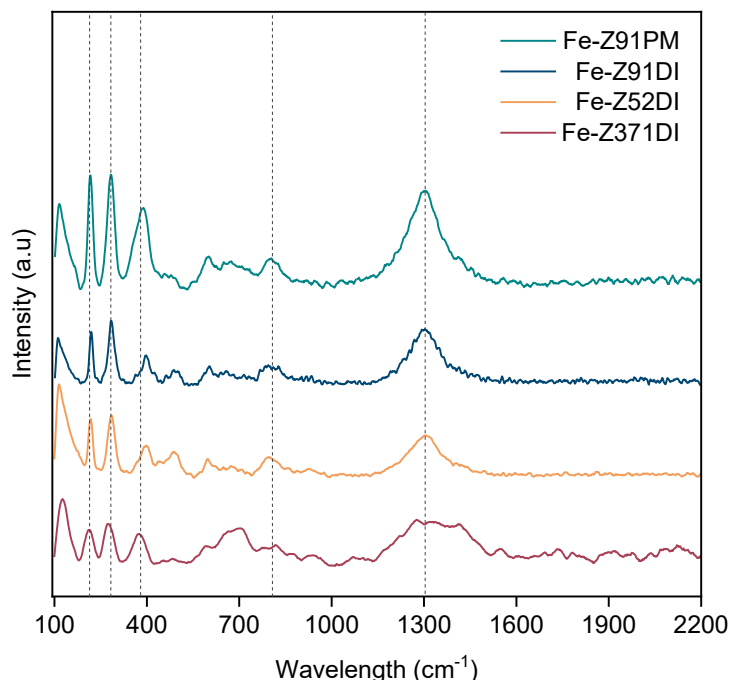


Figure 18 - RAMAN Spectra of the Fe-Z91PM and Fe-Z(52, 91, 371) DI catalysts

The spectra presented characteristic bands of the HZSM-5 and Fe_2O_3 structures. The band at 380 cm^{-1} corresponds to the vibration of double 5-membered ring blocks, while the band at 800 cm^{-1} is attributed to stretching symmetrical vibrations of HZSM-5 lattice^{136,137}. On the other hand, signals around 294 cm^{-1} and 440 cm^{-1} , which are attributed to the bonds of the HZSM-5 rings with six and four members, respectively, did not show significant intensity. The decrease of the zeolite lattice bands after doping with Fe was also observed by Sun et al. (2008)^[138]. This behavior may be observed by Raman scattering properties, since it is a surface-sensitive technique, and the presence of iron species may cause partial masking in the zeolite vibration signals.¹³⁸

Regarding the metallic phase, one observes the presence of Fe_2O_3 bands instead of Fe_3O_4 , which suggests that a phase transformation of the metal oxide may have occurred.¹³⁹ This was expected since the samples were calcined in air atmosphere, leading to the oxidation of magnetite to hematite, confirmed later by XRD and TPR analyses.

Hematite has a crystal structure with Fe atoms disposed in pairs of $\text{Fe}(\text{O})_6$ octahedra species, with 3 short and 3 long nearest-neighbor Fe–O distances, as shown in Figure 19.¹⁴⁰ The phonons generated in its structure by the light irradiation are classified as internal mode, representing the motion of $\text{Fe}(\text{O})_6$ species, or as external mode, attributed to rotation and translation of the entire Fe_2O_3 structure.¹⁴¹

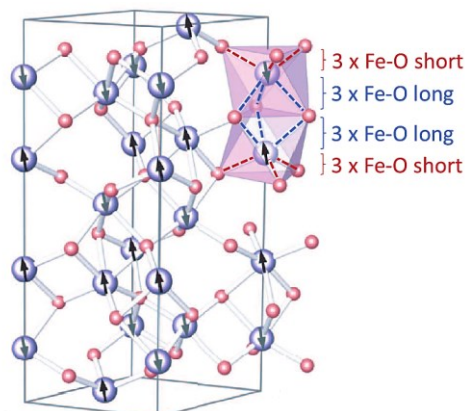


Figure 19 - Crystal structure of hematite.

Source: Reproduced from Sanson, Mathon and Pascarelli (2014)¹⁴⁰ with permission from Elsevier.

The RAMAN spectra presented in Figure 18 showed bands at around 218 cm^{-1} and 285 cm^{-1} , which are representative of internal and external phonons vibration modes, respectively.¹⁴¹ In addition, the large band observed at 1320 cm^{-1} is also typical of Fe_2O_3 structure and represents a two-phonon scattering mechanism.^{141,142}

In summary, the results from RAMAN spectroscopy complemented the FTIR results. The infrared spectroscopy was better for identifying the Al-O and Si-O binding vibrations from the support phase, while the RAMAN spectroscopy showed the bands corresponding to the Fe-O binding vibrations of the metallic phase.

5.1.4 X-ray diffraction (XRD)

The catalysts were analyzed by XRD after calcination to identify the crystalline phases of both metal and support materials. The results in the $2\theta = 5\text{-}75^\circ$ range are shown in Figure 20.

The peaks observed at 2θ around 7.9 , 8.8 , 23.0 , and 24.1° for all samples are consistent with HZSM-5 crystalline structure according to the Inorganic Crystal Structure Database (ICSD) standard n° 201183. The peaks between $2\theta = 7\text{-}10^\circ$ correspond to zeolite lattice planes with Miller indices of (011) and (200), while the peaks between $2\theta = 23\text{-}25^\circ$ are related to the planes (051) and (520)¹⁴³. This indicates stable structure of the support after iron loading and thermal treatment. The intensity of peaks in the lower range ($7\text{-}10^\circ$) is supposed to decrease when the iron is loaded on the zeolite, since the Fe NPs may have an interaction with the support and/or be incorporated in the zeolite channels.^{144,145}

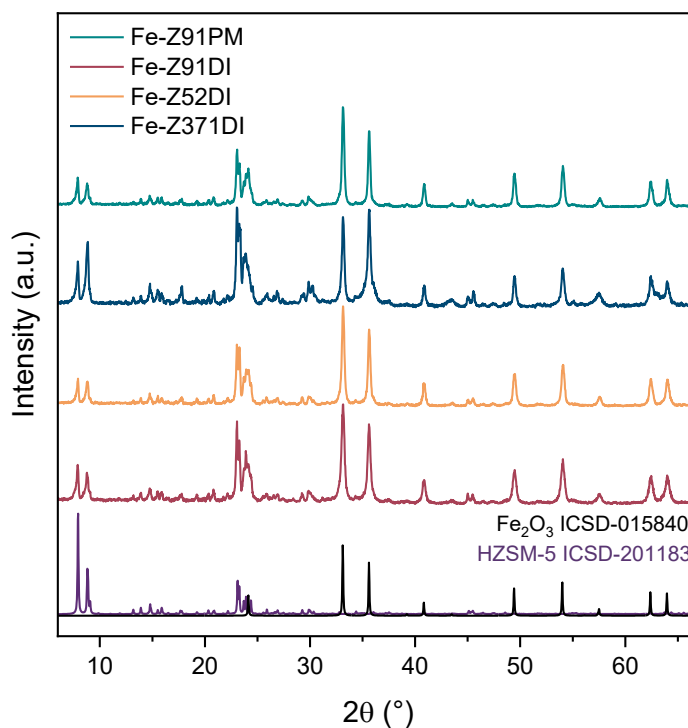


Figure 20 - XRD diffractogram of the Fe-Z91PM and Fe-Z(52, 91, 371) DI catalysts

The peaks observed at 2θ around 24.1, 33.0, 35.5, 40.8, 49.3, 53.9, 57.5, 62.3, and 64.0 ° are in accordance with the Fe₂O₃ pattern from ICSD standard n° 015840. These results corroborate with the RAMAN analysis, indicating that the magnetite NPs obtained after the synthesis were oxidized to hematite during the calcination step. Additionally, no impurities were detected in the diffractogram, indicating high purity and crystallinity for the synthesized samples.

The crystallite size of iron oxide was estimated using the Scherrer equation for the most intense peak, and further estimated from TEM images. The results, displayed in Table 4, indicated a smaller crystallite size of Fe NPs for the catalyst prepared by the impregnation method compared to the method of physical mixture.

Table 4 - XRD parameters and crystallite size of catalysts

Catalyst	Position peak 2θ (°)	FWHM (°)	Crystallite size from Scherrer equation (nm)	Average particle size from TEM analysis (nm)
Fe-Z91PM	33.14	0.29	27.74	30.40
Fe-Z91DI	33.13	0.39	21.01	22.90
Fe-Z52DI	33.14	0.31	25.71	-
Fe-Z371DI	33.14	0.32	25.29	-

5.1.5 N₂ adsorption isotherms

The N₂ physisorption analysis was taken for evaluating the textural properties of the Fe-Z91PM and Fe-Z91DI catalysts. The resultants isotherms and textural properties are displayed in Figure 21 and Table 5, respectively.

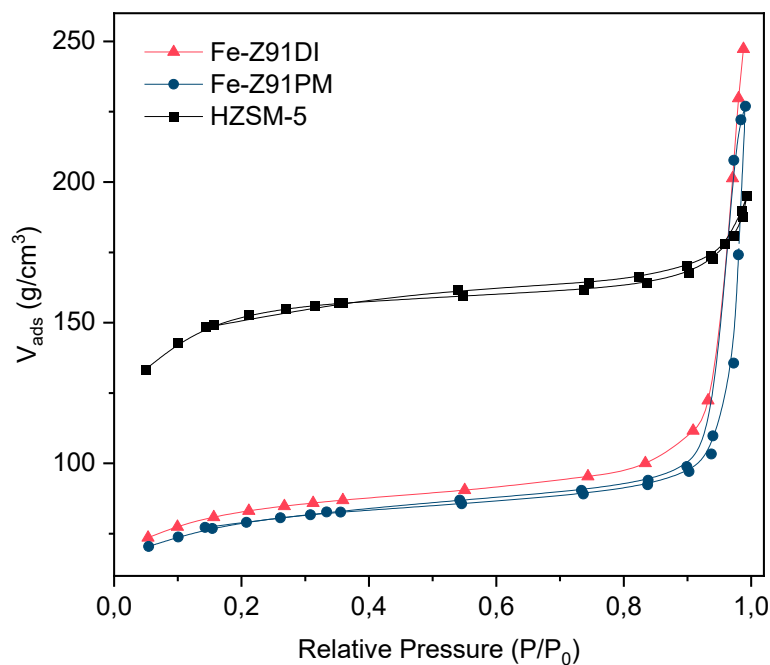


Figure 21 - N₂ adsorption/desorption isotherms of Fe-Z91DI and Fe-Z91PM catalysts calcined and HZSM-5.

Table 5 - Textural properties of the catalysts.

Catalyst code	S _{BET} (m ² /g) ^a	S _{micro} (m ² /g) ^b	V _{micro} (cm ³ /g) ^b	d _{pore range} (nm) ^c	d _{pore} (nm) ^c	NPs	Reference
						diameter (nm)	
H-ZSM-5	463.3	296.7	0.16	1.8 - 132.5	4.5	-	This work
Fe-Z91PM	244.2	145.8	0.07	1.8 – 121.1	16.8	30.40	This work
Fe-Z91DI	255.3	154.3	0.08	1.7 – 114.6	16.3	22.90	This work
Fe/ZSM-5	235.0	181.0	0.10	-	-	37.8	146
Fe/ZSM-5	345.0	166.0	0.12	-	-	19.6	147
Fe/Z240	370.0	313.0	0.14	-	-	-	113

^a Brunauer-Emmett-Teller (BET) surface area.

^b t-Plot method.

^c Barrett-Joyner-Halenda (BJH) pore distribution.

The impregnated catalysts exhibited similar microporous adsorption-desorption isotherms of type II, with hysteresis loops of type IV at high relative pressure, based on the IUPAC classification. This behavior is typical of Fe/HZSM-5 materials and indicates the formation of a monolayer at low relative pressure, while multilayer adsorption occurs at high relative pressures.⁸⁹ The observed hysteresis of type IV suggests the influence of capillary condensation on the porous structures of the support. According to Senamart et al. (2016)¹³², these results are commonly observed in agglomerated iron-containing zeolites that possess both micropores and slit-shaped mesopores.

One can also observe the high surface area and small pore diameter of pure H-ZSM-5 in comparison to the impregnated catalysts. The zeolite surface area decreased by almost half of its initial value when iron was loaded, while the average pore diameter increased from 4 nm to 16 nm. The change in values is a result of the iron allocation on the zeolite channels structure.¹⁴⁸

The isotherms and surface areas were similar for Fe-Z91DI and Fe-Z91PM catalysts, indicating that the different methods of iron loading led to catalysts with similar structures. Nevertheless, the catalyst prepared by impregnation showed a slightly larger surface area and pore volume, compared to those prepared by physical mixing. This is partly due to the smaller particle size observed for this catalyst, which less obstructs the support surface¹⁴⁸. In any case,

the textural properties observed are comparable with similar catalysts previously prepared, as shown in Table 5.

5.1.6 Temperature programmed reduction (TPR)

H₂-TPR analysis was performed for determining the reduction of the metal oxide of the catalysts. The reduction profiles of all samples are shown in Figure 22 and the deconvolution curves for the Fe-Z91DI reduction profile is presented in Figure 23.

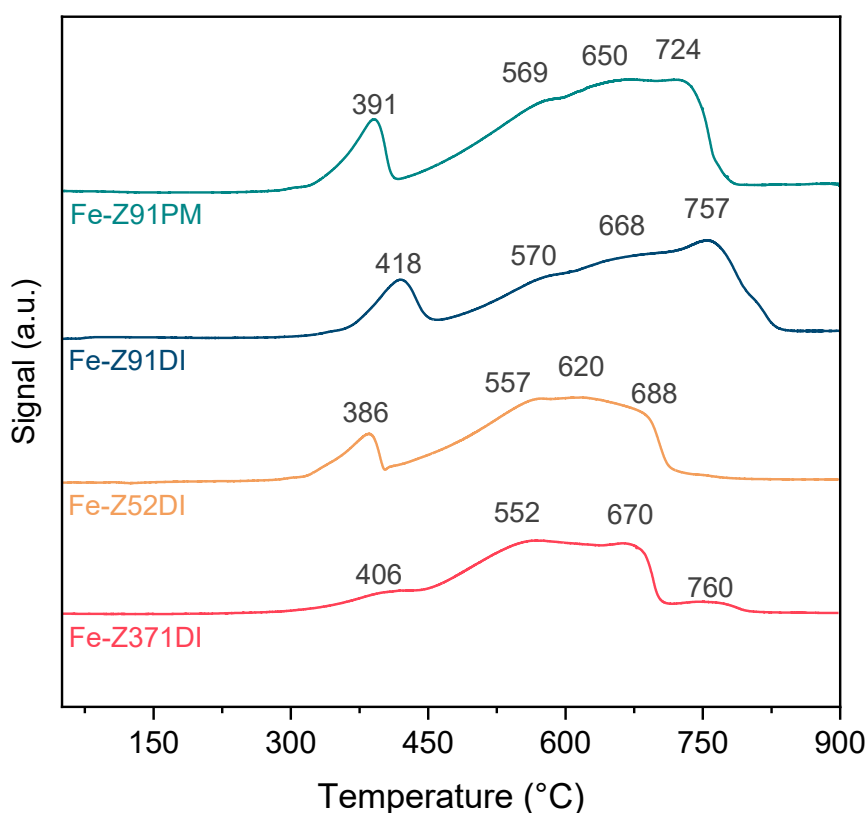
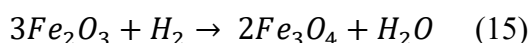


Figure 22 - H₂-TPR curves of the Fe-Z91PM and Fe-Z(52, 91, 371)DI catalysts

The results presented in Figure 22 showed two distinct reduction steps in temperatures between 300 °C and 750 °C for all catalysts. The first peak in the range 300-450 °C represents the reduction of the hematite species to magnetite, as shown in Eq. 15, in accordance with previous results reported in literature.^{146,149}



This reduction step is well known for hematite NPs and was already expected since XRD spectra showed the presence of Fe₂O₃ instead of Fe₃O₄. The slight difference observed in

the temperature for this step may be attributed to the heterogenous dispersion of metallic NPs on the support and their interaction with the HZSM-5 surface.

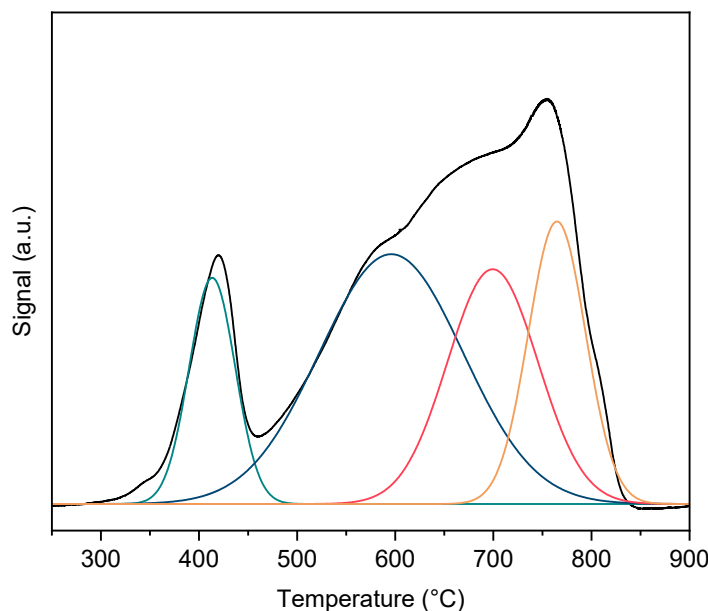
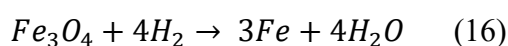


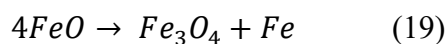
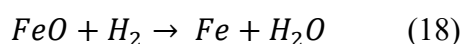
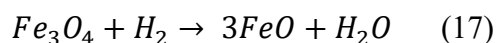
Figure 23 - H₂-TPR detailed profile of the Fe-Z91DI catalyst.

According to Chen et al. (1995)¹⁵⁰, it is reasonable to consider that supported Fe³⁺ species might exist in the catalyst in different oxide states, such as large or bulk α -Fe₂O₃ phase, small α -Fe₂O₃ particles and surface species resulting from the interaction of iron with the support. The variation in the particle sizes was actually observed in the TEM results (section 5.1.7). This explains the lower temperature reduction observed for the Fe-Z91PM sample compared to the Fe-Z91DI. In general, the interaction of the metallic phase with support depends on the preparation method, which influences the metal oxide dispersion¹⁵¹. Thus, it seems that the physical mixture led to a lower interaction of the Fe₂O₃ NPs with the HZSM-5 compared to the impregnation method.

The second broad peak of reduction between 450°C and 750°C corresponds to the transformation of Fe₃O₄ into metallic Fe⁰ (Eq.16), as reported in the literature.^{152,153} However, intermediate transformations have been reported to occur at this temperature range.^{154,155} Figure 23 shows the deconvolution curves for the broad peak reduction of the Fe-Z91DI catalyst.



Above 450 °C, reduction of Fe₃O₄ to FeO was observed, as shown in Eq.17, followed by the reduction of FeO to Fe⁰, as shown in Eq.18. At the same time, FeO is metastable at temperatures below 600°C and can disproportionate into Fe and Fe₃O₄ species, as shown in Eq.19. Thus, the coexistence of Fe⁰, Fe₃O₄ and FeO compounds in the sample explains the multiple peaks observed in this final stage of reduction according to Stoicescu et al. (2022)¹⁵⁵. It should also be mentioned that the intermediate transformation steps are observed when a high heating rate is used during the TPR analysis, which explains the results obtained in this study.¹⁵⁵



5.1.7 Transmission Electron Microscopy (TEM)

A Transmission electron microscopy analysis was carried out for the Fe-Z91DI and Fe-Z91PM catalysts for visualizing the NPs size and their dispersion on the support. Figure 24 and Figure 25 show the images and particle size distribution for the Fe-Z91DI sample, and Figure 26 and Figure 27 the results for the Fe-Z91PM sample.

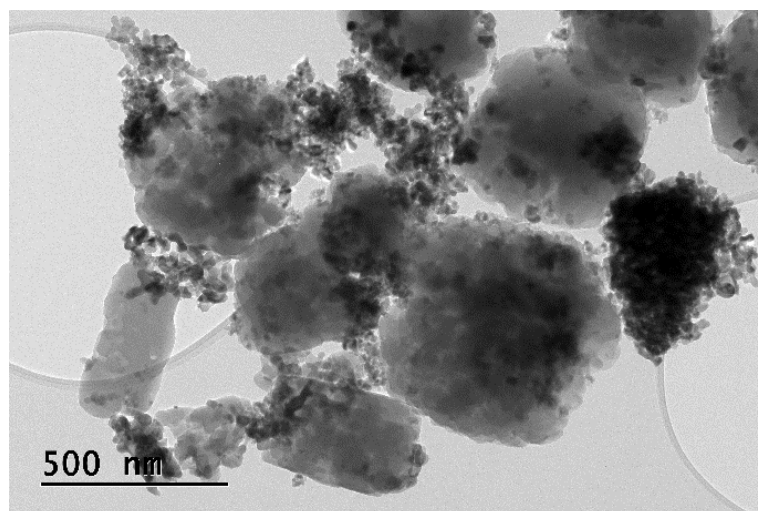


Figure 24 – TEM image of Fe-Z91DI catalyst with a resolution of 500 nm.

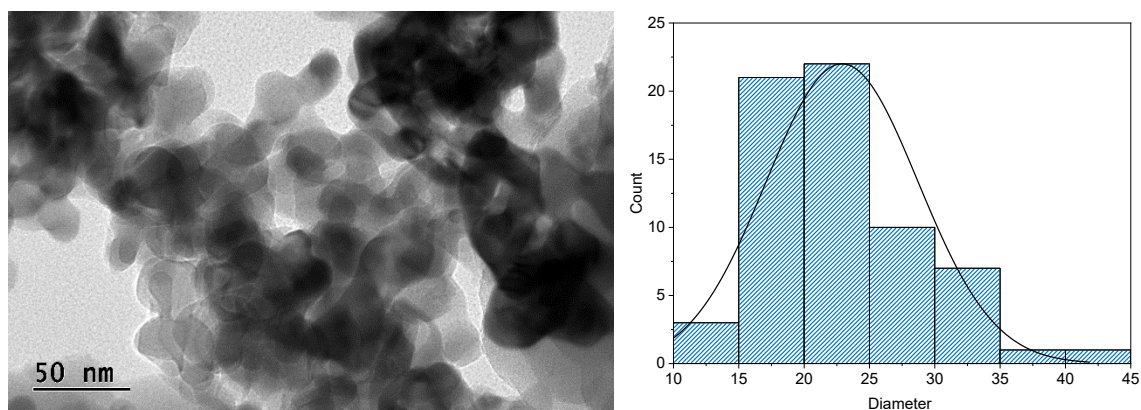


Figure 25 - TEM image of Fe-Z91DI catalyst with a resolution of 50 nm

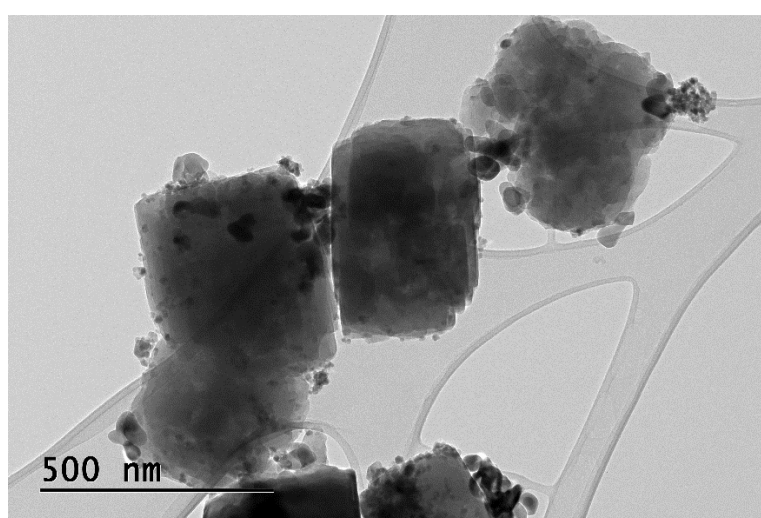


Figure 26 - TEM image of Fe-Z91PM catalyst with a resolution of 500 nm.

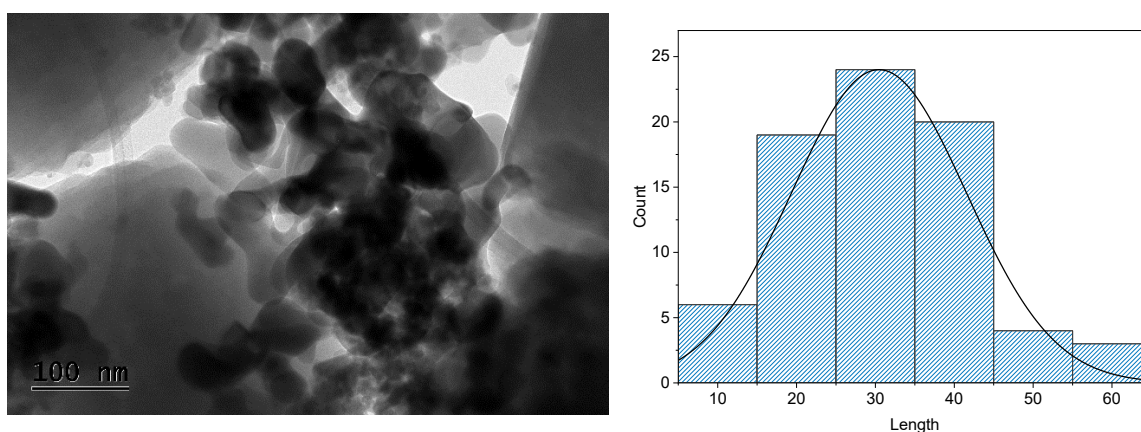


Figure 27 - TEM image of Fe-Z91PM catalyst with a resolution of 100 nm

The iron oxide NPs were easily identified in the samples by the black dots and agglomerates, observed in Figure 24 and Figure 26, whereas large gray crystals represent the

zeolite. These results were confirmed by the surface elemental analysis from energy dispersive spectroscopy (EDS), shown in Figure 28.

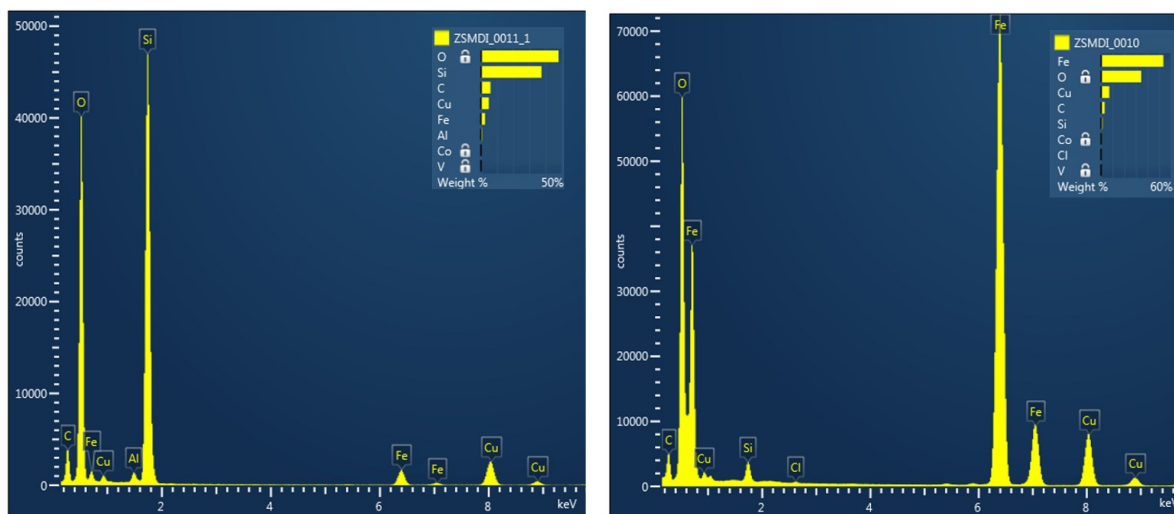


Figure 28 - EDS analysis of the Fe-Z91DI catalyst.

For both catalysts, the metal nanoparticles were heterogeneously distributed on the support. The images show the presence of small and medium metal particles dispersed and also regions with agglomerates or clusters, leading to larger particles. The Fe-Z91PM catalyst exhibited a wider particle size distribution of 5-60 nm and an average particle size of about 30.4 nm compared to the Fe-Z91DI catalyst, which exhibited a particle size distribution between 5 and 45 nm and an average particle size of about 22.9 nm. These results are in good agreement with those reported in the literature for a similar catalyst.^{147,156} Xu et al. (2020)¹⁴⁶ also observed that Fe NPs exhibited a wide particle size distribution of 25~70 nm when impregnated in HZSM-5, without the addition of a promoter.

The difference in the average particle sizes indicates the influence of different preparation methods on the metal dispersion and distribution over the support. In fact, it is known that the impregnation method leads to insertion of metal suspension into the pores of the zeolite, due to a capillary pressure difference¹⁵⁷. This may explain the smaller size observed for the particles in the Fe-Z91DI catalyst compared to Fe-Z91PM.

5.1.8 Temperature programmed desorption (TPD)

Temperature Programmed Desorption (TPD) analyses of CO₂, NH₃ and CO were conducted to evaluate catalyst surface properties, including its acid and basic sites, and the dispersion of metal particles. The detailed results are presented in the following sections.

5.1.8.1 CO₂ and NH₃ temperature programmed desorption (TPD)

The desorption of CO₂ is employed to assess the presence of basic sites on the material. These sites can originate from surface hydroxyl groups, metal-oxygen pairing of Lewis acid and basic components, or the presence of surface oxygen ions with low coordination number.¹⁵⁸ However, with CO₂-TPD it is only possible to determine the strength and quantity of basic sites, but not differentiate the type of basic sites, which is possible with pyridine FTIR technique. Usually, CO₂ desorbs at lower temperatures from weak alkaline sites and at higher temperatures from strong alkaline sites.

Figure 29 and Figure 30 present the overall desorption profile of CO₂ and NH₃ respectively, and Table 6 presents the detailed results of adsorption of both molecules. The detailed desorption curve for each sample is presented in Appendix A. The results showed that pure zeolites exhibited different CO₂ desorption profiles based on distinct SiO₂/Al₂O₃ ratios. The zeolite with higher nominal Al content (SiO₂/Al₂O₃ = 52) exhibited mostly weak basic sites, whereas zeolites with lower Al content (SiO₂/Al₂O₃ = 91 and 371) exhibited weak, moderate, and strong basic sites. These different adsorption site strengths related to nominal Al content were expected, since the zeolite acidity/basicity is inherently related to the presence of aluminum in the framework.

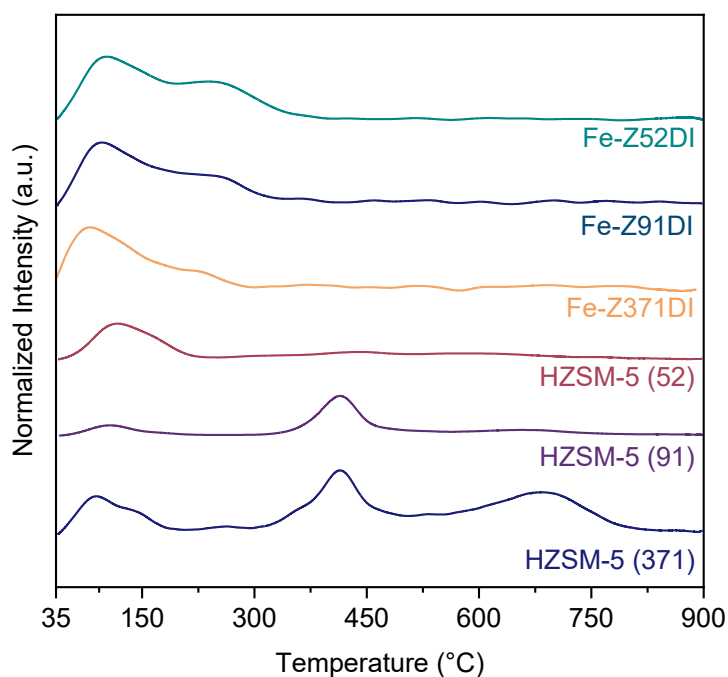


Figure 29 - CO₂-TPD profiles of pure HZSM-5 and impregnated catalysts.

Impregnating zeolites with iron led to a reduction in total CO₂ adsorption, indicating that iron oxide particles masked/blocked a fraction of the zeolite basic sites, as expected. The desorption profile for iron-impregnated samples also changed compared to pure zeolites. From Table 6 and Figure 29, impregnated samples lacked peaks corresponding to moderate sites (410-450°C) and exhibited a shift toward lower temperatures (170-230 °C), indicative of weak sites during desorption. This indicates the influence of iron impregnation on altering the strength of zeolite basic sites.

This behavior was also observed by Liu et al. (2023)¹⁵⁸ who studied CO₂ adsorption/desorption on H-ZSM5 impregnated with Ni. The study showed that the addition of metallic Ni weakened the basic strength of adsorption sites, leading to the transformation of strongly basic sites into moderate or weakly basic sites.

Table 6 - NH₃ and CO₂ adsorption results from TPD analysis.

Sample	T ₁ (°C)	Ads.	T ₂ (°C)	Ads.	T ₃ (°C)	Ads.	Total ads. molecule (mmol/g)
		molecule (mmol/g)		molecule (mmol/g)		molecule (mmol/g)	
		NH ₃			NH ₃	NH ₃	Total NH ₃
Fe-Z52(DI)	97	0.19	199	0.43	-	-	0.62
Fe-Z91(DI)	105	0.72	234	1.51	615	0.46	2.7
Fe-Z371(DI)	91	0.35	167	0.38	-	-	0.73
HZSM-5 (52)	101	5.3	391	1.1	561	0.60	7.0
HZSM-5 (91)	96	5.3	413	5.2	661	1.2	11.7
HZSM-5 (371)	89	1.2	413	0.86	669	1.0	3.1
		CO ₂			CO ₂	CO ₂	Total CO ₂
Fe-Z52(DI)	106	0.21	224	0.22	-	-	0.43
Fe-Z91(DI)	101	0.08	198	0.16	-	-	0.24
Fe-Z371(DI)	89	0.03	170	0.04	-	-	0.07
HZSM-5 (52)	117	0.55	446	0.40	-	-	0.96
HZSM-5 (91)	109	0.08	413	0.42	663	0.13	0.64
HZSM-5 (371)	89	0.07	420	0.17	684	0.17	0.42

The NH₃-TPD analysis of pure zeolites revealed three desorption peaks at 89-101 °C, 390-415 °C, and 560-670 °C, corresponding to weak, moderate, and strong acid sites, respectively. All pure zeolites exhibited weak acid sites, but those with higher nominal Al content demonstrated stronger and increased NH₃ adsorption at this phase, as detailed in Table 5. However, for moderate (391 - 413 °C) and strong acid sites (561 – 669°C), HZSM-5 (91) presented a greater interaction with NH₃ compared to HZSM-5 (52) and HZSM-5 (371). The total amount of adsorbed NH₃ was notably higher for HZSM-5 (91), indicating a greater number of acid sites compared to the other two materials. This result may be due to differences in the accessibility of Al sites within the zeolite framework.¹⁵⁹

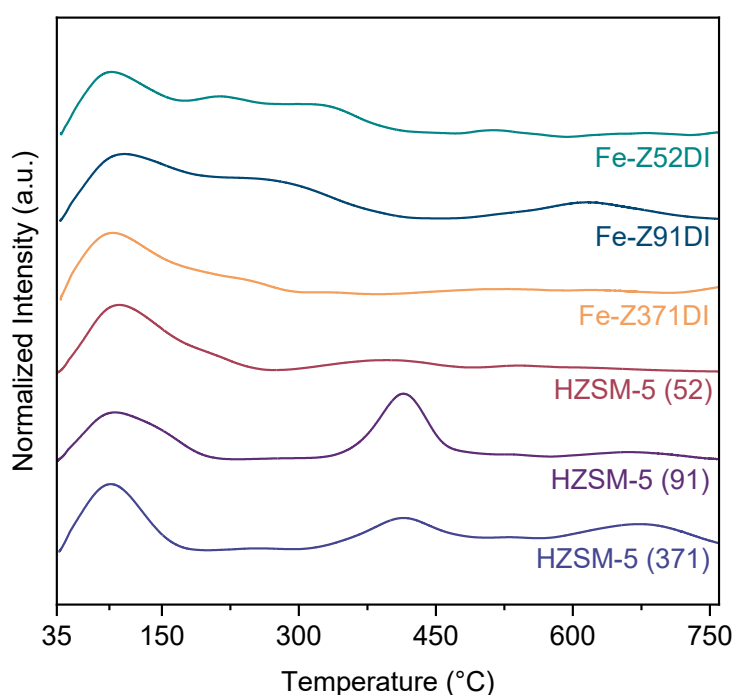


Figure 30 - NH₃-TPD profiles of pure HZSM-5 and impregnated catalysts.

The same pattern was observed for the impregnated catalysts, with Fe-Z91DI exhibiting the higher amount of acid sites among the catalysts evaluated. It is noteworthy that the total amount of adsorbed NH₃ decreased with iron impregnation, as observed in the CO₂ adsorption analysis, indicating the masking effect of metal particles on acid sites. This observation agrees with the study conducted by Xu et al. (2018)¹⁶⁰, who investigated the loading of H-ZSM5 with Fe particles and reported the reduction in the number of acid sites with increasing iron content in the zeolite.

The strength of acid sites also changed with the iron loading on the support. One can observe a shift in the temperature of the moderate acid sites from ~400°C to ~200°C, indicating a weakening of the site adsorption. This finding aligns with the results in the literature.¹⁶¹

Doping HZSM-5 with Fe particles had minimal impact on the temperature of weak acid sites, but it did modulate the moderate acidity to adjacent weaker positions, as observed.¹⁶¹

5.1.8.2 CO Temperature programmed desorption (TPD)

The adsorption/desorption behavior of carbon monoxide with the catalyst surface is of extreme importance for the Fischer-Tropsch synthesis, since the CO activation on the catalyst sites is the first step of the reaction mechanism. Figure 31 presents the desorption profiles for the impregnated catalysts.

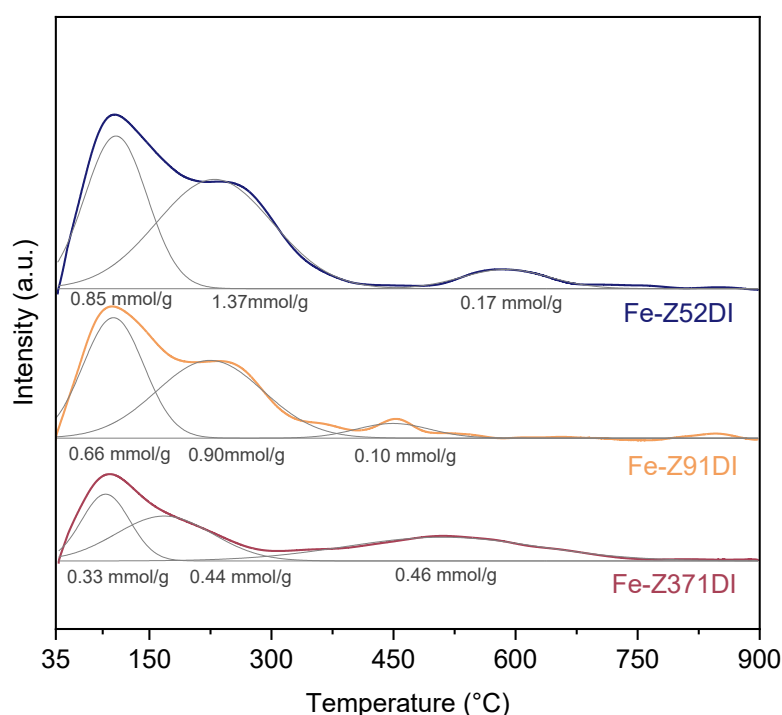


Figure 31 - CO - TPD profiles of impregnated catalysts.

The results exhibited weak and moderate interactions of CO with the studied catalysts, indicating their capability to bind with CO molecules over a broad temperature range. Important variables to observe in CO-TPD analysis are the adsorption strength, correlated to temperature, and number of active sites, associated with the quantity of adsorbed molecule. According to Liu et al. (2021)¹¹⁷, in Metal/Zeolite systems, it is important to note that CO adsorption cannot be attributed only to the influence of iron phases, but also to properties of the support material, which play a substantial role in this phenomenon. The influence of the support is evident in Figure 31, where the amount of adsorbed CO decreased with the decreasing acidity of the zeolites (52 > 91 > 371).

However, the strength of CO interaction did not follow a pattern with the zeolite acidity/basicity. As observed in the NH₃-TPD, the Fe-Z91DI catalyst also exhibited a different behavior, presenting weaker adsorption sites for CO when compared to the Fe-Z52 and Fe-Z371 catalysts. The final stage of CO desorption for Fe-91ZDI catalyst occurred at 560°C whereas for the Fe-Z52 and Fe-Z371 catalyst were at 750°C. The Fe-Z371DI catalyst exhibited the strongest interaction with CO, with 0.46 mmol/g_{catalyst} of CO adsorbed at higher temperatures. This result aligns with results reported previously, as CO is a well-known acidic gas and exhibits a stronger attraction for basic surfaces, thereby augmenting its adsorption capability.¹¹⁷

5.2 FISCHER-TROPSCH PERFORMANCE ASSESSMENT

5.2.1 Evaluation of catalytic activity with temperature screening

Initially, the catalysts were tested by varying the temperature to observe its influence on CO conversion. The tests were conducted using the Fe-Z91DI and Fe-Z91PM catalysts at three different temperatures. Subsequently, the system was cooled down to an intermediate temperature to evaluate the catalyst activity. The results are shown in Figure 32.

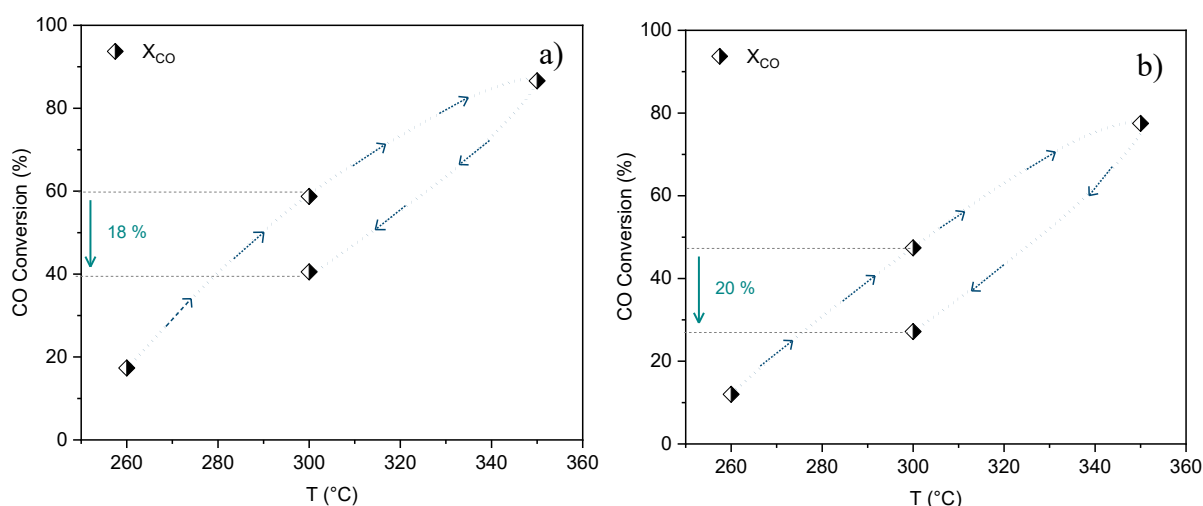


Figure 32 - Fischer-Tropsch activity evaluation with temperature screening.
a) Fe-Z91DI and b) Fe-Z91PM. P=20bar, H₂/CO=2, WHSV=6880 mL.g⁻¹.h⁻¹.

The Fe-Z91DI sample showed an increasing CO conversion with increasing temperature, starting at 17% at 250°C and reaching a maximum of 86% at 350°C. The Fe-Z91PM showed CO conversion from 12 to 77% over the same temperature range. In fact, increasing the temperature favors the Fe carbidization¹⁶² and CO dissociation, and consequently the number of available C atoms on active surface sites, leading to higher conversions.¹⁶³

Noteworthy is that the catalyst prepared by impregnation exhibited a higher CO conversion compared to the catalyst prepared by physical mixing at all temperatures. Indeed, at 300°C, the CO conversion was 11% higher for Fe-Z91DI than for Fe-Z91PM.

The influence of Fe deposition into HZSM-5 channels on the FTS results still needs to be better explored in the literature¹⁶⁴. Nevertheless, it is known that different methods of Fe loading on zeolites might change the size, dispersion, and location of iron species on the support, as discussed in section 5.1.7. In this work, it was observed that particles with smaller crystallite sizes (~23 nm) presented a slightly higher CO conversion than the larger ones (~30 nm).

A slight difference in the liquid hydrocarbon selectivity between the two catalysts evaluated was observed, as shown in Appendix C. The Fe-Z91DI catalyst showed higher selectivity for gasoline-range products (28 %) than Fe-Z91PM catalyst (23%). The occurrence of parallel WGS reaction was observed for both catalysts. The catalyst prepared by physical mixing exhibited a higher CO₂ selectivity compared to the catalyst prepared by dry impregnation, as shown in Figure 33. At the temperature of 350°C, CO₂ reached 54% of selectivity for the Fe-Z91PM and 34% for the Fe-Z91DI. Thus, further investigation of catalytic performance in this work was carried out with catalysts prepared by dry impregnation method.

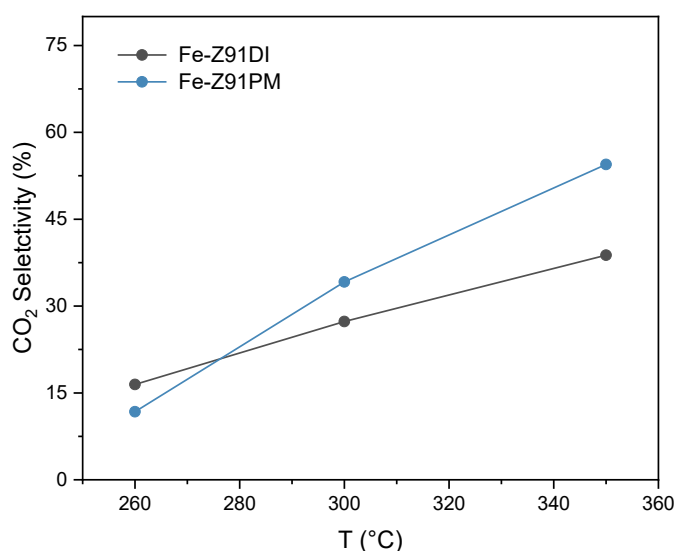


Figure 33 - CO₂ selectivity during Fischer-Tropsch reaction with temperature screening. P=20bar, H₂/CO=2, WHSV=6880 mL.g⁻¹.h⁻¹.

Additionally, as depicted in Figure 32, a decrease in CO conversion was observed when the catalysts were tested at lower temperatures after reaching the maximum conversion at 350°C. This decline indicates a loss of activity for both materials. In fact, CO conversion of the

Fe-Z91DI catalyst decreased from 59% to 40% whereas for the Fe-Z91PM from 47% to 27%. The literature has reported that Fe-based catalysts may undergo changes during the reaction⁸¹, which can be attributed to sintering, coke deposition, and/or metal phase transformations. Likewise, the zeolite support of the bifunctional catalyst can suffer deactivation due to the coke deposition in the zeolite channels or dealumination of the crystals.¹⁶⁵

Eliason and Bartholomew (1999)¹⁶⁶ proposed different parallel deactivation mechanisms for unsupported Fe catalysts in FTS, such as the conversion of atomic carbon to graphitic carbon and/or the transformation of active carbon-rich carbides to inactive carbon-poor carbides. Ning et al. (2006)¹⁶⁷ reported a similar conclusion for Fe-based catalysts, suggesting that the oxidation of Fe carbides and the formation of amorphous carbonaceous compounds were the main factors for the loss of activity. In the context of zeolite deactivation, Botes (2005)¹⁶⁸ investigated the effect of temperature on the deactivation of Fe-HZSM-5 in FTS. This study revealed that at 350°C, the rate of coke formation inside the zeolite pores was low, while the rate of coking on the external surface of the support increased, in contrast to a temperature of 330°C.

Hence, based on the existing literature, the decreasing activity with increasing temperature, observed in Figure 32 can be attributed to the transformation of the Fe phase into inactive species and/or the formation of coke on both zeolite and Fe sites. It is noteworthy that at 350 °C, the higher CO conversion implies a greater amount of adsorbed C species on the catalyst sites, which could potentially undergo Fischer-Tropsch synthesis or even form coke, possibly via the Boudouard reaction (Eq. 5).



5.2.2 The effect of zeolite SiO₂/Al₂O₃ ratio on catalytic activity and product selectivity

The effect of the support acidity on product distribution and activity was studied using three catalysts of Fe/HZSM-5 prepared by dry impregnation method with supports of different SiO₂/Al₂O₃ ratios. The results are shown in Figure 34 and Figure 35.

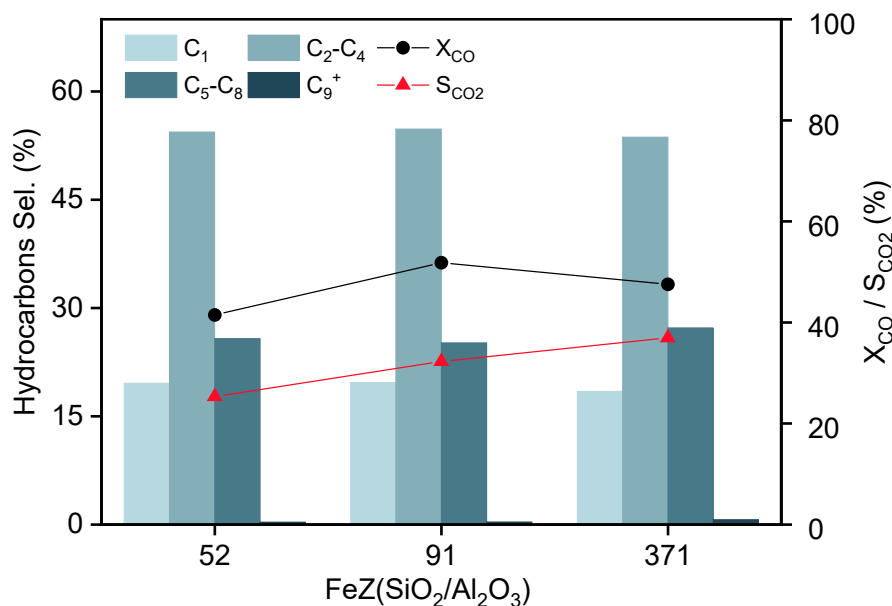


Figure 34 - Effect of SiO₂/Al₂O₃ ratio on FTS activity and product distribution. Fe-Z52DI, Fe-Z91DI and Fe-Z371DI catalysts. T=300°C, P=20bar, H₂/CO=2, WHSV=6880 ml.g⁻¹.h⁻¹.

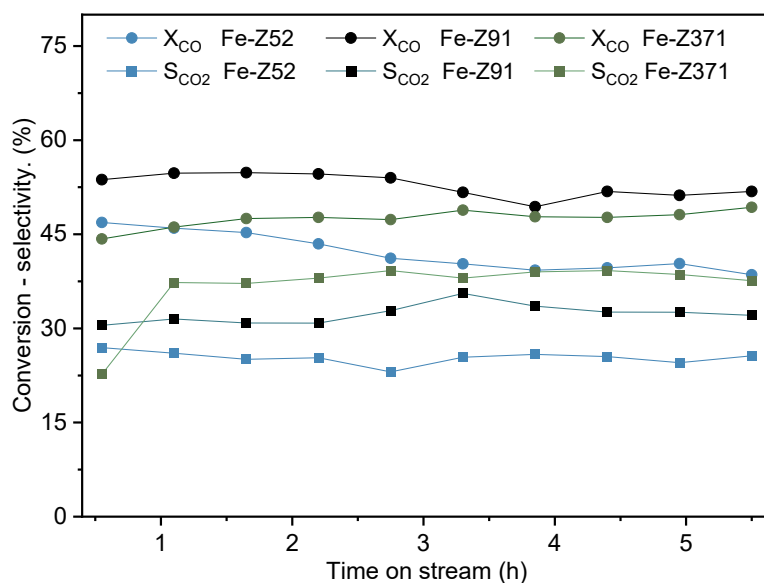


Figure 35 - Effect of SiO₂/Al₂O₃ ratio on FTS activity during time on stream (TOS). Fe-Z52DI, Fe-Z91DI and Fe-Z371DI catalysts. T=300°C P=20bar, H₂/CO=2, WHSV=6880 ml.g⁻¹.h⁻¹.

Zeolites with different SiO₂/Al₂O₃ ratios have different quantities of Lewis and Bronsted acid sites, which influence the adsorption and re-adsorption of molecules for occurrence of cracking and oligomerization reactions. Generally, the lower the SiO₂/Al₂O₃ value is, the more acidic the material is, due to the higher presence of Al³⁺ in the framework.¹¹⁷

The results from Figure 34 and Figure 35 showed that the zeolite with SiO₂/Al₂O₃ ratio of 52 presented the lowest CO conversion with the time, despite showing the lowest CO₂ selectivity, while the supports with medium (91) and high SiO₂/Al₂O₃ ratio (371) showed

similar CO conversion, about 50% at the end of testing. Even though the zeolite acidity may influence CO conversion, it should be noted that Fe NPs also affects FTS and WGS activities.¹²⁷

When evaluating FTS activity, the Fe-Z91DI catalyst exhibited the best result among the studied catalysts. Liu et al. (2021)¹¹⁷ emphasized the importance of balancing strong, medium and weak acid sites on the catalyst to enhance oligomerization/cracking effects and prevent coke formation in zeolite channels. This aligns with the results observed for Fe-Z91DI catalyst. NH₃-TPD analysis revealed that Fe-Z91DI was the only catalyst that exhibited weak, medium and strong acid sites, with the highest number of acid sites. Additionally, CO-TPD results indicated that Fe-Z91DI exhibited weaker adsorption sites for CO in comparison to Fe-Z52DI and Fe-Z371DI.

Product selectivity did not change among the catalysts studied. It is known that the acidity, porosity and the metal particle dispersion on the zeolites are the key parameters influencing the secondary reactions, affecting selectivity, as observed in section 2.8. Hence, it seems that the porosity, dispersion/confinement of metal particles on the zeolite framework may have narrowed the influence of acidity on the hydrocarbon's distribution, as observed in the literature.¹¹³

5.2.3 The effect of temperature on conversion and product selectivity

For evaluating the effect of temperature on product distribution and conversion, the Fe-Z91DI catalyst was tested at four different temperatures and the results are shown Figure 36.

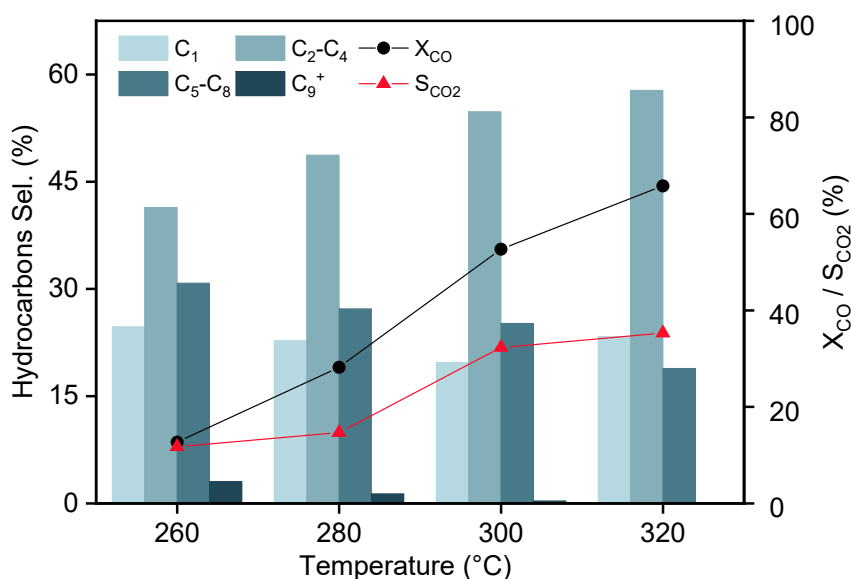


Figure 36 - Effect of temperature on FTS activity and product distribution. Fe-Z91DI catalyst. P=20bar, H₂/CO=2, WHSV=6880 ml.g⁻¹.h⁻¹.

The overall product distribution for all catalysts exhibited a greater formation of light chain hydrocarbons, C₂-C₄, with selectivity around 47-57%. Then, liquid hydrocarbons in the gasoline range, C₅-C₈, were produced (18-31%), followed by CH₄ (19-24%) and heavier liquid hydrocarbons, C₉-C₁₂, (0-3%).

Indeed, the temperature exhibited a considerable influence on product distribution, CO₂ selectivity, and CO conversion. It was observed that as the temperature increased, the reaction favored the formation of light chain hydrocarbons, with C₂-C₄ selectivity increasing from 4% to 57%, while C₅-C₈ selectivity decreased from 31% to 18% as the temperature rose from 260 to 320 °C. This effect was expected, since the reaction temperature has a positive influence on the termination rate of hydrocarbons during the polymerization mechanism, which tends to the formation of shorter chains.¹⁶⁹

It is worth mentioning that increasing temperature presented substantially influence on both CO conversion and CO₂ selectivity. At 320°C the values of CO conversion and CO₂ selectivity reached 66% and 35%, respectively, while at 260°C these values were 13% and 12%. The greater CO conversion observed is explained by the increase in CO dissociation over the active sites and the occurrence of WGS reaction.

The greater CO₂ selectivity observed indicates that the WGS reaction becomes more pronounced at higher temperatures. In fact, this is a typical behavior of Fe-based catalysts in the FTS at temperatures above 300°C.¹²⁷ The temperature is a key parameter for the WGS reaction, influencing the CO equilibrium concentration and the kinetics. Additionally, Fe₃O₄ is an active phase for WGS, and its rate-determining step is usually ascribed to the reaction of a gaseous CO or H₂O molecule with a surface oxygen atom or an oxygen vacancy from the catalyst.⁷⁹

5.2.3.1 ASF distribution

Even though bifunctional catalysts may present deviations from the ASF distribution model for FTS, the principles of this theory remain essential for explaining the influence of some reaction parameters, such as temperature on product selectivity. As discussed in section 2.4, the chain growth probability factor (α) from the ASF model, shown in Eq 9, is defined based on the rates of chain propagation (r_p) and termination (r_t). These reaction rates are dependent on the kinetic constants and amount of adsorbed *H*- and *CH*₂- species on the catalyst sites, all influenced by temperature.

According to the literature⁵⁹, the observed change in product selectivity with increasing temperature is that the chain termination step usually has higher activation energy than the propagation step, decreasing the α value⁵⁹. This finding was observed in the ASF fitted models, as shown in Figure 37 for the tests conducted at different temperatures. The results show an increase of a value from 0.43 to 0.56 with the temperature decrease, which signs the influence of temperature on the propagation/termination behavior during the reaction.

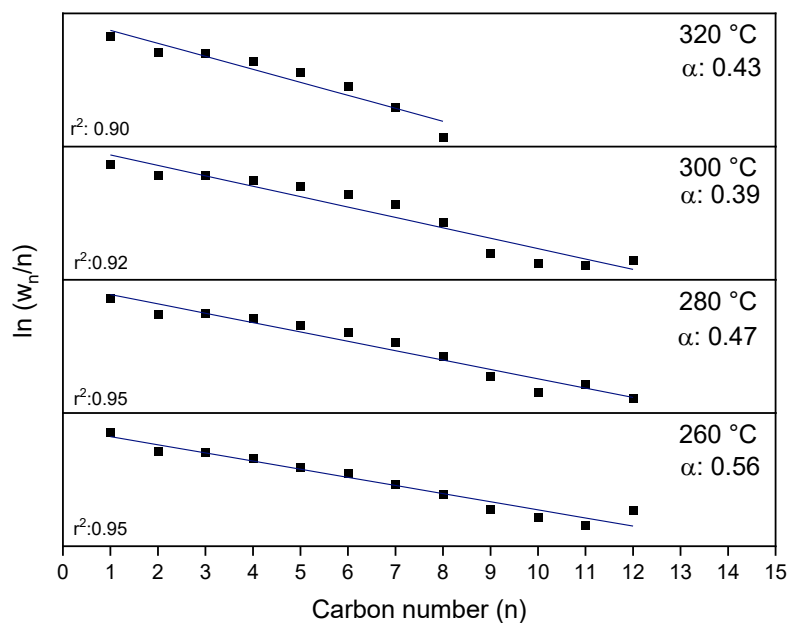


Figure 37 - ASF fitted model for FTS tests under different temperatures. Fe-Z91DI catalyst. P=20bar, H₂/CO=2, WHSV=6880 ml.g⁻¹.h⁻¹.

5.2.4 The effect of space velocity on catalytic activity and product selectivity

For evaluating the effect of space velocity on product distribution and activity with the Fe-Z91DI catalyst, three testes were carried with different space velocities by changing the total flow rate of syngas. The results are shown in Figure 38.

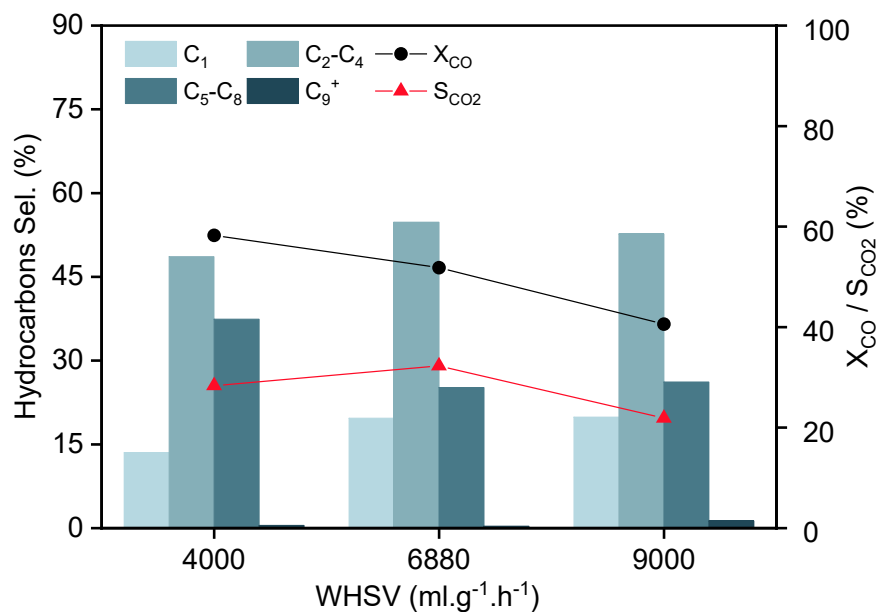


Figure 38 - Effect of WHSV on FTS activity and product distribution. Fe-Z91DI catalyst. T=300°C, H₂/CO=2, P=20 bar.

The results showed that the space velocity has considerable influence on both CO conversion and product selectivity. The CO conversion decreased from 58% to 40% with increasing the space velocity from 4000 to 9000 ml.g⁻¹.h⁻¹. By increasing WSHV, the contact time between the syngas and the catalyst is lower, resulting in lower CO conversion, as observed in previous work reported in the literature for this reaction.^{62,125}

The decreasing space velocity showed a positive influence on liquid production in the gasoline range. At 4000 ml. g⁻¹.h⁻¹, the selectivity for C₅-C₈ hydrocarbons was 37%, which was the highest percentage obtained among all conditions evaluated. At the same time, the methane, and light hydrocarbons (C₂-C₄) selectivity decreased with decreasing space velocity. Although some authors did not report a change in product selectivity with varying WHSV^{59,125}, the effect of space velocity on product distribution in FTS is relatively complex and depends on the other reaction conditions.⁶² However, it is known that a greater residence time of CO and H₂ usually favors chain growth.⁶²

5.2.5 The effect of pressure on catalytic activity and product selectivity

FTS tests were carried out at different pressures for evaluating the effect of this parameter on CO conversion and product selectivity. The results are shown in Figure 39.

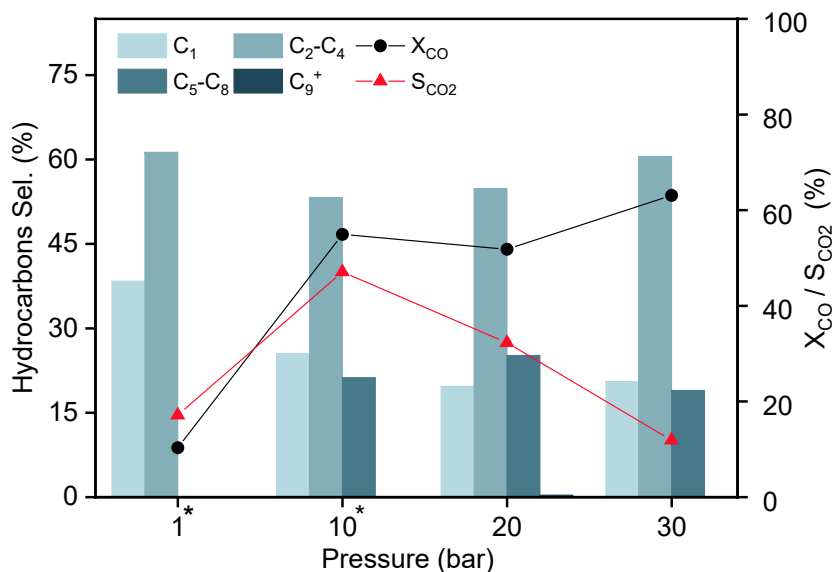


Figure 39 - Effect of pressure on FTS activity and product distribution.

Fe-Z91DI catalyst. T=300°C, H₂/CO=2, WHSV=6880 ml.g⁻¹.h⁻¹. * Tests with WHSV=4000 ml.g⁻¹.h⁻¹

The results showed that an increase in the reaction pressure leads to an increase of the overall CO conversion, starting at 10% at 1 bar and reaching a maximum of 63% at 30 bar. The growing CO conversion with pressure was expected, since pressure improves CO adsorption at the catalyst surface, which improves the overall FTS activity⁶⁰. The results showed a large difference of CO conversion between 1 bar and 10 bar, which reinforces the need of higher pressure for favoring this reaction, as observed.⁶⁰

Regarding product selectivity, higher pressure conditions are known to lower methane formation and favor the selectivity of C₅⁺ hydrocarbons¹⁷⁰. Figure 39 evidenced that, at 1 bar, the methane selectivity was 38% and the C₅⁺ selectivity was negligible. In contrast, at 10 bar, it was obtained 25% for methane selectivity and 24% for C₅⁺ selectivity.

De la Peña O'Shea et al. (2005)¹⁷¹ suggested that increasing total pressure in FTS improves the chain propagation of -CH_x- on the catalyst surface, leading to higher selectivity for higher hydrocarbons. However, this tendency could not be observed in Figure 39 at pressures between 20 and 30 bar, in which product selectivity did not change considerably with pressure variation. Botes et al. (2013)¹⁷² observed a similar result and pointed out that the variation in pressure had a lower effect on product selectivity for Fe-based catalysts.

5.2.6 The effect of feed composition on catalytic activity and product selectivity

For evaluating the effect of feed composition on CO conversion and product selectivity, FTS tests were carried out under three different feed H₂/CO for the Fe-Z91DI catalyst. The results are shown in Figure 40, and the ASF fitted curves are presented in Figure 41.

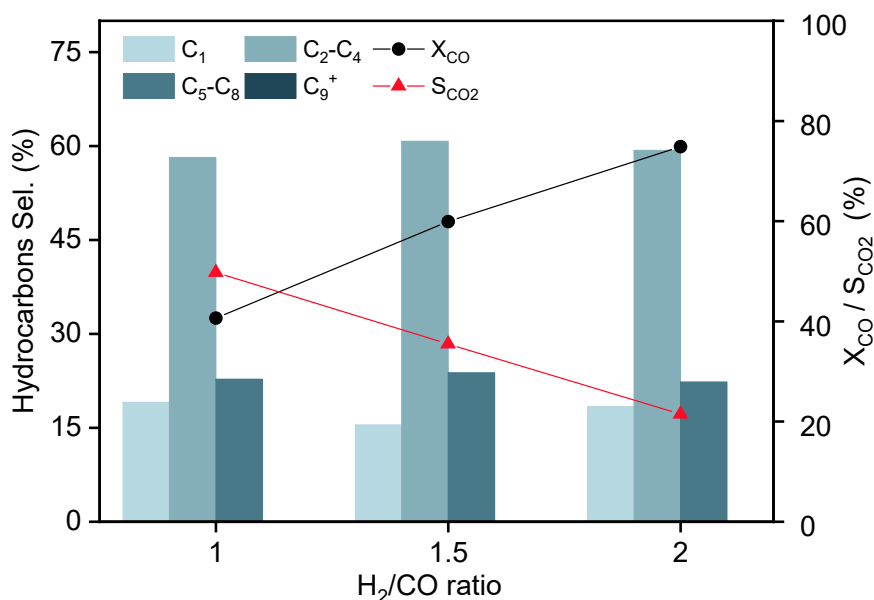
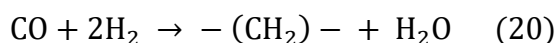


Figure 40 - Effect of H₂/CO ratio on FTS activity and product distribution. Fe-Z91DI catalyst. T=300°C P=20bar. WHSV=4000 ml.g⁻¹.h⁻¹.

The results showed an increase of CO conversion from 41% to 75% with an increase of hydrogen in the feed. In fact, Fischer-Tropsch synthesis is known to present low CO conversion under poor hydrogen environment, as the hydrogen partial pressure is crucial for kinetics of Fe-based catalysts, as shown in Eq. 20.¹⁷³



It is noteworthy that CO₂ selectivity decreased from 49% to 21% with an increasing hydrogen feed ratio. This change occurred due to the equilibrium nature of the water-gas-shift reaction, as shown in Eq. 6. An increase in hydrogen partial pressure shifts the reaction equilibrium toward the reverse water-gas-shift reaction, decreasing CO₂ production. Thus, for this catalyst, higher hydrogen pressure increased CO conversion while reduced CO₂ selectivity, favoring FTS reaction over the parallel WGS reaction. This finding is in good agreement with Burgun et al. (2023)¹⁷⁴ that studied Fe-Cu catalysts supported on zeolite Y and mordenite for the FTS. The catalysts showed a decrease of CO₂ with a higher H₂/CO ratio.

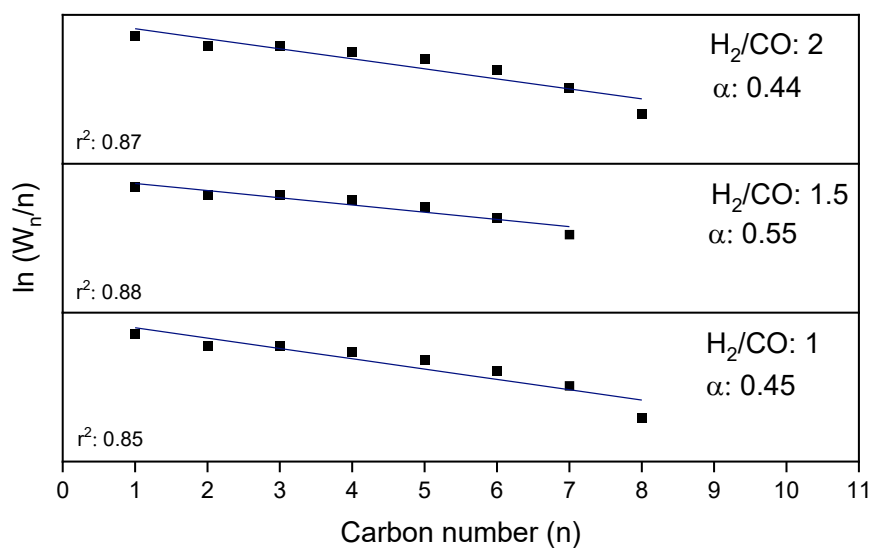


Figure 41 - ASF fitted model for FTS tests under different H₂/CO ratios. Fe-Z91DI catalyst. T=300°C P=20bar, WHSV=4000 ml.g⁻¹.h⁻¹.

Theoretically, increasing H₂/CO ratio is suitable for hydrogenation activity, favoring methane and lighter hydrocarbon selectivity. Actually, this trend was not observed at lower H₂ concentrations (between H₂/CO =1 and 1.5). However, as the H₂/CO ratio increased from 1.5 to 2.0, methane formation augmented, leading to an expected decrease in the α-value, as shown in Figure 41.

5.2.7 Stability test

A time on stream test of 72 hours was carried out with the Fe-Z91DI catalyst in order to evaluate its stability. The results are shown in Figure 42.

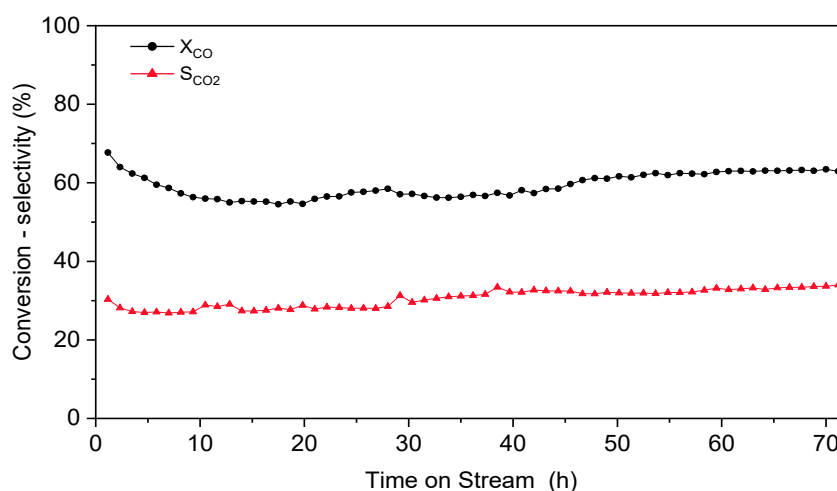


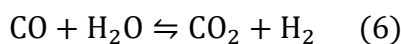
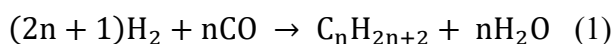
Figure 42 – FTS time on stream test. Fe-Z91DI catalyst. T=300°C, P=20 bar, H₂/CO=2, WHSV=4000 ml.g⁻¹.h⁻¹.

The results from Figure 42 showed that the Fe-Z91DI catalyst exhibited a good stability during the FTS reaction under the evaluated conditions. The CO conversion remained practically constant at the end of the test with an average value of 63%, and no signs of deactivation were observed throughout the test.

A rapid initial loss of activity was observed during the test, with CO conversion decreasing from 68% to 55%. This behavior is consistent with the findings of Burgun et al. (2023)¹⁷⁴, who reported a similar initial decrease in CO conversion while testing Fe catalysts supported on zeolite Y and mordenite for FTS. According to the authors, initial coke deposition was regarded as a possible explanation to the decrease in the catalyst activity.

It was also observed a slight increase in CO conversion at the end of the time of stream. This behavior may be attributed to the stabilization time required for the formation of iron carbide phases. Previous studies¹⁷⁵ reported *in situ* characterization of Fe catalysts under Fischer-Tropsch synthesis (FTS) conditions, demonstrating the gradual formation of the Fe₅C₂ phase as the iron oxide phase decreases over time. Thus, to confirm and understand such behavior in Fe-Z91DI catalyst, conducting an *in situ* XRD analysis would be crucial to evaluate the transformation of iron phases on the catalyst surface over time.

The curves in Figure 42 also shows a nearly constant difference between CO conversion and CO₂ selectivity. Since no signs of deactivation were observed, the stability could be explained by the relation of equilibrium between FTS (Eq. 1) and WGS (Eq. 6) reactions. High activity for WGS favors the oxidation of CO into CO₂, but at the same time increases the production of H₂, favoring the FTS⁷⁹. Moreover, Fe-based catalysts are also known to catalyze the conversion of CO₂ to CO via RWGS (Eq. 21), making CO and CO₂ interconvertible in this process.¹⁶⁴



5.3 POST-REACTION CATALYST CHARACTERIZATION

5.3.1 Infrared and RAMAN spectroscopies

In order to evaluate the structure of the catalyst and possible carbon deposition on the surface after reaction, FTIR and RAMAN spectroscopy analyses were performed on the spent catalyst and the results are shown in Figure 43 and Figure 44 respectively.

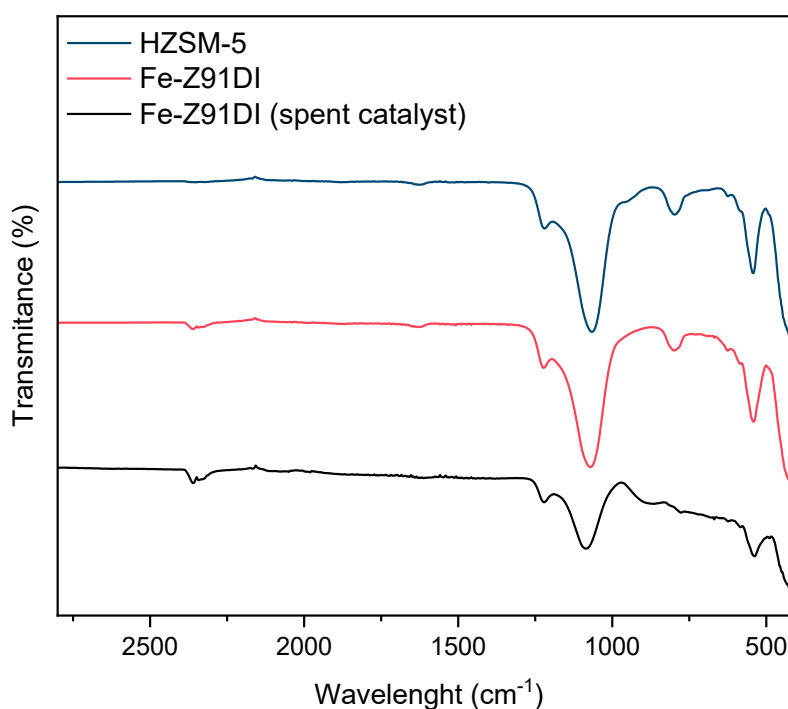


Figure 43 – Post-reaction FTIR spectroscopy analysis with the Fe-Z91DI catalyst.

The results presented in Figure 43 shows a diminution of band intensity between 400-1300 cm⁻¹ in the spent catalyst. These bands correspond to vibrations of the tetrahedral framework within the zeolite. Particularly it was notable the decrease in intensity observed around 550 cm⁻¹ and 1230 cm⁻¹, characteristic of 5-membered ring blocks in HZSM-5. This observation may suggest structural alterations within the zeolite after the reaction.

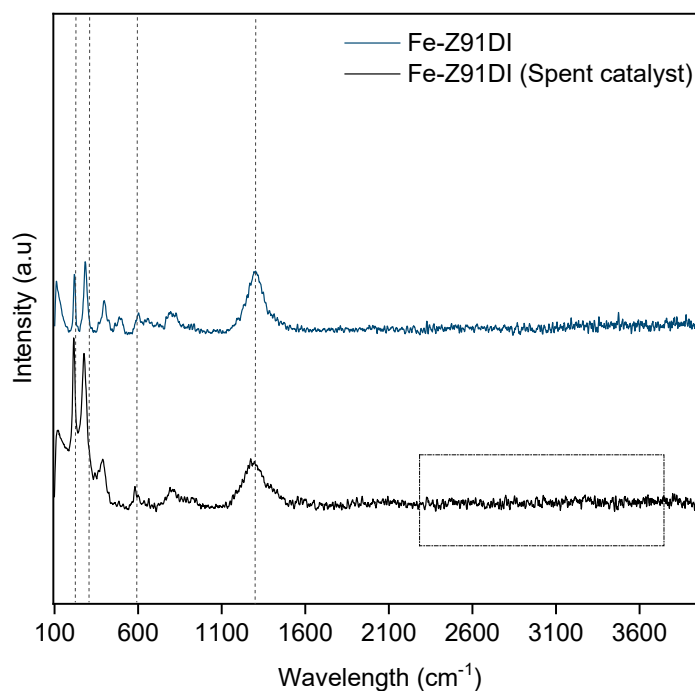


Figure 44 – Post-reaction RAMAN spectroscopy analysis with the Fe-Z91DI catalyst.

The RAMAN analysis showed distinctive bands of the catalysts that did not exhibit significant changes or shifts. Additionally, bands associated with carbon vibrations indicating coke deposition on the catalyst surface were not observed in the spectra. These absences suggest that coke deposition via Boudouard reaction was not prominent under the evaluated conditions. This finding elucidates the observed stability of the catalyst over the 72-hour test on stream, as depicted in Figure 42.

5.3.2 X-ray diffraction (XRD)

Figure 45 presents the diffractogram of the Fe-Z91DI catalyst before and after the reaction.

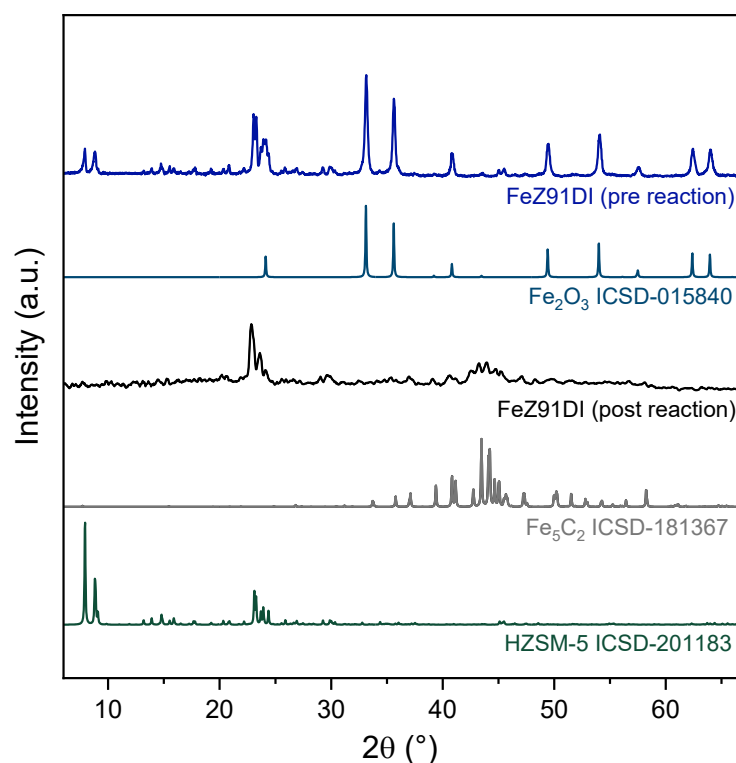


Figure 45 – Pre- and Post-reaction XRD analyses with the Fe-Z91DI catalyst.

The results observed in the diffractogram indicate that the catalyst suffered alteration in its structure after the reaction. First, the peaks assigned to the phases of H-ZSM5 at 2θ around 23.0° , and 24.1° did not change their position or intensity significantly in the post-reaction catalyst. However, the peaks at $2\theta = 7.9$ and 8.8° disappeared on the spent catalyst. This implies that the zeolite structure might persist after the reaction but with reduced crystallinity and/or a different arrangement.

Notably, the diffractogram of the post-reaction catalysts did not show peaks related to the crystalline phases of Fe_2O_3 . This absence suggests that the crystalline hematite phases might have been transformed into amorphous Fe_2O_3 or into iron carbides. The slight peaks observed at 41 - 47° were assigned to the Fe_5C_2 Hagg-carbide, which is an active phase for Fischer-Tropsch reaction¹⁷⁶. According to Smit and Weckhuysen (2008)¹⁷⁷, the study of iron carbide particles by XRD is complex by the fact that the carbides particles formed over the iron oxide particles are usually small. This leads to broadened Bragg reflections with low intensity, consistent with the diffraction signals noted in the present study.

5.3.3 Transmission Electron Microscopy (TEM)

In order to observe particles configuration after reaction, transmission electron microscopy images were taken from the post-reaction Fe-Z91DI catalyst, and the results are shown in Figure 46.

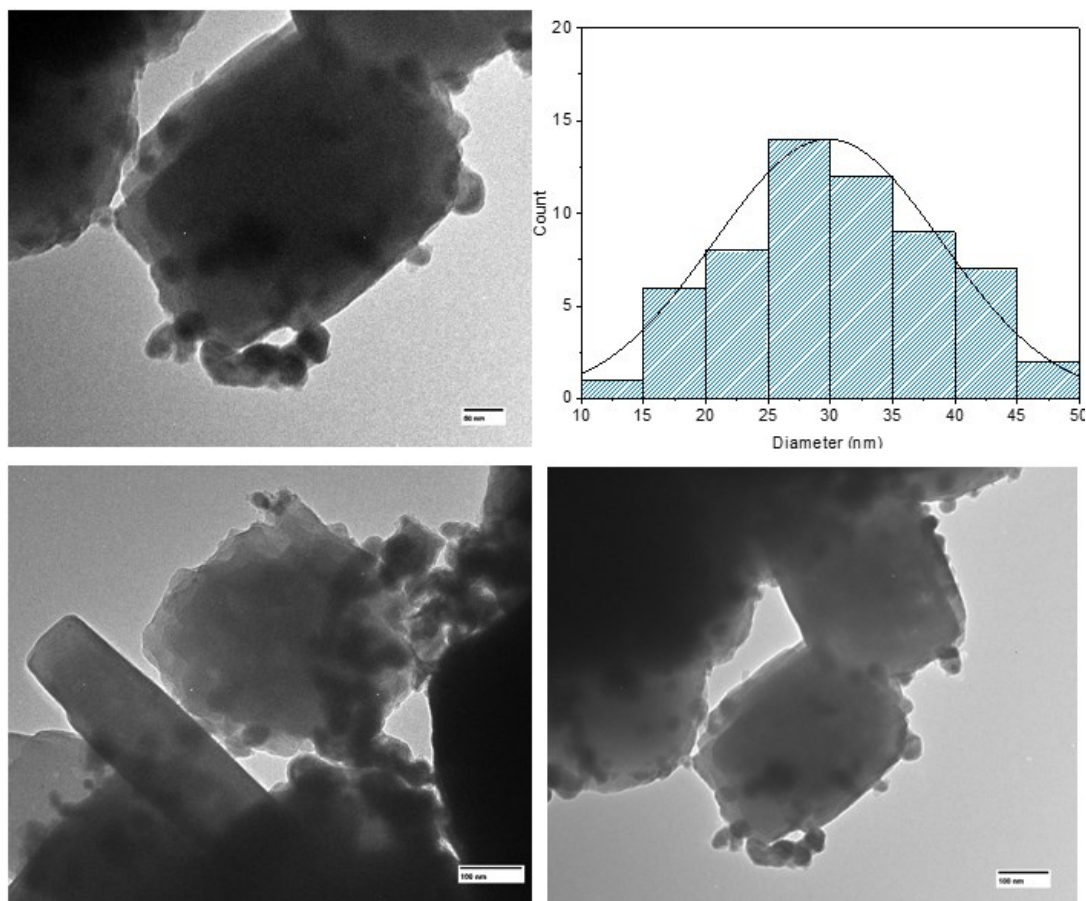


Figure 46 - Post-reaction TEM images of the Fe-Z91DI catalyst.

The images showed a heterogeneous distribution of the particles on the surface as observed on the fresh catalyst in Figure 25. The particles retained their spherical shape; however, a slight increase in the average particle diameter was noted. The fresh catalyst exhibited an average particle diameter of 22 nm, while the spent catalyst had an average particle diameter of 29 nm. Moreover, it was not observed the presence of filaments assigned to amorphous coke deposition, which corroborates with the findings of the RAMAN spectrum. Consequently, no signs of coke were observed, and the surface of the spent catalyst remained unchanged.

5.4 FISCHER-TROPSCH KINETIC ASSESSMENT

5.4.1 Kinetic regime determination

When a reaction occurs within a packed bed filled with catalyst particles, the global reaction rate can be influenced by both the chemical reaction rate and mass transfer of reactants through fluid flow and catalyst pores.¹⁷⁸ According to Schmal and Pinto (2021)¹⁷⁸, the acquisition of good quality kinetic data must be carried out without influence of external and internal mass transfer phenomena, so that the measured reaction rate is exclusively related to the chemical reaction effects. The mitigation of mass transfer limitations can be assured by changing the hydrodynamics inside the reactor. Usually, increasing space velocity or reducing the particle size of the catalyst are the used strategies to get on the kinetic regime of the reaction.¹²⁸

Therefore, prior to collecting kinetic data for model fitting, the FTS W/F_{syg} vs X_{CO} curve was taken for the Fe-Z91DI catalyst. The tests were conducted by varying either the catalyst mass or the reactant syngas flowrate and the results are shown in Figure 47.

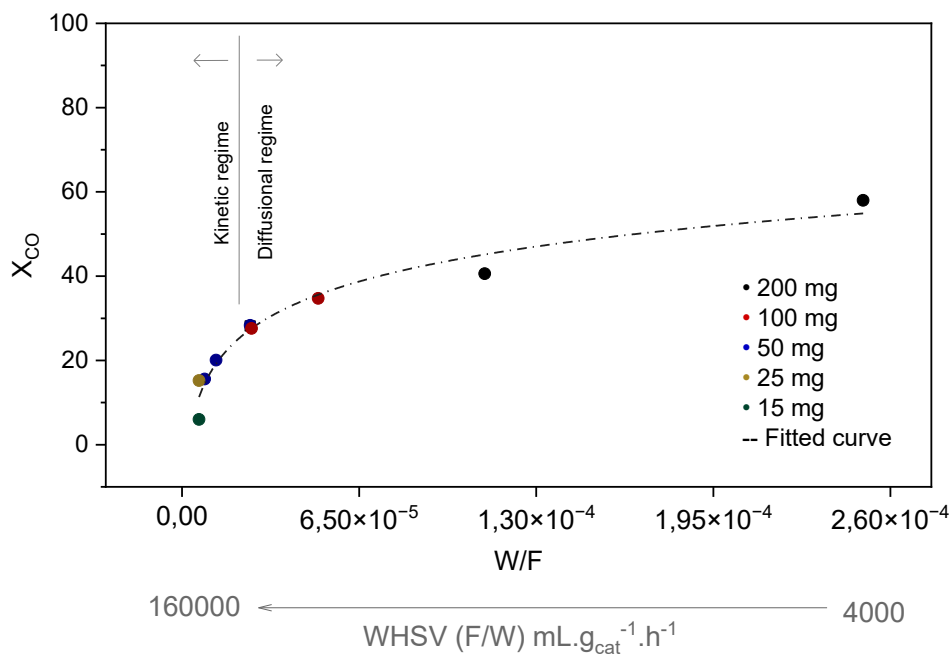


Figure 47 - W/F_{syg} vs X_{CO} for the Fe-Z91DI.

$T=300^{\circ}\text{C}$, $P=20$ bar, $\text{H}_2/\text{CO}=2$, $\text{WHSV}=4000, 9000, 20000, 40000, 80000, 120000$ and 160000 $\text{mL.g}^{-1}.\text{h}^{-1}$.

As expected, the X_{CO} curve exhibits a logarithmic behavior in relation to the W/F_{syg} ratio. The higher X_{CO} values and their lower variation, at higher W/F_{syg} range, indicate the

region where the diffusional regime occurs. In contrast, the lower observed X_{CO} values at the lower W/F range point to the region in which the kinetic regime is close to be established.

To ensure the mitigation of internal and external diffusion limitations, the Weiz-Prater criterion and Mears criterion were estimated according to Fogler (2020)¹²⁸ under the conditions used in Figure 47 with the highest WHSV value of 160000 ml.g⁻¹.h⁻¹. The criterion values and the parameters and variables used to calculate them are shown in Table 7.

Table 7 - Parameters of Weiz-Prater and Mears criteria calculation.

Parameter/Variable	Value	Unit	C_{wp}	MR
$-r_{CO}$ ^a	$6.08 \cdot 10^{-5}$	mol.g _{cat} ⁻¹ .s ⁻¹		
ρ_c ^a	0.757	g.cm ⁻³		
R ^b	$4.77 \cdot 10^{-3}$	cm		
C_{COs}, C_{ab} ^a	$1.27 \cdot 10^{-4}$	mol.cm ⁻³	0.425	$5.27 \cdot 10^{-5}$
D_{AB} ^c	0.081	cm ² .s ⁻¹	($C_{wp} < 1$)	(MR < 0.15)
D_{eff} ^d	0.0081	cm ² .s ⁻¹		
ϕ ^e	0.4	mol.g _{cat} ⁻¹ .s ⁻¹		
k_c ^f	0.19	m.s ⁻¹		

^aExperimentally determined, ^bEstimated by Sauter diameter from experimental granulometry, ^cEstimated by ApenProperties using Chapman-Enskog correlation considering the CO diffusion on reactant flow. ^dEstimated according to [179], ^eEstimated according to [180], ^fEstimated using Thoenes-Kramers correlation¹⁸¹.

Based on the values calculated for the Weiz-Prater and Mears criteria, along with the observed curve behavior shown in Figure 47, it can be concluded that mass transfer effects can be disregarded and that the system operates within the kinetic regime using a WHSV of 160000 ml.g⁻¹.h⁻¹.

5.4.2 Kinetics data acquisition

According to the literature, kinetic models for CO conversion in FTS can be described in the form: $-r_{CO} = f(T, p_{H_2}, p_{CO}, p_{CO_2}, p_{H_2O})$, as explained in section 2.3.2. The experiments for kinetic data acquisition were conducted using a WHSV of 160000 ml.g⁻¹.h⁻¹ with variations

in temperature and inlet H₂/CO (pH₂/pCO) ratios. It was assumed a differential flow reactor to calculate the experimental reaction rate, as explained in section 4.4.2.

Experimental data were collected at four different temperatures: 533.15 K, 553.15 K, 573.15 K, and 583.15 K, employing various inlet H₂/CO ratios: 1.0, 1.5, 2.0, and 3.0, similar to the method used by Mirzhaei et al. (2020).⁵¹ For each reaction condition, experiments were conducted in triplicate, resulting in a total of 41 usable data points for regression study. The kinetic results of the 41 points are detailed in Appendix B, and the average kinetic values for each condition are summarized in Table 8.

Table 8 - Experimental conditions and results for kinetic tests with the Fe-Z91DI catalyst.

Exp.	T (K)	H ₂ /CO	pH ₂ (bar)	pCO (bar)	pCO ₂ (bar)	pH ₂ O (bar)	X _{CO} (%)	-r _{CO} ' (mmol/min.g _{cat})
1	533.15	2.0	10.00	7.21	0.009	0.34	4.76	2.06
2	533.15	3.0	11.37	5.69	0.010	0.37	6.38	2.12
3	553.15	1.0	7.34	9.91	0.015	0.37	3.88	2.47
4	553.15	1.5	8.78	8.33	0.018	0.39	4.83	2.51
5	553.15	2.0	9.95	7.12	0.020	0.43	6.18	2.68
6	553.15	3.0	11.37	5.56	0.023	0.50	8.95	2.97
7	573.15	1.0	7.02	9.94	0.075	0.48	6.00	3.81
8	573.15	1.5	8.49	8.23	0.057	0.58	7.80	4.06
9	573.15	2.0	9.65	7.06	0.067	0.51	8.41	3.65
10	573.15	3.0	11.06	5.42	0.076	0.60	12.20	4.05
11	583.15	1.0	6.94	9.57	0.066	1.02	10.77	6.85
12	583.15	1.5	8.31	7.93	0.076	1.17	14.24	7.41
13	583.15	2.0	9.33	6.82	0.086	1.11	15.89	6.89
14	583.15	3.0	10.70	5.23	0.096	1.10	19.77	6.56

*T = 533-583 K, P=20 bar, H₂/CO = 1-3, WHSV = 160000 ml.g⁻¹.h⁻¹

The experimental results presented in Table 8 showed values of X_{CO} ranging from 4.76% to 19.77 % under the evaluated conditions. It is evident that the experimental reaction

rate was significantly influenced by the temperature increase, whereas both temperature and H_2/CO feed ratio affected X_{CO} .

Common CO consumption reaction rate models for FTS are derived from the Langmuir-Hinshelwood-Hougen-Watson (LHHW) kinetics approach. The LHHW model considers that the reaction rate is controlled by adsorption terms, with the following assumptions: the catalyst surface has a defined number of adsorption sites, each site can adsorb one molecule, all sites are energetically equal, adsorption enthalpy does not depend on the sites coverage degree, adsorption and desorption rates are equal at the equilibrium, a rate determining step is assumed.¹⁸²

As detailed in Section 2.3.1, FTS mechanisms can proceed via diverse routes. The main differences between the mechanism lie on the structure of the specie that initiates the chain growth step and in the oxygen removal step. It is generally agreed that the formation of the monomer is a very low step compared to the chain growth and desorption step¹⁸³. Consequently, the rate-determining step (RDS) in CO consumption is commonly attributed to the monomer formation step.

As a result of the different proposed routes, LHHW rate models vary in their considerations of the mechanism, such as the associative or dissociative adsorption of H_2 or CO, the occurrence of a single or double site reaction step, and the relative adsorption strength of the molecules. In light of this, a collection of 10 LHHW models for Fe-based catalysts was selected to fit the data acquired (Table 7). These models were assessed for the possible influence of the main molecules (CO, H_2 , CO_2 , and H_2O) on the adsorption term, taking into account different adsorption mechanisms (associative or dissociative) and the reaction sites involved (single or double site). The results of the non-linear regression are shown in Table 9.

Table 9 - Results of fitted kinetic models for CO conversion on Fe-Z91DI catalyst.

Model	k_0	E_a (kJ/mol)	k_{10}	$H_{ads(1)}$ (kJ/mol)	k_{20}	$H_{ads(2)}$ (kJ/mol)	Statistical parameters			Ref
							R^2	F	RMSE	
1 $r = \frac{k pH_2^{0.5} pCO^{0.5}}{(1 + K_1 pCO^{0.5} + K_2 pCO_2)^2}$	$1.16 \cdot 10^6$	78.583	$5.56 \cdot 10^{-2}$	-17.778	$7.00 \cdot 10^{-8}$	-98.8112	0.923	84.78	0.00057	52
2 $r = \frac{k pH_2^{0.5} pCO}{(1 + K_1 pCO^{0.5} + K_2 pCO_2)^2}$	$9.45 \cdot 10^6$	69.903	$2.42 \cdot 10^0$	-13.678	$3.29 \cdot 10^{-8}$	-112.540	0.911	73.56	0.00061	184
3 $r = \frac{k pH_2 pCO}{(pCO + K_2 pCO_2)}$	$3.31 \cdot 10^4$	83.697	-	-	$1.68 \cdot 10^{-4}$	-60.403	0.830	61.91	0.00081	185
4 $r = \frac{k pH_2 pCO}{(pCO + K_2 pH_2O)}$	$5.31 \cdot 10^4$	87.588	-	-	$8.99 \cdot 10^{-2}$	-8.997	0.727	33.76	0.00103	186
5 $r = \frac{k pH_2^2 pCO}{(K_1 pCO pH_2 + pH_2O)}$	$1.00 \cdot 10^5$	52.340	$1.27 \cdot 10^0$	-37.474	-	-	0.723	33.10	0.00104	187
6 $r = \frac{k pH_2 pCO^{0.5}}{(1 + K_1 pCO)^2}$	$4.90 \cdot 10^5$	76.731	$2.23 \cdot 10^{-3}$	-16.694	-	-	0.858	76.92	0.00740	173
7 $r = \frac{k pH_2 pCO}{(1 + K_1 pCO)^2}$	$4.90 \cdot 10^3$	76.476	$2.24 \cdot 10^{-3}$	-16.694	-	-	0.832	62.91	0.00081	188
8 $r = \frac{k pH_2 pCO}{(1 + K_1 pCO + K_2 pH_2)^2}$	$5.12 \cdot 10^5$	81.342	$4.97 \cdot 10^0$	-35.554	$6.31 \cdot 10^2$	-11.222	0.870	48.33	0.00073	51
9 $r = \frac{k pH_2 pCO}{(1 + K_1 pCO + K_2 pCO_2 + K_3 pH_2O)}$	$3.01 \cdot 10^7$	70.192	$8.27 \cdot 10^0$	-34.318	$k_2: 6.31 \cdot 10^{-6}$ $k_3: 8.06 \cdot 10^{-36}$	$H_{ads(2)}: -128.048$ $H_{ads(3)}: -46.307$	0.910	47.15	0.00064	189
10 $r = \frac{k pH_2^{0.5} pCO}{(1 + K_1 pCO + K_2 pCO_2 + K_3 pH_2O)^2}$	$1.49 \cdot 10^3$	55.000	$2.34 \cdot 10^{-1}$	-5.789	$k_2: 5.86 \cdot 10^{-5}$ $k_3: 2.54 \cdot 10^{-9}$	$H_{ads(2)}: -61.399$ $H_{ads(3)}: -37.793$	0.670	9.86	0.00120	189

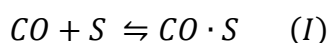
It is worth mentioning that the kinetic model fitting studies of Fe/zeolite catalyst for FTS in the literature are rare. Among the models listed in Table 9, most were developed/fitted for traditional Fe-based catalysts, except for model 8, that was studied over a Fe/zeolite catalyst. In general, the models presented a fit with correlation parameter R^2 ranging from 0.67 to 0.92 and all the parameters estimated were physically consistent.

Notably, the worst fits were observed in models accounting for water adsorption, specifically models 4, 5, and 10. Model 9, despite incorporating water adsorption, exhibited a reasonable fit; however, the pre-exponential adsorption constant obtained was on the order of 10^{-36} , which is practically zero. This suggests that water does not significantly affect the reaction rate for this catalyst, indicating that the formed water rapidly desorbs or is consumed on the catalyst surface.

There is not a consensus in the literature if water should be accounted in the inhibition term of the reaction rate of Fe-based catalysts. The first models developed considered water adsorption, such as model 4, which served as the basis of several FTS kinetic investigations over the years¹⁸⁷. However, kinetic studies of Sasol company pointed out that the apparent water inhibition depends strongly on the composition of the feed gas.¹⁹⁰

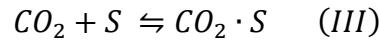
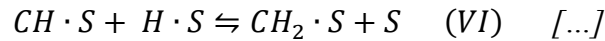
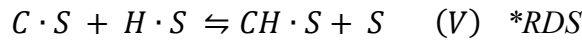
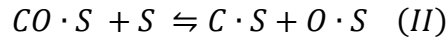
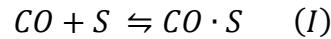
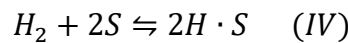
Ledakowicz et al. (1985)¹⁹¹ reported that the water produced could be shifted to form CO_2 over a catalyst with considerable WGS activity. Hence, the inhibition of the rate due to competitive chemisorption of water could be disregarded. Similar to this work findings, Nikbakth, Mirzaei and Atashi (2018)⁵¹ set that FTS reaction rate showed a better fit to kinetic data based on CO consumption without considering the effect of water. When studying a Fe-Co-Ce/Zeolite catalyst, the authors observed that carbon monoxide was adsorbed three times more than water on the catalyst surface.

Models 1, 2, and 3 exhibited a better fit compared to models 6, 7, and 9. The distinguishing factor between these groups is the consideration of CO_2 on the inhibition term of the reaction rate. This better fit observed for the first group suggests that CO_2 adsorbs onto the catalyst surface. This corroborates with the study of Ledakowicz et al. (1985)¹⁹¹, who proposed that carbon monoxide conversion was influenced by adsorption of CO_2 . According to the authors it is reasonable to assume that competitive chemisorption of both CO and CO_2 occurs on the active sites of the catalyst with considerable activity of WGS, as expressed by equations (I) and (III).



When compared to models 1 and 2, which considered dissociative adsorption of CO, model 3 presented a worse fit, by assuming associative adsorption of CO and a single site mechanism. Therefore, based on the statistical parameters presented in Table 8, Model 1, proposed by Van der Laan et al. (1999)⁵² showed the best fit in this study. This model considers a dissociative adsorption of both H₂ and CO, a double site mechanism and a competitive adsorption of CO₂ and CO on the catalyst sites.

The set of elementary reactions proposed for Model 1 considers the steps presented in equations I to VI:



The assumptions for the Model 1 includes: the formation of the monomer intermediate (-CH-) is irreversible and it is the rate determining step (RDS); all intermediates on the catalyst surface are on the steady state; the adsorption steps of H₂ and CO are in the quasi-equilibrium; Fe catalysts exhibit a stronger adsorption of CO compared to H₂, leading to a higher surface concentration of dissociated CO in relation to H₂; and the CO₂ formed in the parallel WGS reaction competes for site adsorption and may inhibit FT reaction rate.

In the following mathematical development, [S] stands for vacant sites concentrations, [x · S] represents the concentration of adsorbed x species (x = H, CO, C, CO₂), and k and K are the kinetic constant and equilibrium constant, respectively, of the adsorption/reaction step.

From reaction I, the net adsorption rate of H₂ is given by Eq. 22.

$$r_1 = k_1 p_{H_2} [S]^2 - k_{-1} [H \cdot S]^2 \quad (22)$$

Considering $K_1 = k_1/k_{-1}$ the adsorption equilibrium constant, Eq. 23 is obtained,

$$r_1 = k_1 \left(p_{H_2} [S]^2 - \frac{[H \cdot S]^2}{K_1} \right) \quad (23)$$

As $r_1/k_1 \sim 0$, the concentration of adsorbed hydrogen species can be expressed by Eq. 24.

$$[H \cdot S] = K_1' p_{H_2}^{0.5} [S] \quad (K_1' = K_1^{0.5}) \quad (24)$$

The same is observed for the first step of CO adsorption, from reaction II, and Eqs. 25 – 27 are obtained.

$$r_2 = k_2 p_{CO} [S] - k_{-2} [CO \cdot S] \quad (25)$$

$$r_2 = k_2 \left(p_{CO} [S] - \frac{[CO \cdot S]}{K_2} \right) \quad (26)$$

$$[CO \cdot S] = K_2 p_{CO} [S] \quad (27)$$

From reaction III, assuming an equal amount of adsorbed C·S and O·S species, [C·S] can be expressed by Eqs. 28 -30.

$$r_3 = k_3 [CO \cdot S] [S] - k_{-3} \overbrace{[C \cdot S][O \cdot S]}^{[C \cdot S]^2} \quad (28)$$

$$r_3 = k_3 \left([CO \cdot S] [S] - \frac{[C \cdot S]^2}{K_3} \right) \quad (29)$$

$$[C \cdot S] = K_3' [CO \cdot S]^{0.5} [S]^{0.5} \quad (K_3' = K_3^{0.5}) \quad (30)$$

Substituting [CO · S] from Eq. (27) in Eq. (30) gives Eq. 31.

$$[C \cdot S] = K_3' K_2' p_{CO}^{0.5} [S] \quad (K_2' = K_2^{0.5}) \quad (31)$$

Finally, for the rate determining step, the reaction rate, r_4 , can be expressed by Eq. 32.

$$r_4 = r_{CO} = k_4 [C \cdot S] [H \cdot S] - \overbrace{k_{-4} [CH \cdot S][S]}^{\sim 0} \quad (32)$$

Substituting [C · S] and [H · S] from Eqs. (31) and (24) gives Eq. 33.

$$r_{CO} = k_4 K_3' K_2' K_1' p_{H_2}^{0.5} p_{CO}^{0.5} [S]^2 \quad (33)$$

From assumptions, $[C \cdot S], [CO_2 \cdot S] \gg [H_2 \cdot S], [H_2O \cdot S]$. Thus, only surface carbon and CO₂ compete for sites to adsorb, and the site balance is expressed by Eq. 34.

$$[S_{tot}] = [S] + [C \cdot S] + [CO_2 \cdot S] \quad (34)$$

Substituting [C · S] from Eq. (30) and assuming CO₂ adsorption from WGS as [CO₂ · S] = $K_{CO_2} p_{CO_2} [S]$ give Eqs. 35 and 36.

$$[S_{tot}] = [S] + K_3' K_2' p_{CO}^{0.5} [S] + K_{CO_2} p_{CO_2} [S] \quad (35)$$

$$[S] = \frac{[S_{tot}]}{1 + \frac{K_3' K_2' p_{CO}^{0.5} + K_{CO_2} p_{CO_2}}{K_{CO}}} \quad (36)$$

Substituting Eq. (36) in Eq.(33), the reaction rate can be expressed by Eqs. 37 and 38.

$$r_{CO} = \frac{\frac{k'}{[S_{tot}]^2 k_4 K_3' K_2' K_1' p_{H_2}^{0.5} p_{CO}^{0.5}}}{(1 + K_{CO} p_{CO}^{0.5} + K_{CO_2} p_{CO_2})^2} \quad (37)$$

$$r_{CO} = \frac{k' p_{H_2}^{0.5} p_{CO}^{0.5}}{(1 + K_{CO} p_{CO}^{0.5} + K_{CO_2} p_{CO_2})^2} \quad (38)$$

Moreover, all kinetic constants depend on temperature and are supposed to follow Arrhenius law, as in Eqs. 39-4:

$$k = k_0 e^{\left(\frac{-E_a}{R.T}\right)} \quad (39)$$

$$K_{CO} = k_0 e^{\left(\frac{-H_{ads CO}}{R.T}\right)} \quad (40)$$

$$K_{CO_2} = k_{CO_2_0} e^{\left(\frac{-H_{ads CO_2}}{R.T}\right)} \quad (41)$$

In which, E_a is the reaction activation energy, $H_{ads CO}$, $H_{ads CO_2}$ are the adsorption enthalpies of the adsorbed molecules and k_0 , k_{CO_0} and $k_{CO_2_0}$ are the pre-exponential factors.

The parity plot encountered for Model 1 is shown in Figure 48 and the residuals distribution of the fit are show in Figure 49.

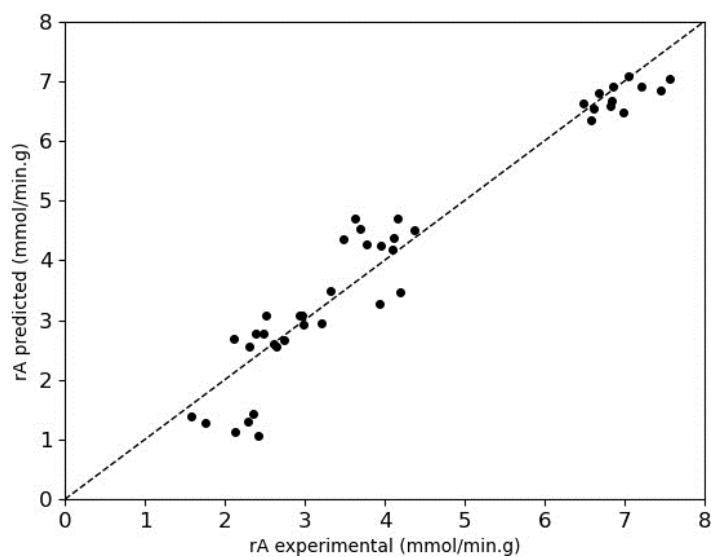


Figure 48 - Parity plot of predicted Model 1 and experimental CO consumption rate.

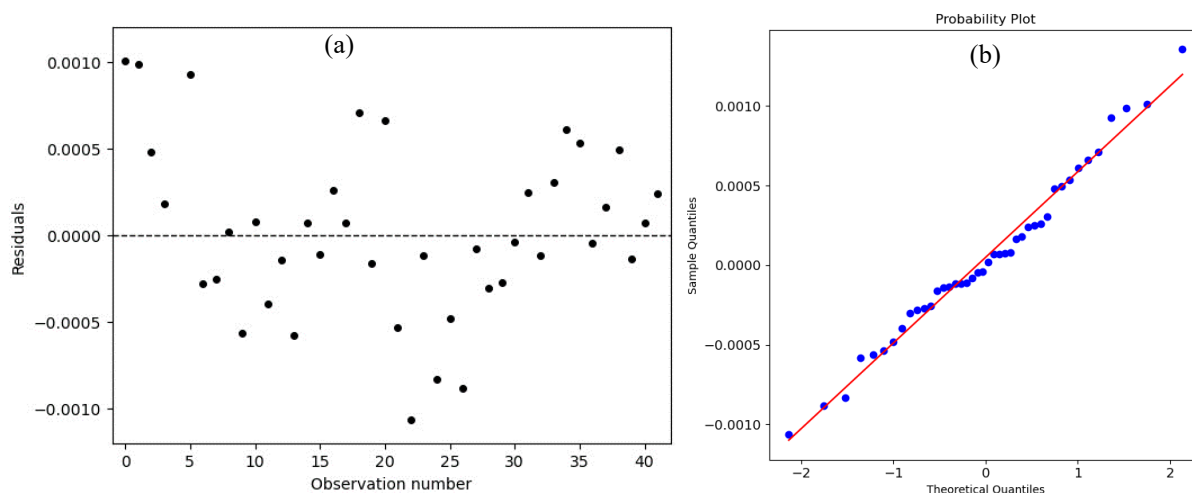


Figure 49 - Residuals distribution: a) dependent r_{co} variable b) normal probability plot.

Overall, from Figure 48, the adjusted data points exhibited narrow dispersion closely with the ideal fitting diagonal, indicating a good fit. Analysis of the residual plot in Figure 49a revealed no issues with the statistical homoscedasticity of the model, confirming consistent error variability across all considered observations. Furthermore, the residuals displayed a significant normal distribution, as depicted in Figure 49b.

The calculated activation energy of Model 1 was determined to be 78.85 kJ/mol, which is in good agreement with results reported in the literature. According to Eshraghi, Mirzaei and Atashi (2015)¹⁹² most of the fitted models for FTS presents values of activation ranging from 63 to 132.3 kJ/mol. The authors emphasized that the wide range observed can be attributed to varying mass transfer conditions across different studies. Moreover, the calculated enthalpy of

CO and CO₂ adsorption were found to be -17.78 kJ/mol and -98.81 kJ/mol, respectively, which indicates an exothermic adsorption process, as expected.¹⁸²

Figure 50 and Figure 51 present a surface response of Model 1 applied to the experimental data, and the model behavior under various H₂/CO feed ratios. The results showed the positive effect of increasing temperature on the reaction rate, as expected, since kinetic constants were assumed to follow Arrhenius's law. Figure 51 also shows that the model exhibited a good prediction for the reaction rate under the different H₂/CO feed conditions studied.

It should also be mentioned the lower reaction rate observed for H₂/CO feed ratio of 1. Experimental observations indicated that there was no significant CO conversion at a temperature of 533.15K for H₂/CO feed ratios of 1 and 1.5 in the kinetic regime. Consequently, data corresponding to these feed compositions were only included from a temperature of 543.15K onwards, as depicted in Table 9.

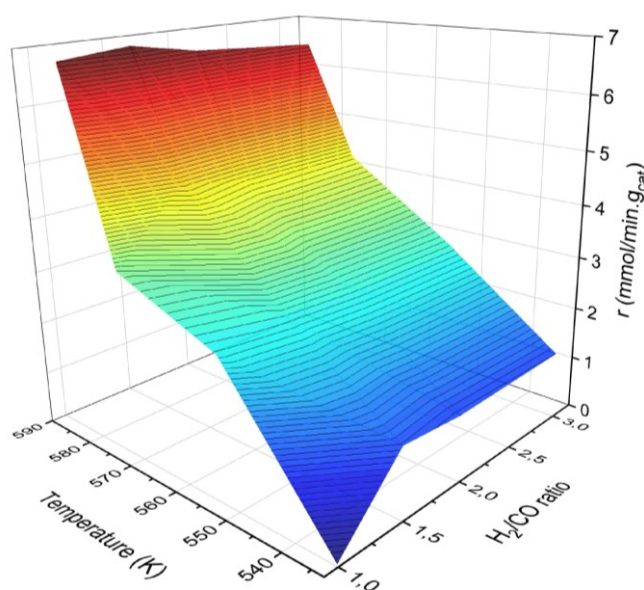


Figure 50 - Surface response of Model 1 evaluating temperature and H₂/CO ratio.

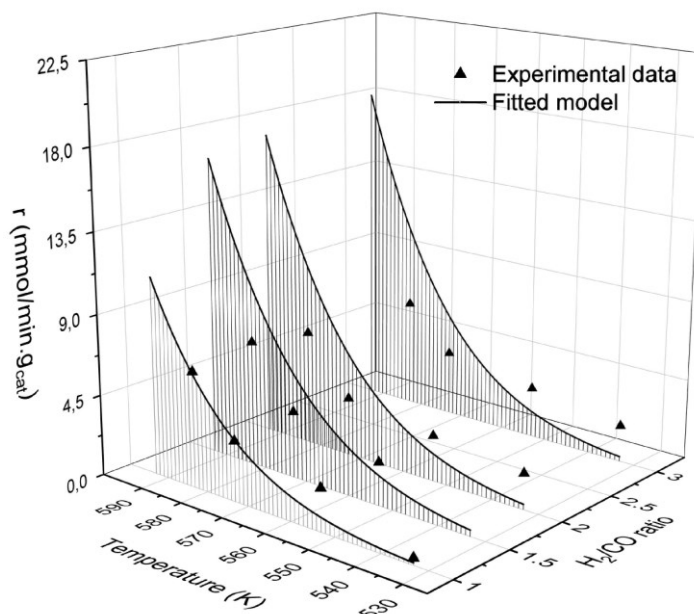


Figure 51 – Model 1 and experimental data curves.

Dry, Shingles and Boshoff (1972)¹⁹³ postulated that the reaction rate of FTS was influenced only by the p_{H_2} for CO conversions below 60%, as described by the power law expression: $-r_{CO} = k p_{H_2}^\alpha$. As shown in Table 8, an increase in the reaction rate is evident with a higher concentration of H_2 in the feed. However, the power law model was fitted to the collected data and did not present a good fit, with an R^2 value of 0.7 and an RMSE of 0.001. Consequently, LHHW models, incorporating the adsorption of different species on the catalyst surface, provided a superior fit to the experimental data.

5.4.3 Diffuse Reflectance Infrared Fourier Transform Spectroscopy (DRIFTS-*in situ*)

The Diffuse Reflectance Infrared Fourier Transform Spectroscopy (DRIFTS) technique is employed to assess catalyst surfaces under operational conditions, showing the molecules interactions with the catalyst surface. Therefore, DRIFTS-*in situ* was conducted on the Fe-Z91DI catalyst under FTS conditions to analyze the possible reaction intermediates on the catalyst surface. The obtained results are shown in Figure 52.

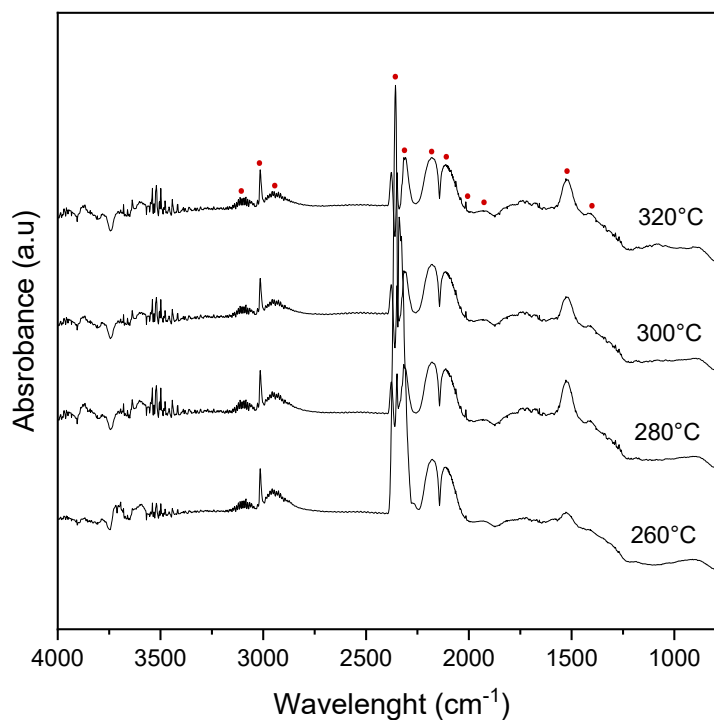


Figure 52 – DRIFTS-*in situ* H₂/CO analysis of Fe-Z91DI catalyst. P=8bar, H₂/CO=2, WHSV=4000 ml.g⁻¹.h⁻¹.

The spectra presented absorption in three characteristic regions. Absorption within the 1200-1700 cm⁻¹ range is attributed to bonding oxygenates species, such as acetates, formates, carbonates and carboxylates¹⁹⁴. Typically, the bands of CO₂ adsorbed species, including chelating or bridging bidentate carbonates, monodentate carbonates, or linearly coordinated CO₂ species, appear in the range of 1707 to 1366 cm⁻¹¹⁹⁵. Notably, bands were observed around 1524 cm⁻¹ and 1415 cm⁻¹, which can be assigned to bidentate and monodentate carbonate, respectively^{194,195}. Therefore, the observed bands in this region suggest the occurrence of CO₂ adsorption over the studied catalyst surface. Moreover, it was observed the increase in these bands between temperatures of 260°C and 280°C, as expected, since the catalyst presents higher CO₂ selectivity at higher temperatures.

The range from 1800-2100 cm⁻¹ is assigned to CO-adsorbed species. CO molecule can adsorb over distinct sites on the catalyst surface, exhibiting linear adsorption, or adsorbing over two adjacent sites, categorizing it as bridge adsorption¹⁸². The slight broad band observed between 1877-1965 cm⁻¹ is attributed to CO-bridged species, while the small distinct band at 2012 cm⁻¹ is related to the CO linearly adsorbed species^{182,196}. The bands at 2112 cm⁻¹ and 2180 cm⁻¹ are characteristic of gaseous CO molecules, and the bands within the 2312 cm⁻¹ and 2389 cm⁻¹ range are related to gaseous CO₂ molecules.^{182,196}

Finally, the range between 2700-3200 cm^{-1} is assigned to C-H bonding hydrocarbons region. The bands observed in the range 2848 3166 cm^{-1} are characteristic of gaseous CH_4 molecules, as reported.¹⁹⁷ A summary of the main species observed in Figure 52 is presented in Table 10.

Table 10 - Summary of observed bands from DRIFTS analysis.

Species	Structure	Absorption wavelength (cm^{-1})	Reference
Bidentate carbonate		1524	194,195
Monodentate carbonate		1415	194,195
Bridge adsorbed CO		1917	182,196
Linear adsorbed-CO		2015	182,196
Gaseous CO		2112 2180	182,196
Gaseous CO_2		2353	182,196
Gaseous CH_4		2944 3014 3099	197

Therefore, the bands observed in Figure 52 corroborates with the mechanism proposed in Model 1. The presence of carbonates and CO-adsorbed species signs to the adsorption of both CO and CO_2 . Moreover, the presence of CO-bridged species suggests the dissociative adsorption path of CO, which aligns with Model 1.

6

CONCLUSIONS

This work focused on studying Fe/HZSM-5 catalysts for Fischer-Tropsch synthesis on performing the synthesis, catalyst characterization, catalytic evaluation, and kinetic assessment. The catalysts proposed were successfully synthesized using physical mixing or dry impregnation methods, incorporating iron oxide on the HZSM-5 support at various Si/Al ratios.

The IR and RAMAN spectroscopies showed the characteristic bands of the zeolite and iron oxide structures, respectively. XRD analysis demonstrated good crystallinity of the catalysts, exhibiting characteristic phases of Fe₂O₃ and H-ZSM5. The textural characterization indicated a high surface area, with presence of mesopores. The reduction study showed the multiple reduction stages of iron oxides particles, consistent with literature findings. TEM analysis showed nanoparticles ranging from 23-30 nm, with impregnation resulting in smaller crystallite sizes compared to the physical mixture. Chemisorption studies demonstrated that iron impregnation altered the moderate acidity of the studied zeolites.

The catalysts were active for the Fischer-Tropsch synthesis, showing CO conversion greater than 50% at 300 °C, and C₅-C₈ selectivity up to 37% at low space velocity. The catalyst with smaller Fe crystallite size (Fe-Z91DI) demonstrated the best FTS activity. In general, the catalysts exhibited greater formation of light chain hydrocarbons (C₂-C₄), followed by liquid hydrocarbons in the gasoline range (C₅-C₈). Temperature positively influenced CO conversion but also increased CO₂ selectivity, and a loss of activity was observed after temperature variation. Pressure, support SiO₂/Al₂O₃ ratio, and H₂/CO feed ratio affected CO conversion and CO₂ selectivity, but not the product selectivity. Moreover, the catalyst remained stable over 72 hours of FTS conditions without structural changes or coke deposition.

The proposed kinetic LHHW model for the Fe-Z91DI catalyst followed the carbide mechanism, with kinetic parameters consistent with similar literature works. The best fitted model considers dissociative adsorption of CO and H₂, reacting in a double site mechanism to form the monomer (-CH_x-), which is the rate-determining step (RDS). Additionally, CO and CO₂ compete for site adsorption, and the rate of CO consumption is proportional to the partial pressure of H₂. *In situ* DRIFTS analysis confirmed certain intermediates in the proposed mechanism.

In summary, this research contributed to a better understanding of the relationship between physical-chemical properties of Fe/HZSM-5 catalysts and their catalytic performance in the Fischer-Tropsch synthesis. The study of reaction parameters proved to be crucial in comprehending how different variables affect FTS results with Fe/HZSM-5 catalysts. Furthermore, the kinetic assessment gave a contribution for understanding CO activation mechanism for catalyst type, which is essential for catalyst optimization with similar compositions in future studies.

6.1 SUGGESTIONS FOR FUTURE WORKS

The perspectives for the study of Fe/H-ZSM5 catalysts for FTS include studying other synthesis methods for this catalyst, in order to precisely evaluate the influence of particle size and allocation on the zeolite framework on the catalytic performance. A study on the zeolite porosity is an alternative to modify catalyst properties for ensuring a superior selectivity for liquid hydrocarbons. Additionally, optimizing catalyst composition by incorporating alkaline and oxide promoters shows promise for enhancing catalyst results.

REFERENCES

1. Rozzi, E., Minuto, F. D., Lanzini, A. & Leone, P. Green Synthetic Fuels: Renewable Routes for the Conversion of Non-Fossil Feedstocks into Gaseous Fuels and Their End Uses. *Energies (Basel)* **13**, 420 (2020).
2. bp. bp Statistical Review of World Energy. <https://www.bp.com/en/global/corporate/energy-economics/statistical-review-of-world-energy.html> (2022).
3. The International Energy Agency. Transport Improving the sustainability of passenger and freight transport. <https://www.iea.org/topics/transport> (2022).
4. Roy, P., Mohanty, A. K. & Misra, M. Prospects of carbon capture, utilization and storage for mitigating climate change. *Environmental Science: Advances* (2023) doi:10.1039/D2VA00236A.
5. Chen, W. *et al.* Recent advances in the investigation of nanoeffects of Fischer-Tropsch catalysts. *Catal Today* **311**, 8–22 (2018).
6. Do, T. N., You, C., Chung, H. & Kim, J. Superstructure optimization model for design and analysis of CO₂-to-fuels strategies. *Comput Chem Eng* **170**, 108136 (2023).
7. Jin, K. *et al.* Conversion of CO₂ to gasoline over tandem Fe/C and HZSM-5 catalysts. *Sustain Energy Fuels* (2023) doi:10.1039/D2SE01567F.
8. Scopus database. Search from Scopus database. Fischer-Tropsch synthesis 1939-2022. https://www.scopus.com/results/results.uri?src=s&sort=plf-f&st1=Fischer-Tropsch+Synthesis&sid=c1a435f15185ee8d28dfc6c3c3112fb2&sot=b&sdt=cl&sl=40&s=TITLE-ABS-KEY%28fischer-tropsch+AND+synthesis%29&cl=t&ss=plf-f&ws=r-f&ps=plf-f&cs=r-f&origin=resultlist&zone=queryBar&featureToggles=FEATURE_DOCUMENT_RESULT_MICRO_UI%3A1&sessionSearchId=c1a435f15185ee8d28dfc6c3c3112fb2&limit=10&yearFrom=1939&yearTo=2022 (2023).
9. 4AirCRAFT. 4AirCRAFT Air Carbon Recycling for Aviation Fuel Technology. <https://4aircraft-project.eu/> (2021).

¹The Nature citation style was used for references.

10. Wang, X. & Economides, M. Gas-To-Liquids (GTL). in *Advanced Natural Gas Engineering* 243–287 (Elsevier, 2009). doi:10.1016/B978-1-933762-38-8.50014-9.
11. Gabriel, K. J. *et al.* Gas-to-liquid (GTL) technology: Targets for process design and water-energy nexus. *Curr Opin Chem Eng* **5**, 49–54 (2014).
12. Wood, D. A., Nwaoha, C. & Towler, B. F. Gas-to-liquids (GTL): A review of an industry offering several routes for monetizing natural gas. *J Nat Gas Sci Eng* **9**, 196–208 (2012).
13. Selvatico, D., Lanzini, A. & Santarelli, M. Low Temperature Fischer-Tropsch fuels from syngas: Kinetic modeling and process simulation of different plant configurations. *Fuel* **186**, 544–560 (2016).
14. Akbarzadeh, O. *et al.* Effect of Pressure, H₂/CO Ratio and Reduction Conditions on Co–Mn/CNT Bimetallic Catalyst Performance in Fischer–Tropsch Reaction. *Symmetry (Basel)* **12**, 698 (2020).
15. Yakovenko, R. E. *et al.* Bifunctional Cobalt Catalyst for the Synthesis of Waxy Diesel Fuel by the Fischer–Tropsch Method: From Development to Commercialization. Part 1: Selection of the Industrial Sample of the Zeolite Component HZSM-5. *Catal Ind* **13**, 230–238 (2021).
16. Graciano, J. E. A., Chachuat, B. & Alves, R. M. B. Conversion of CO₂-Rich Natural Gas to Liquid Transportation Fuels via Trireforming and Fischer–Tropsch Synthesis: Model-Based Assessment. *Ind Eng Chem Res* **57**, 9964–9976 (2018).
17. Panahi, M., Yasari, E. & Rafiee, A. Multi-objective optimization of a gas-to-liquids (GTL) process with staged Fischer-Tropsch reactor. *Energy Convers Manag* **163**, 239–249 (2018).
18. Sousa-Aguiar, E. F., Noronha, F. B. & Faro, Jr., A. The main catalytic challenges in GTL (gas-to-liquids) processes. *Catal Sci Technol* **1**, 698 (2011).
19. Summa, P., Samojeden, B. & Motak, M. Dry and steam reforming of methane. Comparison and analysis of recently investigated catalytic materials. A short review. *Polish Journal of Chemical Technology* **21**, 31–37 (2019).

¹The Nature citation style was used for references.

20. Batiot-Dupeyrat, C. Dry Reforming of Methane. in *Perovskites and Related Mixed Oxides* 501–516 (Wiley-VCH Verlag GmbH & Co. KGaA, 2015). doi:10.1002/9783527686605.ch22.
21. Osman, A. I. Catalytic Hydrogen Production from Methane Partial Oxidation: Mechanism and Kinetic Study. *Chem Eng Technol* **43**, 641–648 (2020).
22. Ciambelli, P., Palma, V., Palo, E. & Iaquaniello, G. Natural Gas Autothermal Reforming: an Effective Option for a Sustainable Distributed Production of Hydrogen. in *Catalysis for Sustainable Energy Production* 287–319 (Wiley-VCH Verlag GmbH & Co. KGaA, 2009). doi:10.1002/9783527625413.ch9.
23. Mohanty, U. S. *et al.* Current advances in syngas (CO + H₂) production through bi-reforming of methane using various catalysts: A review. *Int J Hydrogen Energy* **46**, 32809–32845 (2021).
24. Martinelli, M., Gnanamani, M. K., LeViness, S., Jacobs, G. & Shafer, W. D. An overview of Fischer-Tropsch Synthesis: XtL processes, catalysts and reactors. *Appl Catal A Gen* **608**, 117740 (2020).
25. Botes, F. G. *et al.* Middle distillate fuel production from synthesis gas via the Fischer–Tropsch process. in *Advances in Clean Hydrocarbon Fuel Processing* 329–362 (Elsevier, 2011). doi:10.1533/9780857093783.4.329.
26. Stranges, A. N. *A history of the fischer-tropsch synthesis in Germany 1926-45. Studies in Surface Science and Catalysis* vol. 163 (Elsevier B.V., 2007).
27. Seemann, M. & Thunman, H. Methane synthesis. in *Substitute Natural Gas from Waste* 221–243 (Elsevier, 2019). doi:10.1016/B978-0-12-815554-7.00009-X.
28. Stranges, A. N. Friedrich Bergius and the Rise of the German Synthetic Fuel Industry. *Isis* **75**, 643–667 (1984).
29. Fischer, F. & Tropsch, H. Process for the production of paraffin-hydrocarbons with more than one carbon atom. (1927).
30. Fischer, F. & Tropsch, H. Verfahren zur Gewinnung mehrgliedriger Paraffinkohlenwasserstoffe aus Kohlenoxyden und Wasserstoff auf katalytischem Wege. (1929).

¹The Nature citation style was used for references.

31. Mahmoudi, H. *et al.* A review of Fischer Tropsch synthesis process, mechanism, surface chemistry and catalyst formulation. *Biofuels Engineering* **2**, 11–31 (2017).
32. van de Loosdrecht, J. *et al.* Fischer–Tropsch Synthesis: Catalysts and Chemistry. in *Comprehensive Inorganic Chemistry II* vol. 7 525–557 (Elsevier, 2013).
33. Gupta, P. K., Kumar, V. & Maity, S. Renewable fuels from different carbonaceous feedstocks: a sustainable route through Fischer–Tropsch synthesis. *Journal of Chemical Technology & Biotechnology* **96**, 853–868 (2021).
34. Guettel, R., Kunz, U. & Turek, T. Reactors for Fischer-Tropsch Synthesis. *Chem Eng Technol* **31**, 746–754 (2008).
35. Teimouri, Z., Abatzoglou, N. & Dalai, A. K. Kinetics and Selectivity Study of Fischer–Tropsch Synthesis to C5+ Hydrocarbons: A Review. *Catalysts* **11**, 330 (2021).
36. Dry, M. E. Practical and theoretical aspects of the catalytic Fischer-Tropsch process. *Appl Catal A Gen* **138**, 319–344 (1996).
37. Dry, M. E. Chemical concepts used for engineering purposes. in *Studies in Surface Science and Catalysis* vol. 152 196–257 (Elsevier B.V., 2004).
38. Cheng, Y., Qiao, M. & Zong, B. Fischer–Tropsch Synthesis. in *Encyclopedia of Sustainable Technologies* vol. 3 403–410 (Elsevier, 2017).
39. Bukur, D. B., Todic, B. & Elbashir, N. Role of water-gas-shift reaction in Fischer–Tropsch synthesis on iron catalysts: A review. *Catal Today* **275**, 66–75 (2016).
40. van Santen, R. A., Ciobîcă, I. M., van Steen, E. & Ghouri, M. M. Mechanistic Issues in Fischer–Tropsch Catalysis. in 127–187 (2011). doi:10.1016/B978-0-12-387772-7.00003-4.
41. Shafer, W. *et al.* Fischer–Tropsch: Product Selectivity–The Fingerprint of Synthetic Fuels. *Catalysts* **9**, 259 (2019).
42. Davis, B. H. Fischer–Tropsch synthesis: current mechanism and futuristic needs. *Fuel Processing Technology* **71**, 157–166 (2001).

¹The Nature citation style was used for references.

43. Brady, R. C. & Pettit, R. Reactions of diazomethane on transition-metal surfaces and their relationship to the mechanism of the Fischer-Tropsch reaction. *J Am Chem Soc* **102**, 6181–6182 (1980).
44. Maitlis, P. M. Fischer–Tropsch, organometallics, and other friends. *J Organomet Chem* **689**, 4366–4374 (2004).
45. Ciobîcă, I. M., Kramer, G. J., Ge, Q., Neurock, M. & van Santen, R. A. Mechanisms for Chain Growth in Fischer–Tropsch Synthesis over Ru(0001). *J Catal* **212**, 136–144 (2002).
46. van Helden, P., van den Berg, J.-A. & Ciobîcă, I. M. Hydrogen-assisted CO dissociation on the Co(211) stepped surface. *Catal Sci Technol* **2**, 491 (2012).
47. Broos, R. J. P., Klumpers, B., Zijlstra, B., Filot, I. A. W. & Hensen, E. J. M. A quantum-chemical study of the CO dissociation mechanism on low-index Miller planes of Θ -Fe₃C. *Catal Today* **342**, 152–160 (2020).
48. Broos, R. J. P., Zijlstra, B., Filot, I. A. W. & Hensen, E. J. M. Quantum-Chemical DFT Study of Direct and H- and C-Assisted CO Dissociation on the χ -Fe₅C₂ Hägg Carbide. *The Journal of Physical Chemistry C* **122**, 9929–9938 (2018).
49. Davis, B. H. Fischer–Tropsch synthesis: current mechanism and futuristic needs. *Fuel Processing Technology* **71**, 157–166 (2001).
50. Okeson, T. J., Keyvanloo, K., Lawson, J. S., Argyle, M. D. & Hecker, W. C. On the kinetics and mechanism of Fischer–Tropsch synthesis on a highly active iron catalyst supported on silica-stabilized alumina. *Catal Today* **261**, 67–74 (2016).
51. Nikbakht, N., Mirzaei, A. A. & Atashi, H. Kinetic modeling of the Fischer-Tropsch reaction over a zeolite supported Fe-Co-Ce catalyst prepared using impregnation procedure. *Fuel* **229**, 209–216 (2018).
52. van der Laan, G. P. Kinetics, selectivity and scale up of the Fischer-Tropsch synthesis. (Rijksuniversiteit Groningen, 1999).
53. VANNICE, M. The catalytic synthesis of hydrocarbons from H₂/CO mixtures over the group VIII metals II. The kinetics of the methanation reaction over supported metals. *J Catal* **37**, 462–473 (1975).

¹The Nature citation style was used for references.

54. Puskas, I. & Hurlbut, R. S. Comments about the causes of deviations from the Anderson–Schulz–Flory distribution of the Fischer–Tropsch reaction products. *Catal Today* **84**, 99–109 (2003).
55. Zhou, W. *et al.* New horizon in C1 chemistry: breaking the selectivity limitation in transformation of syngas and hydrogenation of CO₂ into hydrocarbon chemicals and fuels. *Chem Soc Rev* **48**, 3193–3228 (2019).
56. Jong, K. P. De. Fischer–Tropsch Synthesis. in *Fischer-Tropsch Refining* 73–103 (Wiley, 2011). doi:10.1002/9783527635603.ch4.
57. Puskas, I. & Hurlbut, R. S. Comments about the causes of deviations from the Anderson–Schulz–Flory distribution of the Fischer–Tropsch reaction products. *Catal Today* **84**, 99–109 (2003).
58. Li, J. *et al.* Integrated tuneable synthesis of liquid fuels via Fischer–Tropsch technology. *Nat Catal* **1**, 787–793 (2018).
59. Todic, B., Nowicki, L., Nikacevic, N. & Bukur, D. B. Fischer–Tropsch synthesis product selectivity over an industrial iron-based catalyst: Effect of process conditions. *Catal Today* **261**, 28–39 (2016).
60. Klerk, A. De. Fischer–Tropsch fuels refinery design. *Energy Environ Sci* **4**, 1177 (2011).
61. de la Osa, A. R., De Lucas, A., Romero, A., Valverde, J. L. & Sánchez, P. Fischer–Tropsch diesel production over calcium-promoted Co/alumina catalyst: Effect of reaction conditions. *Fuel* **90**, 1935–1945 (2011).
62. Liu, Y. *et al.* Effect of reaction conditions on the catalytic performance of Fe-Mn catalyst for Fischer-Tropsch synthesis. *J Mol Catal A Chem* **272**, 182–190 (2007).
63. Akbarzadeh, O. *et al.* Effect of Temperature, Syngas Space Velocity and Catalyst Stability of Co-Mn/CNT Bimetallic Catalyst on Fischer Tropsch Synthesis Performance. *Catalysts* **11**, 846 (2021).
64. Li, H. *et al.* Effect of reaction temperature and H₂/CO ratio on deactivation behavior of precipitated iron Fischer-Tropsch synthesis catalyst. *Catal Today* (2022) doi:10.1016/j.cattod.2022.04.025.

¹The Nature citation style was used for references.

65. Dry, M. E. Fischer–Tropsch reactions and the environment. *Appl Catal A Gen* **189**, 185–190 (1999).
66. Lamprecht, D., Dancuart, L. P. & Harrilall, K. Performance Synergies between Low-Temperature and High-Temperature Fischer–Tropsch Diesel Blends. *Energy & Fuels* **21**, 2846–2852 (2007).
67. Mao, W. Y. *et al.* Links between Reaction Intermediates, Reactivity, and Reaction Conditions in Oxygenates Formation during Fischer-Tropsch Synthesis. *Energy Sources, Part A: Recovery, Utilization, and Environmental Effects* **36**, 2175–2182 (2014).
68. Niu, C. *et al.* Effect of process conditions on the product distribution of Fischer-Tropsch synthesis over an industrial cobalt-based catalyst using a fixed-bed reactor. *Appl Catal A Gen* **601**, 117630 (2020).
69. Dinse, A., Aigner, M., Ulbrich, M., Johnson, G. R. & Bell, A. T. Effects of Mn promotion on the activity and selectivity of Co/SiO₂ for Fischer–Tropsch Synthesis. *J Catal* **288**, 104–114 (2012).
70. Steynberg, A. P., Dry, M. E., Davis, B. H. & Breman, B. B. Fischer-Tropsch Reactors. in 64–195 (2004). doi:10.1016/S0167-2991(04)80459-2.
71. Gnanamani, M. K. *et al.* Fischer-Tropsch Synthesis: Activity and Selectivity of χ -Fe₅C₂ and θ -Fe₃C Carbides. in *Fischer-Tropsch Synthesis, Catalysts, and Catalysis* 16 (CRC Press, 2016).
72. Shen, J. *et al.* Design of a Fischer-Tropsch multi-tube reactor fitted in a container: A novel design approach for small scale applications. *J Clean Prod* **362**, 132477 (2022).
73. Pfeifer, P. *et al.* Scale-up of microstructured Fischer–Tropsch reactors – status and perspectives. *Curr Opin Chem Eng* **36**, 100776 (2022).
74. Liuzzi, D. *et al.* Advances in membranes and membrane reactors for the Fischer-Tropsch synthesis process for biofuel production. *Reviews in Chemical Engineering* **38**, 55–76 (2022).
75. Cheng, K. *et al.* Advances in Catalysis for Syngas Conversion to Hydrocarbons. in 125–208 (2017). doi:10.1016/bs.acat.2017.09.003.

¹The Nature citation style was used for references.

76. Perego, C., Bortolo, R. & Zennaro, R. Gas to liquids technologies for natural gas reserves valorization: The Eni experience. *Catal Today* **142**, 9–16 (2009).
77. Alsudani, F. T. *et al.* Fisher–Tropsch Synthesis for Conversion of Methane into Liquid Hydrocarbons through Gas-to-Liquids (GTL) Process: A Review. *Methane* **2**, 24–43 (2023).
78. Ail, S. S. & Dasappa, S. Biomass to liquid transportation fuel via Fischer Tropsch synthesis – Technology review and current scenario. *Renewable and Sustainable Energy Reviews* **58**, 267–286 (2016).
79. Abelló, S. & Montané, D. Exploring Iron-based Multifunctional Catalysts for Fischer–Tropsch Synthesis: A Review. *ChemSusChem* **4**, 1538–1556 (2011).
80. Shroff, M. D. *et al.* Activation of Precipitated Iron Fischer-Tropsch Synthesis Catalysts. *J Catal* **156**, 185–207 (1995).
81. de Smit, E. *et al.* Stability and Reactivity of ϵ - χ - θ Iron Carbide Catalyst Phases in Fischer–Tropsch Synthesis: Controlling μ C. *J Am Chem Soc* **132**, 14928–14941 (2010).
82. Liu, J., Song, Y., Guo, X., Song, C. & Guo, X. Recent advances in application of iron-based catalysts for CO hydrogenation to value-added hydrocarbons. *Chinese Journal of Catalysis* **43**, 731–754 (2022).
83. Chun, D. H. *et al.* Brief Review of Precipitated Iron-Based Catalysts for Low-Temperature Fischer – Tropsch Synthesis. *Top Catal* **63**, 793–809 (2020).
84. Abelló, S. & Montané, D. Exploring Iron-based Multifunctional Catalysts for Fischer–Tropsch Synthesis: A Review. *ChemSusChem* **4**, 1538–1556 (2011).
85. Uykun Mangaloğlu, D., Baranak, M., Ataç, Ö. & Atakül, H. Effect of the promoter presence in catalysts on the compositions of Fischer–Tropsch synthesis products. *Journal of Industrial and Engineering Chemistry* **66**, 298–310 (2018).
86. YANG, Y., XIANG, H.-W., XU, Y.-Y., BAI, L. & LI, Y.-W. Effect of potassium promoter on precipitated iron-manganese catalyst for Fischer-Tropsch synthesis. *Appl Catal A Gen* **266**, 181–194 (2004).

¹The Nature citation style was used for references.

87. Niu, L. *et al.* Effect of potassium promoter on phase transformation during H₂ pretreatment of a Fe₂O₃ Fischer Tropsch synthesis catalyst precursor. *Catal Today* **343**, 101–111 (2020).
88. Yang, Y. *et al.* Effect of alkalis (Li, Na, and K) on precipitated iron-based catalysts for high-temperature Fischer-Tropsch synthesis. *Fuel* **326**, 125090 (2022).
89. Schmal, M. *Heterogeneous Catalysis and its Industrial Applications*. (Springer International Publishing, 2016). doi:10.1007/978-3-319-09250-8.
90. Zhang, Q., Cheng, K., Kang, J., Deng, W. & Wang, Y. Fischer-Tropsch Catalysts for the Production of Hydrocarbon Fuels with High Selectivity. *ChemSusChem* **7**, 1251–1264 (2014).
91. Jun, K.-W., Roh, H.-S., Kim, K.-S., Ryu, J.-S. & Lee, K.-W. Catalytic investigation for Fischer–Tropsch synthesis from bio-mass derived syngas. *Appl Catal A Gen* **259**, 221–226 (2004).
92. Kang, S.-H. *et al.* Correlation of the amount of carbonaceous species with catalytic performance on iron-based Fischer–Tropsch catalysts. *Fuel Processing Technology* **109**, 141–149 (2013).
93. Lu, F., Chen, X., Lei, Z., Wen, L. & Zhang, Y. Revealing the activity of different iron carbides for Fischer-Tropsch synthesis. *Appl Catal B* **281**, 119521 (2021).
94. Gholami, Z. *et al.* Production of Light Olefins via Fischer-Tropsch Process Using Iron-Based Catalysts: A Review. *Catalysts* **12**, 174 (2022).
95. Cheng, K. *et al.* Pore size effects in high-temperature Fischer–Tropsch synthesis over supported iron catalysts. *J Catal* **328**, 139–150 (2015).
96. Xiong, H., Zhang, Y., Liew, K. & Li, J. Fischer–Tropsch synthesis: The role of pore size for Co/SBA-15 catalysts. *J Mol Catal A Chem* **295**, 68–76 (2008).
97. Valero-Romero, M. J., Rodríguez-Cano, M. Á., Palomo, J., Rodríguez-Mirasol, J. & Cordero, T. Carbon-Based Materials as Catalyst Supports for Fischer–Tropsch Synthesis: A Review. *Front Mater* **7**, (2021).

¹The Nature citation style was used for references.

98. Chen, W., Fan, Z., Pan, X. & Bao, X. Effect of Confinement in Carbon Nanotubes on the Activity of Fischer–Tropsch Iron Catalyst. *J Am Chem Soc* **130**, 9414–9419 (2008).
99. Chen, W., Fan, Z., Pan, X. & Bao, X. Effect of Confinement in Carbon Nanotubes on the Activity of Fischer–Tropsch Iron Catalyst. *J Am Chem Soc* **130**, 9414–9419 (2008).
100. Yu, G. *et al.* Fe_xO_y@C Spheres as an Excellent Catalyst for Fischer–Tropsch Synthesis. *J Am Chem Soc* **132**, 935–937 (2010).
101. Yu, L., Li, W.-X., Pan, X. & Bao, X. In- and Out-Dependent Interactions of Iron with Carbon Nanotubes. *The Journal of Physical Chemistry C* **116**, 16461–16466 (2012).
102. Wang, Z., Yu, J. & Xu, R. Needs and trends in rational synthesis of zeolitic materials. *Chem. Soc. Rev.* **41**, 1729–1741 (2012).
103. Kulprathipanja, S. *Zeolites in Industrial Separation and Catalysis*. (Wiley, 2010). doi:10.1002/9783527629565.
104. Weitkamp, J. Zeolites and catalysis. *Solid State Ion* **131**, 175–188 (2000).
105. Yoneyama, Y., He, J., Morii, Y., Azuma, S. & Tsubaki, N. Direct synthesis of isoparaffin by modified Fischer–Tropsch synthesis using hybrid catalyst of iron catalyst and zeolite. *Catal Today* **104**, 37–40 (2005).
106. Martínez, A. & López, C. The influence of ZSM-5 zeolite composition and crystal size on the in situ conversion of Fischer–Tropsch products over hybrid catalysts. *Appl Catal A Gen* **294**, 251–259 (2005).
107. Zhou, W. *et al.* New horizon in C1 chemistry: breaking the selectivity limitation in transformation of syngas and hydrogenation of CO₂ into hydrocarbon chemicals and fuels. *Chem Soc Rev* **48**, 3193–3228 (2019).
108. Cheng, K. *et al.* Selective Transformation of Syngas into Gasoline-Range Hydrocarbons over Mesoporous H-ZSM-5-Supported Cobalt Nanoparticles. *Chemistry - A European Journal* **21**, 1928–1937 (2015).
109. Hammer, H., Joisten, M., Lungen, S. & Winkler, D. New zeolites in fischer-tropsch synthesis. *Int J Energy Res* **267**, 217–225 (2004).

¹The Nature citation style was used for references.

110. Bessell, S. Support effects in cobalt-based fischer-tropsch catalysis. *Appl Catal A Gen* **96**, 253–268 (1993).
111. BESSELL, S. Investigation of bifunctional zeolite supported cobalt Fischer-Tropsch catalysts. *Appl Catal A Gen* **126**, 235–244 (1995).
112. Botes, F. G. & Böhringer, W. The addition of HZSM-5 to the Fischer–Tropsch process for improved gasoline production. *Appl Catal A Gen* **267**, 217–225 (2004).
113. Plana-Pallejà, J., Abelló, S., Berruoco, C. & Montané, D. Effect of zeolite acidity and mesoporosity on the activity of Fischer–Tropsch Fe/ZSM-5 bifunctional catalysts. *Appl Catal A Gen* **515**, 126–135 (2016).
114. Peng, X. *et al.* Impact of Hydrogenolysis on the Selectivity of the Fischer-Tropsch Synthesis: Diesel Fuel Production over Mesoporous Zeolite-Y-Supported Cobalt Nanoparticles. *Angewandte Chemie International Edition* **54**, 4553–4556 (2015).
115. Wang, P., Kang, J., Zhang, Q. & Wang, Y. Lithium ion-exchanged zeolite faujasite as support of iron catalyst for Fischer-Tropsch synthesis. *Catal Letters* **114**, 178–184 (2007).
116. Baranak, M., Gürünlü, B., Sariođlan, A., Ataç, Ö. & Atakül, H. Low acidity ZSM-5 supported iron catalysts for Fischer–Tropsch synthesis. *Catal Today* **207**, 57–64 (2013).
117. Liu, H. *et al.* Activated carbon templated synthesis of hierarchical zeolite Y-encapsulated iron catalysts for enhanced gasoline selectivity in CO hydrogenation. *J Mater Chem A Mater* **9**, 8663–8673 (2021).
118. Amoo, C. C. *et al.* Fabricating Fe Nanoparticles Embedded in Zeolite Y Microcrystals as Active Catalysts for Fischer–Tropsch Synthesis. *ACS Appl Nano Mater* **3**, 8096–8103 (2020).
119. Kang, S.-H., Bae, J. W., Sai Prasad, P. S. & Jun, K.-W. Fischer–Tropsch Synthesis Using Zeolite-supported Iron Catalysts for the Production of Light Hydrocarbons. *Catal Letters* **125**, 264–270 (2008).
120. Liu, Y. *et al.* Preparation of low carbon olefins on a core–shell K–Fe₅C₂@ZSM-5 catalyst by Fischer–Tropsch synthesis. *RSC Adv* **10**, 26451–26459 (2020).

¹The Nature citation style was used for references.

121. Agwara, J. N., Bakas, N. J., Neidig, M. L. & Porosoff, M. D. Challenges and Opportunities of Fe-based Core-Shell Catalysts for Fischer-Tropsch Synthesis. *ChemCatChem* **14**, (2022).
122. Feyzi, M., Khodaei, M. M. & Shahmoradi, J. Preparation and characterization of promoted Fe–Mn/ZSM-5 nano catalysts for CO hydrogenation. *Int J Hydrogen Energy* **40**, 14816–14825 (2015).
123. Li, M. *et al.* Direct conversion of syngas to gasoline ranged olefins over Na impellent Fe@NaZSM-5 catalyst. *Fuel* **308**, 121938 (2022).
124. Amoo, C. C. *et al.* Fabricating Fe Nanoparticles Embedded in Zeolite Y Microcrystals as Active Catalysts for Fischer–Tropsch Synthesis. *ACS Appl Nano Mater* **3**, 8096–8103 (2020).
125. Xu, Y., Liu, D. & Liu, X. Conversion of syngas toward aromatics over hybrid Fe-based Fischer-Tropsch catalysts and HZSM-5 zeolites. *Appl Catal A Gen* **552**, 168–183 (2018).
126. Song, F. *et al.* FeMn@HZSM-5 capsule catalyst for light olefins direct synthesis via Fischer-Tropsch synthesis: Studies on depressing the CO₂ formation. *Appl Catal B* **300**, 120713 (2022).
127. Wei, J. *et al.* Directly converting CO₂ into a gasoline fuel. *Nat Commun* **8**, 15174 (2017).
128. Fogler, H. S. *Elements of Chemical Reaction Engineering*. (Pearson, 2020).
129. Liu, Y., Luo, Q., Lu, H. & Wang, Z. The influencing factors of hydrothermal synthesis of ZSM-5 zeolite and its adsorption of phenol, quinoline and indole. *Mater Res Express* **6**, 115540 (2019).
130. Sabarish, R. & Unnikrishnan, G. Synthesis, characterization and evaluations of micro/mesoporous ZSM-5 zeolite using starch as bio template. *SN Appl Sci* **1**, 989 (2019).
131. Shirazi, L., Jamshidi, E. & Ghasemi, M. R. The effect of Si/Al ratio of ZSM-5 zeolite on its morphology, acidity and crystal size. *Crystal Research and Technology* **43**, 1300–1306 (2008).

¹The Nature citation style was used for references.

132. Senamart, N. *et al.* Characterization and temperature evolution of iron-containing species in HZSM-5 zeolite prepared from different iron sources. *Journal of Porous Materials* **26**, 1227–1240 (2019).
133. Structure commission, I. Z. A. Database of Zeolite Structures. (2022).
134. Nabiyouni, G., Shabani, A., Karimzadeh, S., Ghasemi, J. & Ramazani, H. Synthesis, characterization and magnetic investigations of Fe₃O₄ nanoparticles and zeolite-Y nanocomposites prepared by precipitation method. *Journal of Materials Science: Materials in Electronics* **26**, 5677–5685 (2015).
135. Krisnandi, Y. K. *et al.* The new challenge of partial oxidation of methane over Fe₂O₃/NaY and Fe₃O₄/NaY heterogeneous catalysts. *Heliyon* **7**, e08305 (2021).
136. Chen, J., Feng, Z., Ying, P. & Li, C. ZnO Clusters Encapsulated inside Micropores of Zeolites Studied by UV Raman and Laser-Induced Luminescence Spectroscopies. *J Phys Chem B* **108**, 12669–12676 (2004).
137. Yu, Y., Xiong, G., Li, C. & Xiao, F.-S. Characterization of aluminosilicate zeolites by UV Raman spectroscopy. *Microporous and Mesoporous Materials* **46**, 23–34 (2001).
138. SUN, K. *et al.* Active sites in Fe/ZSM-5 for nitrous oxide decomposition and benzene hydroxylation with nitrous oxide. *J Catal* **254**, 383–396 (2008).
139. Nieuwoudt, M. K., Comins, J. D. & Cukrowski, I. The growth of the passive film on iron in 0.05 M NaOH studied *in situ* by Raman micro-spectroscopy and electrochemical polarisation. Part I: near-resonance enhancement of the Raman spectra of iron oxide and oxyhydroxide compounds. *Journal of Raman Spectroscopy* **42**, 1335–1339 (2011).
140. Sanson, A., Mathon, O. & Pascarelli, S. Local vibrational dynamics of hematite (α -Fe₂O₃) studied by extended x-ray absorption fine structure and molecular dynamics. *J Chem Phys* **140**, (2014).
141. Marshall, C. P., Dufresne, W. J. B. & Ruffledt, C. J. Polarized Raman spectra of hematite and assignment of external modes. *Journal of Raman Spectroscopy* **51**, 1522–1529 (2020).

¹The Nature citation style was used for references.

142. El Mendili, Y. *et al.* New evidences of in situ laser irradiation effects on γ -Fe₂O₃ nanoparticles: a Raman spectroscopic study. *Journal of Raman Spectroscopy* **42**, 239–242 (2011).
143. M.M.J. Treacy, J. B. H. *Collection of Simulated XRD Powder Patterns for Zeolites Fifth (5th) Revised Edition.* (Elsevier, 2007).
144. Bajec, D., Kostyniuk, A., Pohar, A. & Likozar, B. Nonoxidative methane activation, coupling, and conversion to ethane, ethylene, and hydrogen over Fe/HZSM-5, Mo/HZSM-5, and Fe–Mo/HZSM-5 catalysts in packed bed reactor. *Int J Energy Res* **er.4697** (2019) doi:10.1002/er.4697.
145. Tan, P. Active phase, catalytic activity, and induction period of Fe/zeolite material in nonoxidative aromatization of methane. *J Catal* **338**, 21–29 (2016).
146. Xu, Y. *et al.* Direct synthesis of aromatics from syngas over Mo-modified Fe/HZSM-5 bifunctional catalyst. *Appl Catal A Gen* **598**, 117589 (2020).
147. Liu, R. *et al.* Identifying correlations in Fischer-Tropsch synthesis and CO₂ hydrogenation over Fe-based ZSM-5 catalysts. *Journal of CO₂ Utilization* **41**, 101290 (2020).
148. Hu, R. *et al.* Nano-Hollow Zeolite-Encapsulated Highly Dispersed Ultra-Fine Fe Nanoparticles as Fischer–Tropsch Catalyst for Syngas-to-Olefins. *Catalysts* **13**, 948 (2023).
149. Tu, J. *et al.* Synthesis of Fe₃O₄-nanocatalysts with different morphologies and its promotion on shifting C₅+ hydrocarbons for Fischer–Tropsch synthesis. *Catal Commun* **59**, 211–215 (2015).
150. Chen, K., Fan, Y., Hu, Z. & Yan, Q. Study on the Reduction Behavior of Zirconia Supported Iron Oxide Catalysts by Temperature-Programmed Reduction Combined within Situ Mössbauer Spectroscopy. *J Solid State Chem* **121**, 240–246 (1996).
151. Mehrabadi, B. A. T., Eskandari, S., Khan, U., White, R. D. & Regalbuto, J. R. A Review of Preparation Methods for Supported Metal Catalysts. in 1–35 (2017). doi:10.1016/bs.acat.2017.10.001.

¹The Nature citation style was used for references.

152. Schmal, M., Scheunemann, R., Ribeiro, N. F. P., Bengoa, J. F. & Marchetti, S. G. Synthesis and characterization of Pt/Fe–Zr catalysts for the CO selective oxidation. *Appl Catal A Gen* **392**, 1–10 (2011).
153. Lin, H.-Y., Chen, Y.-W. & Li, C. The mechanism of reduction of iron oxide by hydrogen. *Thermochim Acta* **400**, 61–67 (2003).
154. Yiu, H. H. P. *et al.* Synthesis of novel magnetic iron metal–silica (Fe–SBA-15) and magnetite–silica (Fe₃O₄–SBA-15) nanocomposites with a high iron content using temperature-programed reduction. *Nanotechnology* **19**, 255606 (2008).
155. Stoicescu, C. S. *et al.* Temperature programmed reduction of a core-shell synthetic magnetite: Dependence on the heating rate of the reduction mechanism. *Thermochim Acta* **709**, 179146 (2022).
156. Jiang, W. *et al.* Preparation and properties of superparamagnetic nanoparticles with narrow size distribution and biocompatible. *J Magn Magn Mater* **283**, 210–214 (2004).
157. Munnik, P., de Jongh, P. E. & de Jong, K. P. Recent Developments in the Synthesis of Supported Catalysts. *Chem Rev* **115**, 6687–6718 (2015).
158. Liu, Q. *et al.* Preparation of ZSM-5 molecular sieve modified by kaolin and its CO₂ adsorption performance investigation. *Microporous and Mesoporous Materials* **360**, 112678 (2023).
159. Caldeira, V. P. S., Santos, A. G. D., Pergher, S. B. C., Costa, M. J. F. & Araujo, A. S. Use of a low-cost template-free ZSM-5 for atmospheric petroleum residue pyrolysis. *Quim Nova* (2016) doi:10.5935/0100-4042.20160019.
160. Xu, Y. *et al.* Effect of iron loading on acidity and performance of Fe/HZSM-5 catalyst for direct synthesis of aromatics from syngas. *Fuel* **228**, 1–9 (2018).
161. Yuan, E., Wu, G., Dai, W., Guan, N. & Li, L. One-pot construction of Fe/ZSM-5 zeolites for the selective catalytic reduction of nitrogen oxides by ammonia. *Catal Sci Technol* **7**, 3036–3044 (2017).
162. Mao, W. Y. *et al.* Links between Reaction Intermediates, Reactivity, and Reaction Conditions in Oxygenates Formation during Fischer-Tropsch Synthesis. *Energy Sources, Part A: Recovery, Utilization, and Environmental Effects* **36**, 2175–2182 (2014).

¹The Nature citation style was used for references.

163. Tian, L. *et al.* Effects of reaction conditions on iron-catalyzed Fischer–Tropsch synthesis: A kinetic Monte Carlo study. *Journal of Molecular Structure: THEOCHEM* **941**, 30–35 (2010).
164. Wang, P., Kang, J., Zhang, Q. & Wang, Y. Lithium ion-exchanged zeolite faujasite as support of iron catalyst for Fischer-Tropsch synthesis. *Catal Letters* **114**, 178–184 (2007).
165. Nakhaei Pour, A. & Housaindokht, M. R. Fischer-Tropsch synthesis on iron catalyst promoted with HZSM-5 zeolite: Regeneration studies of catalyst. *J Nat Gas Sci Eng* **14**, 49–54 (2013).
166. Eliason, S. A. & Bartholomew, C. H. Reaction and deactivation kinetics for Fischer–Tropsch synthesis on unpromoted and potassium-promoted iron catalysts. *Appl Catal A Gen* **186**, 229–243 (1999).
167. NING, W. *et al.* Phase transformation of unpromoted and promoted Fe catalysts and the formation of carbonaceous compounds during Fischer–Tropsch synthesis reaction. *Appl Catal A Gen* **312**, 35–44 (2006).
168. Botes, F. G. The effect of a higher operating temperature on the Fischer–Tropsch/HZSM-5 bifunctional process. *Appl Catal A Gen* **284**, 21–29 (2005).
169. Ji, Y.-Y. *et al.* Effect of reaction conditions on the product distribution during Fischer–Tropsch synthesis over an industrial Fe-Mn catalyst. *Appl Catal A Gen* **214**, 77–86 (2001).
170. Akbarzadeh, O. *et al.* Effect of Pressure, H₂/CO Ratio and Reduction Conditions on Co–Mn/CNT Bimetallic Catalyst Performance in Fischer–Tropsch Reaction. *Symmetry (Basel)* **12**, 698 (2020).
171. de la Peña O’Shea, V. A., Alvarez-Galvan, M. C., Campos-Martin, J. M. & Fierro, J. L. G. Strong dependence on pressure of the performance of a Co/SiO₂ catalyst in Fischer–Tropsch slurry reactor synthesis. *Catal Letters* **100**, 105–116 (2005).
172. Botes, F. G., Niemantsverdriet, J. W. & Van De Loosdrecht, J. A comparison of cobalt and iron based slurry phase Fischer-Tropsch synthesis. *Catal Today* **215**, 112–120 (2013).

¹The Nature citation style was used for references.

173. Botes, F. G. & Breman, B. B. Development and Testing of a New Macro Kinetic Expression for the Iron-Based Low-Temperature Fischer–Tropsch Reaction. *Ind Eng Chem Res* **45**, 7415–7426 (2006).
174. Burgun, U. *et al.* Effects of Rare Earth Metal Promotion over Zeolite-Supported Fe–Cu-Based Catalysts on the Light Olefin Production Performance in Fischer–Tropsch Synthesis. *ACS Omega* **8**, 648–662 (2023).
175. Peña, D. *et al.* The Effect of Copper Loading on Iron Carbide Formation and Surface Species in Iron-Based Fischer–Tropsch Synthesis Catalysts. *ChemCatChem* **10**, 1300–1312 (2018).
176. Yang *et al.* Preparation of Iron Carbides Formed by Iron Oxalate Carburization for Fischer–Tropsch Synthesis. *Catalysts* **9**, 347 (2019).
177. de Smit, E. & Weckhuysen, B. M. The renaissance of iron-based Fischer–Tropsch synthesis: on the multifaceted catalyst deactivation behaviour. *Chem Soc Rev* **37**, 2758 (2008).
178. Schmal, M. & Pinto, J. C. Heterogeneous reaction kinetics, . in *Chemical Reaction Engineering* 199–234 (CRC Press, 2021). doi:10.1201/9781003046608-10.
179. Ercan, C., Dautzenberg, F. M., Yeh, C. Y. & Barner, H. E. Mass-Transfer Effects in Liquid-Phase Alkylation of Benzene with Zeolite Catalysts. *Ind Eng Chem Res* **37**, 1724–1728 (1998).
180. Dixon, A. G. Correlations for wall and particle shape effects on fixed bed bulk voidage. *Can J Chem Eng* **66**, 705–708 (1988).
181. Thoenes, D. & Kramers, H. Mass transfer from spheres in various regular packings to a flowing fluid. *Chem Eng Sci* **8**, 271–283 (1958).
182. Schmal, M. *Catálise Heterogênea*. (Synergia Editora, 2012).
183. Fazlollahi, F. *et al.* Preparation of Fe-Mn/K/Al₂O₃ Fischer-Tropsch Catalyst and Its Catalytic Kinetics for the Hydrogenation of Carbon Monoxide. *Chin J Chem Eng* **21**, 507–519 (2013).

¹The Nature citation style was used for references.

184. van der Laan, G. P., Beenackers, A. A. C. M. & Krishna, R. Multicomponent reaction engineering model for Fe-catalyzed Fischer–Tropsch synthesis in commercial scale slurry bubble column reactors. *Chem Eng Sci* **54**, 5013–5019 (1999).
185. Ledakowicz, S., Nettelhoff, H., Kokuun, R. & Deckwer, W. D. Kinetics of the Fischer–Tropsch synthesis in the slurry phase on a potassium promoted iron catalyst. *Industrial & Engineering Chemistry Process Design and Development* **24**, 1043–1049 (1985).
186. Dry, M. E. Advances in Fischer–Tropsch Chemistry. *Product R&D* **15**, 282–286 (1976).
187. Huff, G. A. & Satterfield, C. N. Intrinsic kinetics of the Fischer–Tropsch synthesis on a reduced fused-magnetite catalyst. *Industrial & Engineering Chemistry Process Design and Development* **23**, 696–705 (1984).
188. Ojeda, M. *et al.* CO activation pathways and the mechanism of Fischer–Tropsch synthesis. *J Catal* **272**, 287–297 (2010).
189. Zhou, L.-P. *et al.* Studies and Discriminations of the Kinetic Models for the Iron-Based Fischer–Tropsch Catalytic Reaction in a Recycle Slurry Reactor. *Energy & Fuels* **25**, 52–59 (2011).
190. Botes, F. G. The Effects of Water and CO₂ on the Reaction Kinetics in the Iron-Based Low-Temperature Fischer–Tropsch Synthesis: A Literature Review. *Catalysis Reviews* **50**, 471–491 (2008).
191. Ledakowicz, S., Nettelhoff, H., Kokuun, R. & Deckwer, W. D. Kinetics of the Fischer–Tropsch synthesis in the slurry phase on a potassium promoted iron catalyst. *Industrial & Engineering Chemistry Process Design and Development* **24**, 1043–1049 (1985).
192. Eshraghi, A., Mirzaei, A. A. & Atashi, H. Kinetics of the Fischer–Tropsch reaction in fixed-bed reactor over a nano-structured Fe–Co–Ce catalyst supported with SiO₂. *J Nat Gas Sci Eng* **26**, 940–947 (2015).
193. DRY, M. Rate of the Fischer–Tropsch reaction over iron catalysts. *J Catal* **25**, 99–104 (1972).
194. Kollár, M. *et al.* The mechanism of the Fischer–Tropsch reaction over supported cobalt catalysts. *J Mol Catal A Chem* **333**, 37–45 (2010).

¹The Nature citation style was used for references.

195. Polisi, M. *et al.* CO₂ Adsorption/Desorption in FAU Zeolite Nanocrystals: In Situ Synchrotron X-ray Powder Diffraction and in Situ Fourier Transform Infrared Spectroscopic Study. *The Journal of Physical Chemistry C* **123**, 2361–2369 (2019).
196. Santos, J., Bobadilla, L., Centeno, M. & Odriozola, J. Operando DRIFTS-MS Study of WGS and rWGS Reaction on Biochar-Based Pt Catalysts: The Promotional Effect of Na. *C (Basel)* **4**, 47 (2018).
197. Weiß, J. *et al.* Operando DRIFT and In situ Raman Spectroscopic Studies on Aspects of CO₂ Fischer-Tropsch Synthesis Catalyzed by Bulk Iron Oxide-Based Catalysts. *ChemCatChem* **14**, (2022).

¹The Nature citation style was used for references.

APPENDIX A – CONVERSION AND SELECTIVITY CALCULATIONS

The wide range of products formed during FTS makes post-reaction calculations a challenging step. In the chromatographic analyses, two stationary phases coupled with TCD and FID detectors were used for quantifying the compounds. During the tests, a N₂ flow gas was mixed with the syngas (10% v/v) and used as an internal standard for calculations. The CO conversion, X_{CO} and CO₂ selectivity, S_{CO_2} , were calculated following the Eqs. A1 and A2.

$$X_{CO} = \frac{\frac{A_{CO}^{in}}{A_{N_2}^{in}} - \frac{A_{CO}^{out}}{A_{N_2}^{out}}}{\frac{A_{CO}^{in}}{A_{N_2}^{in}}} \quad A1$$

$$S_{CO_2} = \frac{c_{CO_2}^{out} Q_{tot}^{out} MM_{CO_2}}{c_{CO}^{in} Q_{tot}^{in} MM_{CO} X_{CO}} \quad A2$$

Where A^{in} and A^{out} stand for the chromatographic area of the compounds from the entrance and exit of the reactor, c is the molar concentration (mol/ml), Q_{tot} is the total flow of gases (mL/min), and MM is the molar mass of the compounds (g/mol). The selectivity of hydrocarbons was obtained using the weight percentage of the components. In the chromatograms, the peaks for different hydrocarbons are separated according to their carbon number in groups with their variations. The selectivity for each hydrocarbon group with a carbon number 'n' was obtained according to Eq. A3:

$$S_{C_nH_{2n+2}} = \frac{C_{C_nH_{2n+2}}}{\sum_{i=1}^m C_{C_nH_{2n+2}}} \quad A3$$

Where $C_{C_nH_{2n+2}}$ stands for the mass concentration of each hydrocarbon obtained from the chromatographic areas and 'm' is the highest number of carbon obtained in the chains during the test.

APPENDIX B – COMPLEMENTARY FTS TESTS FOR KINETIC MODELING

The complete results of kinetic data used for models' adjustment are presented in Table B1.

Table B1 – Kinetic data used for models adjustment.

T (K)	H ₂ /CO	X _{co} (%)	pH ₂ (bar)	pCO (bar)	pCO ₂ (bar)	pH ₂ O (bar)	r _{co} (mmol/min.g _{cat})
533	2	4.92	9.98	7.22	0.011	0.35	2.13
533	2	5.30	9.93	7.18	0.008	0.39	2.30
533	2	4.06	10.09	7.25	0.008	0.29	1.76
533	3	4.75	11.38	5.83	0.009	0.27	1.58
533	3	7.29	11.36	5.62	0.013	0.42	2.42
533	3	7.09	11.37	5.63	0.008	0.41	2.36
553	1	3.91	7.46	9.83	0.014	0.37	2.49
553	1	3.63	7.29	9.95	0.016	0.34	2.31
553	1	4.11	7.27	9.96	0.016	0.40	2.61
553	1.5	4.83	8.89	8.23	0.014	0.39	2.51
553	1.5	5.08	8.67	8.29	0.021	0.40	2.64
553	1.5	4.58	8.78	8.47	0.018	0.37	2.38
553	2	6.77	9.91	7.05	0.017	0.48	2.94
553	2	4.87	9.94	7.26	0.022	0.33	2.11
553	2	6.88	9.99	7.05	0.019	0.48	2.99
553	3	8.95	11.37	5.61	0.021	0.51	2.97
553	3	9.65	11.40	5.46	0.022	0.54	3.20
553	3	8.25	11.33	5.60	0.026	0.45	2.74
573	1	6.58	7.03	9.90	0.073	0.55	4.19
573	1	5.22	7.08	9.92	0.073	0.40	3.32
573	1	6.18	6.95	10.00	0.078	0.50	3.93
573	1.5	8.00	8.45	8.24	0.056	0.61	4.16
573	1.5	6.98	8.46	8.27	0.056	0.51	3.63
573	1.5	8.42	8.57	8.17	0.060	0.63	4.38
573	2	8.51	9.67	7.04	0.065	0.52	3.69
573	2	8.71	9.66	7.02	0.070	0.53	3.78

573	2	8.02	9.62	7.11	0.068	0.48	3.48
573	3	12.34	11.07	5.40	0.077	0.61	4.10
573	3	11.89	11.05	5.43	0.075	0.58	3.95
583	1	11.07	7.11	9.43	0.063	1.05	7.04
583	1	10.73	6.90	9.61	0.069	1.02	6.83
583	1	10.50	6.81	9.66	0.065	1.00	6.68
583	1.5	13.85	8.28	7.99	0.076	1.13	7.20
583	1.5	14.31	8.24	7.98	0.077	1.18	7.44
583	1.5	14.55	8.40	7.84	0.075	1.19	7.57
583	2	15.81	9.35	6.87	0.083	1.12	6.86
583	2	15.77	9.26	6.78	0.086	1.10	6.84
583	2	16.09	9.38	6.80	0.090	1.12	6.98
583	3	19.55	10.66	5.21	0.094	1.08	6.49
583	3	19.91	10.75	5.22	0.096	1.11	6.61
583	3	19.84	10.68	5.25	0.099	1.10	6.59

The partial pressure of each component was calculated with Dalton's law, Eq. B2:

$$p_i = y_i P_{tot} \text{ (B2)}$$

In which y_i is the molar fraction of the component i (CO, CO₂, H₂, H₂O or CH₄), and P_{tot} is the total pressure of the reactor. The molar fraction, y_i , of the component i was calculated according to Eq.B3:

$$y_i = \frac{F_i}{\sum_i^n F_i} \text{ (B3)}$$

In which, F_i is molar flow of the component i , and can be calculated from Eq.B4:

$$F_i = C_i^{out} Q_{tot}^{out} \text{ (B4)}$$

Where C_i^{out} is the concentration of the component i at the reactor outlet and Q_{tot}^{out} is the total volumetric flow rate at the reactor outlet.

APPENDIX C – COMPLEMENTARY CATALYST CHARACTERIZATION

This section presents complementary characterization of the catalysts.

Thermogravimetric curves

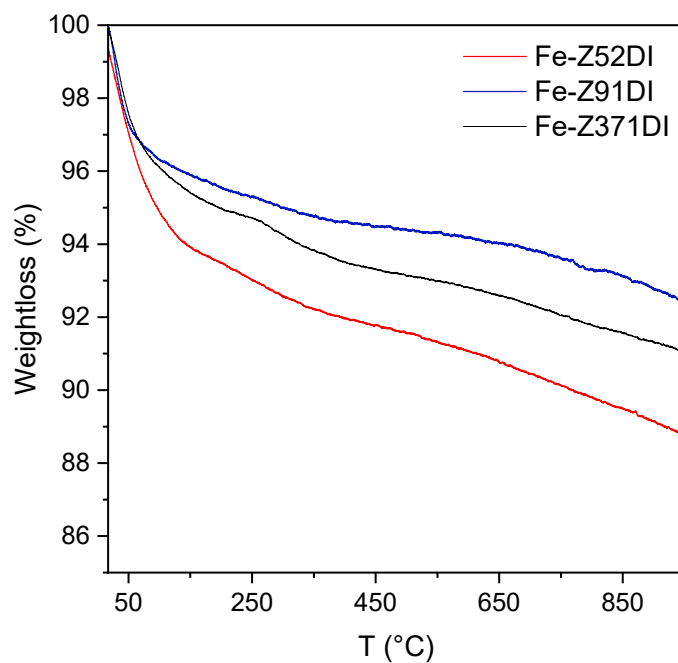


Figure C1 - TGA curves of the Fe-Z52DI, Fe-Z91DI and Fe-Z371DI catalysts after calcination.

CO₂ -TPD Curves

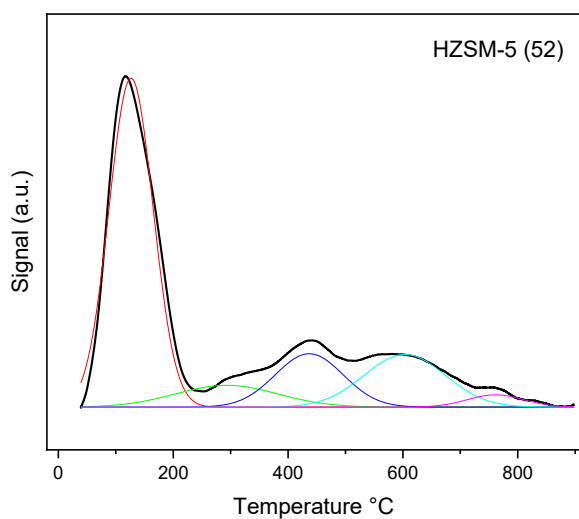


Figure C2 – Deconvolution curves of CO₂ TPD profile of HZSM-5 (52) zeolite.

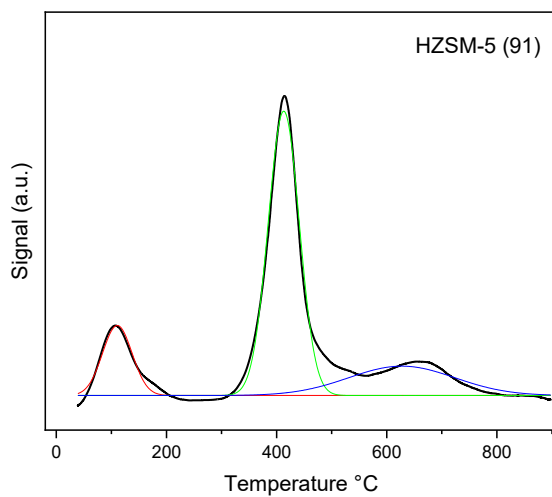


Figure C3 – Deconvolution curves of CO₂ TPD profile of HZSM-5 (91) zeolite.

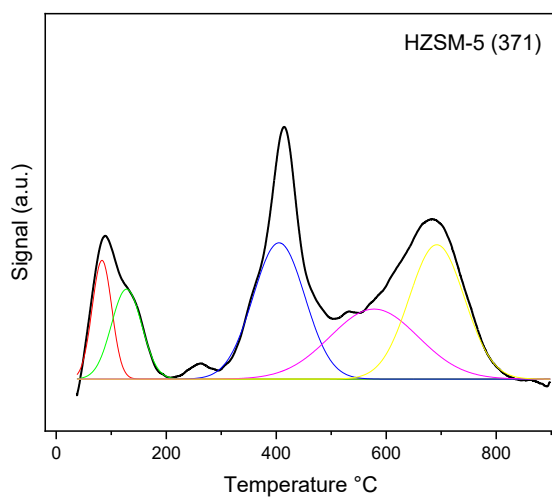


Figure C4 – Deconvolution curves of CO₂ TPD profile of HZSM-5 (371) zeolite.

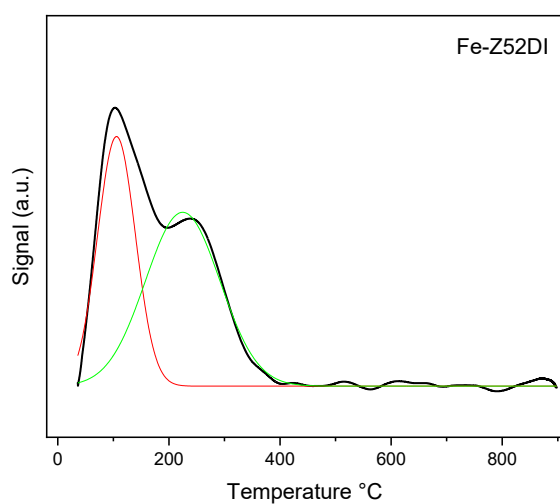


Figure C5 – Deconvolution curves of CO₂ TPD profile of FeZ52DI catalyst.

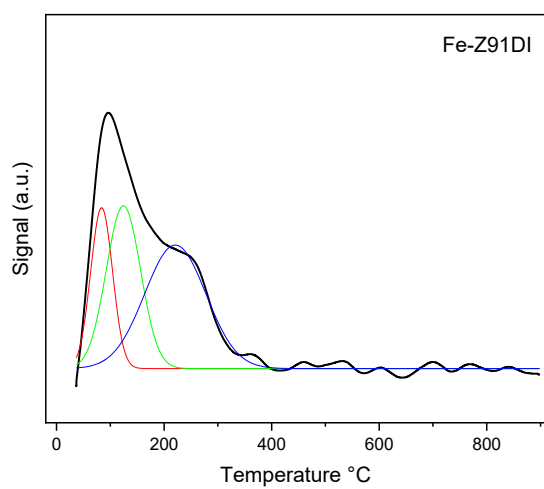


Figure C6 – Deconvolution curves of CO₂ TPD profile of FeZ91DI catalyst.

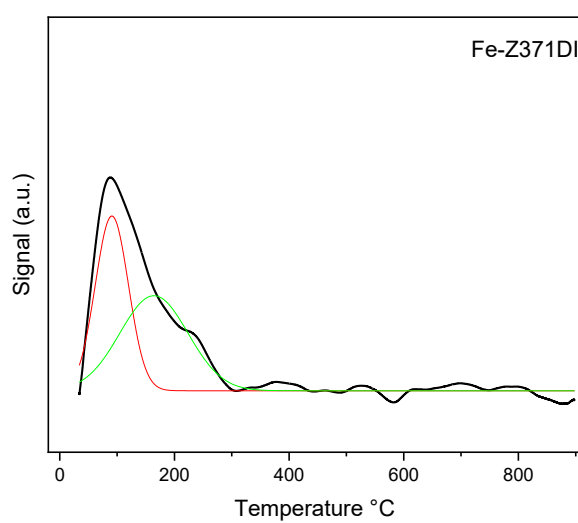
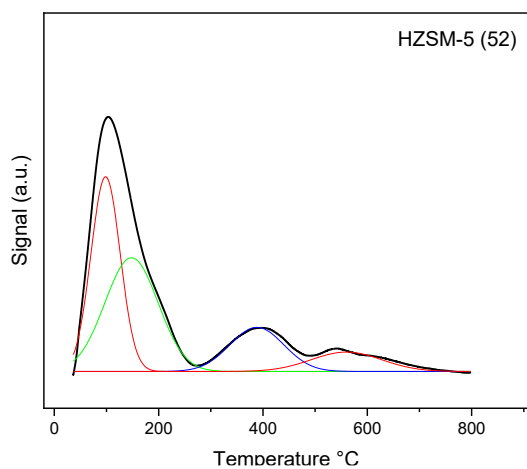
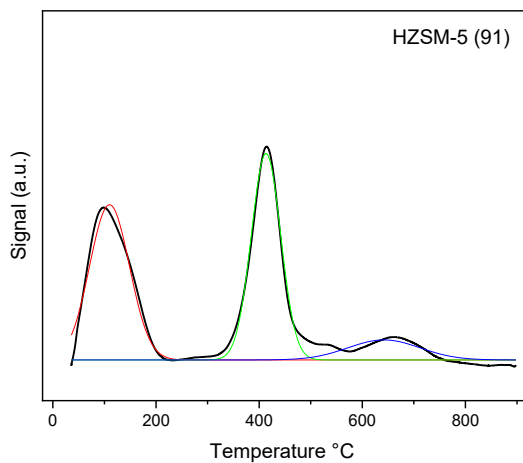
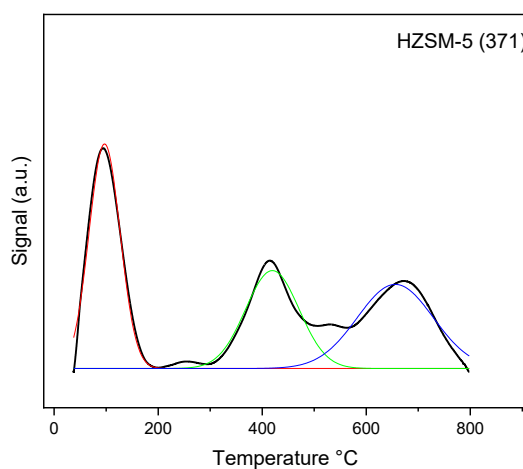


Figure C7 – Deconvolution curves of CO₂ TPD profile of FeZ371DI catalyst.

NH₃ – TPD CurvesFigure C8 – Deconvolution curves of NH₃ TPD profile of HZSM-5 (52) zeolite.Figure C9 – Deconvolution curves of NH₃ TPD profile of HZSM-5 (91) zeolite.Figure C10 – Deconvolution curves of NH₃ TPD profile of HZSM-5 (371) zeolite.

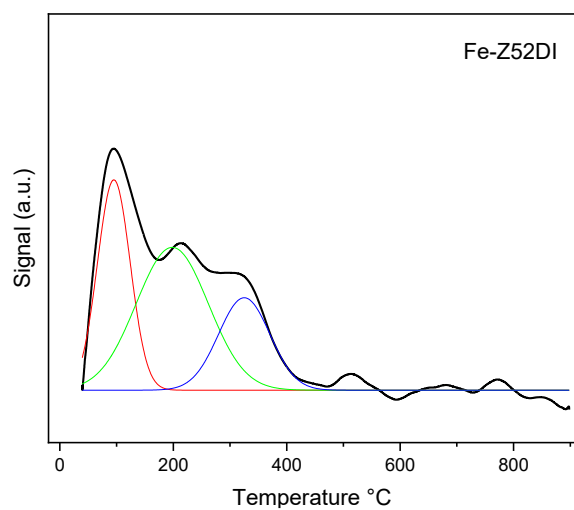


Figure C11 – Deconvolution curves of NH₃ TPD profile of FeZ52DI catalyst.

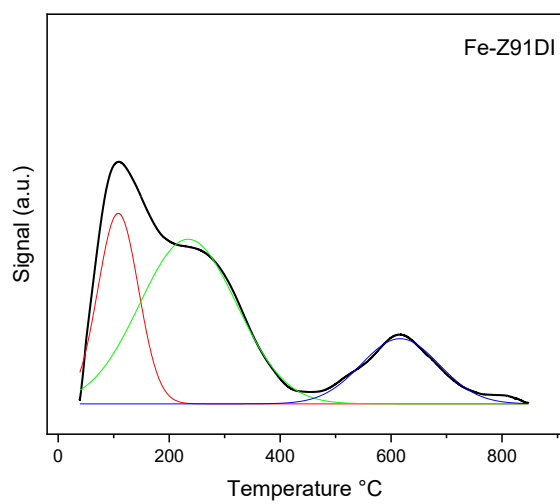


Figure C12 – Deconvolution curves of NH₃ TPD profile of FeZ91DI catalyst.

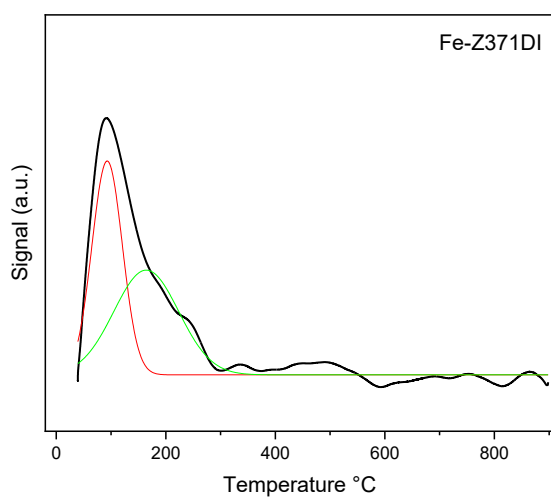


Figure C13 – Deconvolution curves of NH_3 TPD profile of FeZ371DI catalyst.

APPENDIX D – COMPLEMENTARY FTS TESTS

This section presents the complementary results from Fischer-Tropsch catalytic tests.

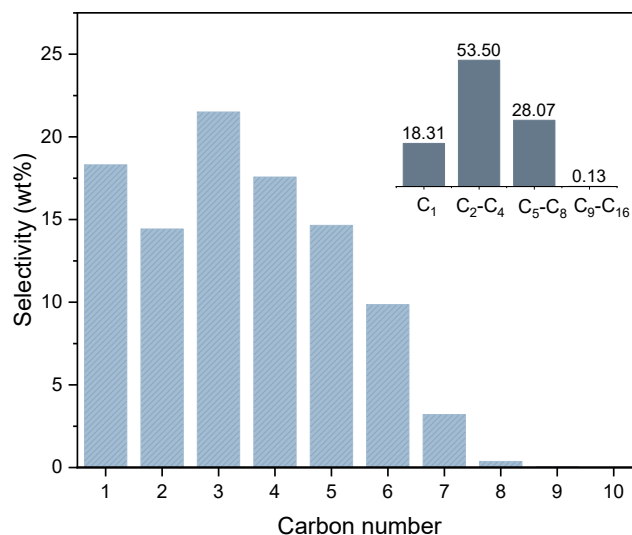


Figure D1 – Hydrocarbons distribution after temperature screening of Fe-Z91DI catalyst. T=300°C
P=20bar, H₂/CO=2, WHSV=6880 ml.g⁻¹.h⁻¹.

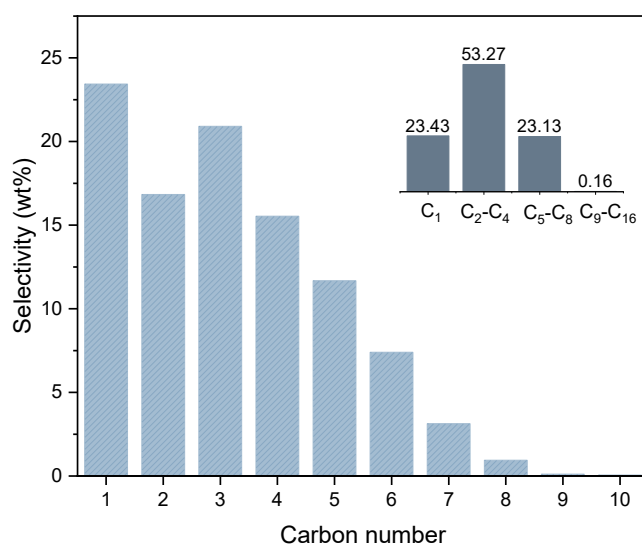


Figure D2 – Hydrocarbons distribution after temperature screening of Fe-Z91PM catalyst. T=300°C
P=20bar, H₂/CO=2, WHSV=6880 ml.g⁻¹.h⁻¹.